Microscopic Modelling of Collective Quadrupole Excitations of Nuclei

David Muir

PhD Thesis

University of York

Physics

November 2021

Abstract

We explore the Generalised Bohr Hamiltonian (GBH) approach in describing various nuclear observables - energy spectra and their associated $B\left(E2\right)$ electromagnetic transition rates - in even-even nuclei exhibiting quadrupole collective excitations. We carry out a systematic survey of the rare-earth region of the nuclear chart with the UNEDF0 functional in constrained Hartree-Fock-Bogoliubov calculations of mass parameters used in the GBH. In addition, we aim to address key questions with regards to the robustness of the Bohr Hamiltonian approach and specifically what key factors impact the nuclear observables calculated through this methodology. In particular, initial work is carried out on specific chains and a subgroup of nuclei, requested by various experimental physicists, with the UNEDF1 and UNEDF1$_{\mathrm{SO}}$ functionals.

Contents

1 Introduction and Aims **13**
1.1 The Research Project . . . 15
1.2 Thesis Structure . . . 17

2 Background Theory **18**
2.1 Quantum Many-Body Problem . . . 18
2.2 Many Particle Problem in Electronic Systems . . . 18
2.2.1 The Born-Oppenheimer Approximation . . . 19
2.2.2 Hartree-Fock Atomic Energy . . . 19
2.2.3 Hartree-Fock Operators . . . 20
2.2.4 Hartree-Fock Spin . . . 21
2.2.5 Hartree-Fock Roothaan Procedure/Equations . . . 22
2.2.6 Kohn-Sham Equations . . . 23
2.3 Hartree-Fock-Bogoliubov (HFB) Theory . . . 24
2.4 Nuclear Density Functional Theory (NDFT) . . . 25
2.4.1 The Skyrme Interaction . . . 26
2.4.2 The Gogny Interaction . . . 29
2.5 Nuclear Deformation . . . 29
2.6 ATDHFB Theory . . . 31
2.6.1 The ATDHFB Equation . . . 32
2.7 Mass Parameters . . . 33
2.7.1 HFB In a Different Notation . . . 33
2.7.2 Basics of Mass Parameters . . . 33
2.7.3 Cranking . . . 34
2.7.4 Relation between the Derivatives of R_0 and H_0 . . . 35
2.7.5 Constrained HFB . . . 36
2.7.6 Derivatives $\partial q_k/\partial \lambda_j$ . . . 36
2.7.7 Vibrational Mass Parameters . . . 38
2.7.8 Moments of Inertia . . . 38
2.8 Derivation of the Collective Model . . . 40
2.8.1 Collective Coordinates . . . 40
2.8.2 The Generalised Bohr Hamiltonian . . . 43
2.8.3 Limitations of the Bohr Hamiltonian . . . 43
2.8.4 Advantages of the Bohr Hamiltonian . . . 44

3 Computational Implementation **45**
3.1 Global Computational Procedure . . . 45
3.2 Experimental Data . . . 48
3.2.1 Experimental β_2 Deformation Parameter . . . 50
3.2.2 First excited $E_{2_1^+}$ state . . . 51
3.2.3 First excited $E_{4_1^+}$ state . . . 52

3.3 Computational Benchmark Tests and Convergence . . . 53
3.3.1 The Xenon isotopic Chain . . . 53
3.3.2 Computational Runtime and Convergence . . . 54
3.3.3 Numerical Stability of Convergence . . . 56
3.3.4 Nuclei near the Proton Dripline . . . 57
3.3.5 Thouless-Valatin Scaling . . . 58
3.4 Summary . . . 59

4 Bohr Hamiltonian Survey Results 65
4.1 Ground State Properties . . . 66
4.1.1 Minimum $\beta\gamma$ Deformations . . . 66
4.2 Excited States . . . 68
4.2.1 The Erbium Isotopic Chain . . . 68
4.2.2 First excited $E_{2_1^+}$ state . . . 78
4.2.3 First excited $E_{4_1^+}$ state . . . 79
4.2.4 First excited $E_{0_2^+}$ state . . . 81
4.2.5 $B\left(E2 : 2_1^+ \rightarrow 0_1^+\right)$ reduced transition probabilities . . . 82
4.2.6 $B\left(E2 : 4_1^+ \rightarrow 2_1^+\right)$ reduced transition probabilities . . . 83
4.3 Generalised Bohr Hamiltonian with Various (UNEDF) Functionals . . . 84
4.3.1 The Krypton Isotopic Chain . . . 84
4.3.2 $N = Z$ Nuclei . . . 87
4.3.3 ^{70}Kr and ^{70}Se Work . . . 89
4.3.4 Mass Parameters . . . 90
4.3.5 Collective Wavefunctions . . . 91

5 Summary, Conclusions and Future Work 103
5.1 Summary . . . 103
5.2 Conclusions . . . 103
5.3 Future Work . . . 104

A Mass Parameters: A More Detailed Look 106
A.0.1 Mass Parameters in Different Variables . . . 106
A.0.2 Expressions for Mass Parameters . . . 107
A.0.3 Moments of Inertia from Mass Parameters . . . 108

B The Metric Tensor 109

C The Laplace-Beltrami Operator 110

D Derivation of the Metric Tensor and the Jacobian for the Bohr Hamiltonian 112

List of Publications

Below is a list of the current publications for David Muir.

1. Muir D, Próchniak L, Pastore A and Dobaczewski J 2020 *Structure of Krypton Isotopes using the Generalised Bohr Hamiltonian Method* 27th International Nuclear Physics Conference (Preprint 2004.10835)

2. Muir D, Pastore A, Dobaczewski, Barton C J (2017) *Bootstrap Technique to Study Correlation between Neutron Skin Thickness and the Slope of the Symmetry energy in Atomic Nuclei*, Acta Physica Polonica B

3. Llewellyn R D O, Bentley M A, Wadsworth R, Iwasaki H, Dobaczewski J, de Angelis G, Ash J, Bazin D, Bender P C, Cederwall B, Crider B P, Doncel M, Elder R, Elman B, Gade A, Grinder M, Haylett T, Jenkins D G, Lee I Y, Longfellow B, Lunderberg E, Mijatović T, Milne S A, **Muir D**, Pastore A, Rhodes D and Weisshaar D (2020) Phys. Rev. Lett. **124**(15) 152501 URL `https://link.aps.org/doi/10.1103/PhysRevLett.124.152501`

List of Tables

2.1 Orbitals from the function ϕ_ν. 23
2.2 Parameter (t, x) set for UNEDF0, UNEDF1 and UNEDF1$_{\mathrm{SO}}$. 28

4.1 ^{70}Kr BH data for UNEDF0. 89
4.2 ^{70}Kr BH data for UNEDF1. 89
4.3 ^{70}Kr BH data for UNEDF1$_{\mathrm{SO}}$. 90
4.4 ^{70}Se BH data for UNEDF0. 90
4.5 ^{70}Se BH data for UNEDF1. 91
4.6 ^{70}Se BH data for UNEDF1$_{\mathrm{SO}}$. 91

List of Figures

1.1 1975 Nobel Prize in Physics Winners. 13
1.2 Nuclear structure energy scales [1]. 14
1.3 Proposed survey regions of the nuclear chart. Only even-even nuclei are considered. The rare-earth region of key interested (highlighted in green) to be surveyed is between $Z = 50 - 82$ and $N = 82 - 126$. The nuclei highlighted in red is the expanded region of calculations extending back towards the proton dripline and down to $Z = 28$ but only for known nuclei. 16

2.1 Intrinsic nuclear deformation shapes: (a) spherical nucleus, quadrupole deformation - (b) Prolate and (c) oblate - and (d) octupole deformation, where the symmetry axis is indicated by a dashed line. 30
2.2 The (β, γ) plane describing nuclear deformation. 31

3.1 Flowchart of the global computational procedure employed in the systematic study of even-even nuclei within the Bohr Hamiltonian methodology. Steps and codes highlighted in red are pre-existing standalone codes which have been incorporated into the global implementation. Steps, codes and scripts shown in violet have been solely created and implemented by David Muir in order to construct a logical and robust implementation of the methodology which can be built on in future work. Highlighted in green are outputs obtained systematically for this study and in blue we highlight the resultant isotopic chain document created to summarize these known outputs. 48
3.2 Experimental β_2 deformation parameter across the even-even nuclei of the nuclear chart [2]. 50
3.3 Experimental $E_{2_1^+}$ across the nuclear chart [2]. 51
3.4 Experimental $E_{4_1^+}$ across the nuclear chart [2]. 52
3.5 (Colour Online) Values of the deformation parameters $\beta_{\min}$ (left panel) and $\gamma_{\min}$ (right panel) at the minimum of the potential energy surfaces for the Xe isotopic chain for UNEDF0 (red) and UNEDF1$_{\mathrm{SO}}$ (blue). 53
3.6 (Colour Online) Shows the 2_1^+ (left panel) and 4_1^+ (right panel) energy spectra for the Xe isotopic chain for UNEDF0 (red) and UNEDF1$_{\mathrm{SO}}$ (blue). 54
3.7 (Colour Online) Shows the experimental (left), theoretical with scaling (sc = 1.3) and theoretical without scaling BH calculations for UNEDF0 (red/centre) and UNEDF1$_{\mathrm{SO}}$ (blue/right) energy level schemes for ^{126}Xe. . 54
3.8 (Colour Online) Convergence Tests: Potential energy surfaces for the ^{128}Xe test case with 10, 12, 14, 16, 18 and 20 shells (from top row to bottom row) for the three following mesh densities $(\beta_{\mathrm{Step}}, \gamma_{\mathrm{Step}}) = (0.100, 12^\circ)$, $(0.050, 6^\circ)$, $(0.025, 3^\circ)$ (shown left to right in the diagram above). 61
3.9 Comparison of the 2_1^+ and the 4_1^+ for different $\beta\gamma$ mesh densities in a varying number of shells. 62

3.10 Comparison of the $B(E2)$ transition probabilities for different mesh densities in a varying number of shells. 62
3.11 The (β, γ) plane sextant describing nuclear quadrupole deformation. 62
3.12 Illustration of certain states with zero or small positive energies unbound by the given potential but still bound by the Coulomb barrier. 63
3.13 (Colour Online) Experimental (left panel), theoretical with scaling (sc = 1.3) (centre panel) and theoretical (right panel) energy level schemes for ^{80}Zr with the UNEDF0 functional. 63
3.14 (Colour Online) Experimental (left panel), theoretical with scaling (sc = 1.2) (centre panel) and theoretical (right panel) energy level schemes for ^{80}Zr with the UNEDF0 functional. 64

4.1 β_{min} deformation across the nuclear chart. 66
4.2 γ_{min} deformation across the nuclear chart. 67
4.3 (Colour Online) Shows the evolution of the β_{min} (top panel) and γ_{min} (bottom panel) across the erbium isotopic chain for UNEDF0 BH calculations (red hollow circles). The light blue bands highlight the semi-magic nuclei ^{150}Er and ^{194}Er. 68
4.4 (Colour Online) Shows the evolution of the energies expressed in MeV of the first excited 2_1^+ (top panel) and 4_1^+ (bottom panel) states across the erbium isotopic chain for scaled UNEDF0 BH calculations represented by red hollow circles and unscaled UNEDF0 BH calculations represented by blue hollow circles and compare them to the experimental results [2] represented by the solid black dots. The light blue bands highlight the semi-magic nuclei ^{150}Er and ^{194}Er. 69
4.5 (Colour Online) Shows the first 2_1^+ (left panel) and 4_1^+ (right panel) theoretical energy states against the corresponding experimentally measured states [2] for scaled and unscaled UNEDF0 BH calculations. To guide the eye we add errorbars of ±100 keV (inner bound) and ±200 keV (outer bound). Highlighted in large circles is the semi-magic ^{150}Er nuclei. 70
4.6 (Colour Online) Shows the first excited 0_2^+ state predictions from scaled (red hollow circles) and unscaled (blue hollow circles) UNEDF0 BH calculations along with the known experimental states shown by solid black dots. 70
4.7 (Colour Online) A collection of the low-lying energy spectra of the erbium isotopic chain calculated using UNEDF0 BH calculations. The top panel presents the unscaled results whilst the bottom panel includes the Thouless-Valatin scaling of a factor of 1.3 of the microscopic HFB mass parameters. . 71
4.8 (Colour Online) Shows the $B\left(E2 : 2_1^+ \rightarrow 0_1^+\right)$ (top panel) and $B\left(E2 : 4_1^+ \rightarrow 2_1^+\right)$ (bottom panel) transition probabilities compared to experimental data [2] across the erbium isotopic chain for scaled (red hollow circles) and unscaled (blue hollow circles) UNEDF0 BH calculations. 73
4.9 (Colour Online) Potential energy surfaces for ^{150}Er (spherical, right), ^{158}Er (transitional, centre) and ^{166}Er (strongly deformed, left) obtained using the UNEDF0 functional. 74
4.10 (Colour Online) Shows the evolution of the energy spectra expressed in MeV as a function of angular momentum for the low-lying energy states for scaled (red hollow circles) and unscaled (blue hollow circles) UNEDF0 BH calculations. The experimental results [2] are represented by the solid black dots. The results are shown for ^{150}Er (top panel), ^{158}Er (middle panel) and^{166}Er (bottom panel). 75

4.11 (Colour Online) Shows the evolution of the energies expressed in MeV of the first excited 2_1^+ (top panel) and 4_1^+ (bottom panel) states across the erbium isotopic chain for scaled UNEDF0 BH calculations represented by red hollow circles and unscaled UNEDF0 BH calculations represented by blue hollow circles and compare them to the Gogny D1S study [3] results represented by orange hollow circles. The light blue bands highlight the semi-magic nuclei ^{150}Er and ^{194}Er. 77
4.12 2_1^+ energy spectra for the UNEDF0 BH study. 78
4.13 4_1^+ energy spectra for the UNEDF0 BH study. 79
4.14 $E_{4_1^+}/E_{2_1^+}$ ratio against $\beta_{\min}$ across the nuclear chart for the UNEDF0 BH study. 80
4.15 0_2^+ energy spectra for the UNEDF0 BH study. 81
4.16 Reduced $B\left(E2 : 2_1^+ \rightarrow 0_1^+\right)$ transition rates across the nuclear chart. 82
4.17 Reduced $B\left(E2 : 4_1^+ \rightarrow 2_1^+\right)$ transition rates across the nuclear chart. 83
4.18 (Colour Online) We represent the evolution of the energies expressed in MeV of the first excited 2_1^+ (left panel) and 4_1^+ (right panel) states across the krypton isotopic chain for the 3 functionals: UNEDF0 represented by hollow circles; UNEDF1 represented by hollow squares and UNEDF1$_{\rm SO}$ represented by hollow triangles and compare them to the experimental results [2] represented by the solid dots. The light blue bands highlight the semi-magic ^{86}Kr nucleus. 84
4.19 (Colour Online) Shows the first 2_1^+ (left panel) and 4_1^+ (right panel) theoretical energy states against the corresponding experimentally measured states [2] for all 3 UNEDF functionals represented by hollow: circles for UNEDF0; squares for UNEDF1 and triangles for UNEDF1$_{\rm SO}$. To guide the eye we add errorbars of $\pm$100 keV (inner bound) and $\pm$200 keV (outer bound). Highlighted in large circles are the semi-magic ^{86}Kr nuclei. 85
4.20 (Colour Online) Shows the $B\left(E2 : 2_1^+ \rightarrow 0_1^+\right)$ (left panel) and $B\left(E2 : 4_1^+ \rightarrow 2_1^+\right)$ (right panel) transition probabilities [2] across the Krypton isotopic chain for the 3 UNEDF functionals represented by hollow circles for UNEDF0; squares for UNEDF1 and triangles for UNEDF1$_{\rm SO}$. 85
4.21 (Colour Online) Potential energy surfaces for ^{72}Kr (top row), ^{74}Kr (middle row) and ^{76}Kr (bottom row) obtained using UNEDF0 (left column), UNEDF1 (centre column) and UNEDF1$_{\rm SO}$ (right column) functionals. . . . 87
4.22 (Colour Online) Shows the energy spectra for a number of low-lying states and their associated $B\left(E2\right)$ transition probabilities for ^{72}Kr where we show the experimental results [2] (far left panel), UNEDF0 (left centre panel), UNEDF1 (right centre panel) and UNEDF1$_{\rm SO}$ (far right panel). 87
4.23 (Colour Online) Comparison of the experimental (black dots) and theoretical (coloured squares) $B\left(E2 : 2_1^+ \rightarrow 0_1^+\right)$ transition probabilities in a variety of even-even nuclei requested by experimentalists. Unfortunately, not all functionals converged for all nuclei. Specifically, the ^{68}Se and ^{78}Sr nuclei. 88
4.24 (Colour Online) Shows the evolution of the energy spectra expressed in MeV as a function of angular momentum for the low-lying energy states for scaled (red hollow circles) and unscaled (blue hollow circles) UNEDF0 (top row), UNEDF1 (middle row) and UNEDF1$_{\rm SO}$ (bottom row) BH calculations. The experimental results [2] are represented by the solid black dots whilst states that are uncertain in terms of their angular momentum are marked as hollow black dots. The results are shown for ^{70}Kr (left panels) and ^{70}Se (right panels). 93

4.25 (Colour Online) Potential energy surfaces for ^{70}Kr (top row) and ^{70}Se (bottom row) obtained using UNEDF0 (left), UNEDF1 (centre) and UNEDF1$_{\mathrm{SO}}$ (right). 94
4.26 (Colour Online) Microscopically calculated mass parameters ($B_{\beta\beta}$, $B_{\beta\gamma}$, $B_{\gamma\gamma}$, B_x, B_y and B_z) for ^{70}Kr (top two rows) and ^{70}Se (bottom two rows) obtained using UNEDF0. 95
4.27 (Colour Online) Microscopically calculated mass parameters ($B_{\beta\beta}$, $B_{\beta\gamma}$, $B_{\gamma\gamma}$, B_x, B_y and B_z) for ^{70}Kr (top two rows) and ^{70}Se (bottom two rows) obtained using UNEDF0 with a Thouless-Valatin scaling factor of 1.3 for the mass parameters. 96
4.28 (Colour Online) Probability densities for the 0_1, 0_2, 2_1, 2_2 energy states of ^{150}Er obtained using UNEDF0. 97
4.29 (Colour Online) Collective wavefunction components for ^{150}Er obtained using UNEDF0. 97
4.30 (Colour Online) Probability densities for the 0_1, 0_2, 2_1, 2_2 energy states of ^{158}Er obtained using UNEDF0. 98
4.31 (Colour Online) Collective wavefunction components for ^{158}Er obtained using UNEDF0. 98
4.32 (Colour Online) Probability densities for the 0_1, 0_2, 2_1, 2_2 energy states of ^{166}Er obtained using UNEDF0. 99
4.33 (Colour Online) Collective wavefunction components for ^{166}Er obtained using UNEDF0. 99
4.34 (Colour Online) Probability densities for the 0_1, 0_2, 2_1, 2_2 energy states of ^{72}Kr obtained using UNEDF0. 100
4.35 (Colour Online) Collective wavefunction components for ^{72}Kr obtained using UNEDF0. 100
4.36 (Colour Online) Probability densities for the 0_1, 0_2, 2_1, 2_2 energy states of ^{72}Kr obtained using UNEDF1. 101
4.37 (Colour Online) Collective wavefunction components for ^{72}Kr obtained using UNEDF1. 101
4.38 (Colour Online) Probability densities for the 0_1, 0_2, 2_1, 2_2 energy states of ^{72}Kr obtained using UNEDF1$_{\mathrm{SO}}$. 102
4.39 (Colour Online) Collective wavefunction components for ^{72}Kr obtained using UNEDF1$_{\mathrm{SO}}$. 102

Acknowledgements

I would like to dedicate my thesis and the work contained herein to the five most influential people in my life to date in getting me to this point in my career - my immediate family: Sarah Muir (Sister), Hannah Muir (Sister), Robert Muir (Father), Elaine Muir (Mother) and Irene Davis (Grandmother). Throughout my life I have been privileged to be supported and encouraged by all of my friends, family and colleagues but no-one more than these people. I would like to thank each one for their time, support and encouragement in aiding me to where I am today.
I would like to extend my profound thanks to both of my supervisors - Dr Alessandro Pastore and Professor Jacek Dobaczewski - for their time, effort and faith in me as a PhD candidate as well as their continued support and encouragement. I hope to stay in close collaboration in the years to come with you both. I wish to thank Leszek Próchniak for his collaboration over the course of this project, without whom this project would not have succeeded. Leszek has offered incredible support throughout my PhD and has been vital in guiding my understanding of this interesting field of study.
In addition, I would like to thank my thesis advisory panel (TAP) members - Professor Rex Godby and Professor David Jenkins - as well as all of the staff and students I have had the pleasure of interacting and collaborating with at the University of York throughout my PhD. I would like to give a special mention to Professor Alison Laird and Professor Mike Bentley for both offering me their time and support during my time at the university of York.
Finally, I must make a special mention to two of my closest friends - Dr Amy Skelt and Dr Angela Daisley. Amy and I met through our PhD studies in physics at the University of York and has become a great friend of mine. Her support was invaluable and it was a pleasure to return the favour to her when I could. Angela has been one of my closest friends for many years and similarly has always been an incredibly supportive friend and a pleasure to know. I wish both of you the very best.
I wish all of the people above as well as those who have helped me at various other points in my life well in their lives and careers and hope to stay both friends and colleagues with them in the future.

Declaration

I declare that this thesis is a presentation of original work and I am the sole author. This work has not previously been presented for an award at this, or any other, University. All sources are acknowledged as References.

I declare that this PhD thesis is an original piece of academic work in the field of theoretical nuclear physics carried out by David Muir during his PhD at the University of York (2016-2021). References, citations and acknowledgements throughout this document are widely used to give credit and merit to those individuals, publications and collaborations who have aided in my research activities and more specifically, the construction of this thesis. This work has not been previously submitted for an award at this, or any other, university.

1. I declare the use of the unpublished Bohr Hamiltonian code of my collaborator Leszek Próchniak along with his edited version of the published HFODD code (version 2.49t) without which I could not have carried out this project. I built on top of both of these pre-existing codes generating original data included in chapter 3 and 4 of this thesis.

2. HFODD249t computational nuclear physics code. This was utilised extensively in the project.
   Schunck N, Dobaczewski J, McDonnell J, Satu la W, Sheikh J, Staszczak A, Stoitsov M and Toivanen P 2012 *Computer Physics Communications* **183** 166 - 192 ISSN 0010-4655 URL `http://www.sciencedirect.com/science/article/pii/S0010465511002852`

3. Experimental data from the National Nuclear Data Center was mined and used for comparison with my original work in chapters 3 and 4.
   National Nuclear Data Center, Brookhaven National Laboratory URL `https://www.nndc.bnl.gov/`

4. Bohr Hamiltonian Gogny D1S study data was extracted from the following reference, more specifically their online database, again for the purposes of comparison with my original work in chapter 4.
   Delaroche J P, Girod M, Libert J, Goutte H, Hilaire S, Peru S, Pillet N and Bertsch G 2009 *Physical Review C* **81**

5. An experimental collaboration I was part of published the reference below and I have included experimental data from this collaboration in chapter 4 in order to compare this work to experimental data.
   Llewellyn R D O, Bentley M A, Wadsworth R, Iwasaki H, Dobaczewski J, de Angelis G, Ash J, Bazin D, Bender P C, Cederwall B, Crider B P, Doncel M, Elder R, Elman B, Gade A, Grinder M, Haylett T, Jenkins D G, Lee I Y, Longfellow B, Lunderberg E, Mijatović T, Milne S A, Muir D, Pastore A, Rhodes D and Weisshaar D 2020 *Phys. Rev. Lett.* **124**(15) 152501 URL `https://link.aps.org/doi/10.1103/PhysRevLett.124.152501`

6. New experimental data mined from the publication below and was included in chapter 4 of this thesis. Again this was for comparison reasons between the model presented in this work and the mined experimental data.
   Wimmer K, Korten W, Doornenbal P, Arici T, Aguilera P, Algora A, Ando T, Baba H, Blank B, Boso A, Chen S, Corsi A, Davies P, de Angelis G, de France G, Delaroche J P, Doherty D T, Gerl J, Gernhäuser R, Girod M, Jenkins D, Koyama S, Motobayashi T, Nagamine S, Niikura M, Obertelli A, Libert J, Lubos D, Rodríguez

T R, Rubio B, Sahin E, Saito T Y, Sakurai H, Sinclair L, Steppenbeck D, Taniuchi R, Wadsworth R and Zielinska M 2021 *Phys. Rev. Lett.* **126**(7) 072501 URL `https://link.aps.org/PhysRevLett.124.152501`

7. I have included work from the following conference proceeding in which I was lead author. This work was a direct consequence of the main thesis project and is included in chapter 4.
   Muir D, Próchniak L, Pastore A and Dobaczewski J 2020 *Structure of Krypton Isotopes using the Generalised Bohr Hamiltonian Method* 27th International Nuclear Physics Conference (Preprint 2004.10835)

Signed,
David Muir

Note: Graphs of the nuclear chart are used throughout this work. Formatting data in such plots is a challenge to make them clear in all formats. The sizing of the points in these graphs were chosen so that they print well with each nucleus evenly spaced and identifiable. Where possible, I strongly recommend printing the graphs. Obviously, if you are viewing this material online then the formatting is dependent on the size of your screen, the zoom chosen and the preference of each reader.

Chapter 1

Introduction and Aims

In 1975 the Nobel Prize in Physics [4] was award to Aage Bohr (1.1a), Ben Roy Mottelson (1.1b) and Leo James Rainwater (1.1c) for their discovery of the connection between single particle motion and collective motion within atomic nuclei. This intensified the discussion of collective properties of nuclei and set the challenge of accurately modelling such phenomena. As with all scientific endeavours the maximum amount of analytical rigour is sought when looking to model any phenomenon. However, as is well documented in a variety of fields, a "from first principles approach" may not be practical due to either the complexity of the problem (as is the case in most quantum field theories) or simply the ability to carry out the necessary computations associated with a given approach. This often leads to a diverse range of theoretical models being developed in an attempt to better examine the phenomenon under scrutiny. Typically, each approach will be built on appropriate degrees of freedom to describe a particular length and/or energy scale accurately. For example, classical Newtonian physics is a good description of the everyday macroscopic world involving extended massive objects travelling slow relative to an observer. Refinements made by Einstein in his theory of special relativity and later his general theory of relativity are necessary extensions in understanding fast moving objects and large scale gravitational systems respectively. Conversely, in going to microscopic objects quantum mechanics has a key role to play in our understanding of nature. Interestingly, quantum mechanics provides a completely new perspective into the fundamental working of reality and accurately describes the interactions of the fundamental particles within the standard model of particle physics [5].

(a) Aage Bohr (1922-2009)

(b) Ben Roy Mottelson (1926-Present)

(c) Leo James Rainwater (1917-1986)

Figure 1.1: 1975 Nobel Prize in Physics Winners.

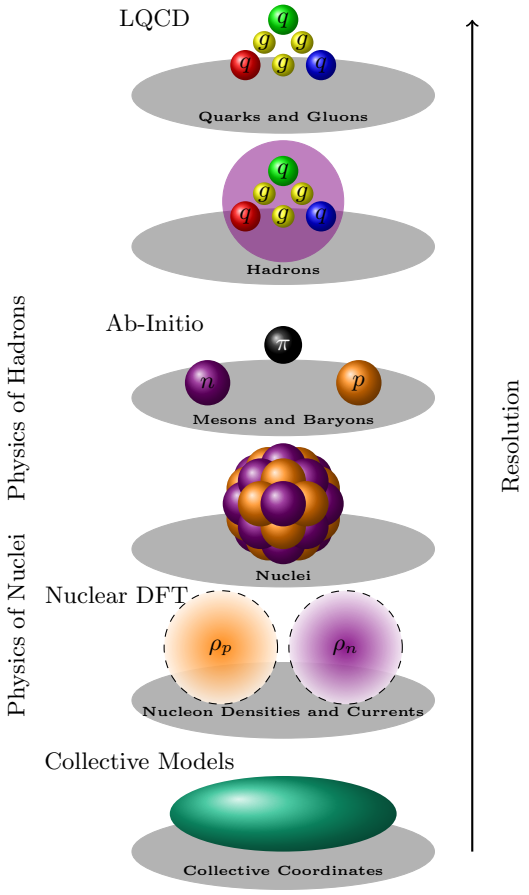

Figure 1.2: Nuclear structure energy scales [1].

When it comes to the field of nuclear physics it is a well documented problem of what degrees of freedom are relevant to describe a variety of nuclear structure phenomena [6]. Let's begin by examining the structure of nuclei. Every nucleon is composed of 3 quarks bound by the strong nuclear force mediated by gluon interactions [5]. Nuclear structure encompasses many phenomena at various energy scales from fundamental constituents of the standard model of particle physics (quarks and gluons) through constituent nucleons (protons and neutrons) to nuclei (bound groups of such nucleons) to density functional calculations based on washing the individual nucleon structure out to express the nucleus purely as a proton and a neutron density to the collective excitations (multipole moments) associated with the collective motions of many nucleons as represented in figure 1.2
Figure 1.2 shows the various approaches and resolution scales examined within the field of nuclear physics from a fundamental description of quarks and gluons as governed by quantum chromodynamics through theories of discrete properties of individual protons and neutrons, for example the shell model and liquid drop model on to density functional theory approaches culminating in collective properties of the nucleus as a whole of which the Bohr Hamiltonian is a prime example.

The most accurate and analytical theory of these interactions comes from quantum chromodynamics (QCD). QCD governs the structure of the protons and neutrons which themselves form bound systems of nucleons called nuclei which in turn bind electrons forming atoms giving rise to all visible matter in the universe. Analytical techniques such as lattice quantum chromodynamics (LQCD) and chiral effective field theories informed from QCD are applicable to few nucleon systems and extending these to systems of a large number of particles is very complicated and currently beyond our abilities [7]. Next is the so-called ab-initio approaches which mixes various theoretical models and aims to inform

itself, as much as possible, by fundamental approaches such as interactions obtained from chiral effective field theories and build on the physics of fundamental few-body systems and extend this through some approximation to heavier systems. This has been a very successful endeavour but still faces limitations for medium-to-heavy mass nuclei. All of these computational models along with their implementations via codes and pseudocodes describing a variety of nuclear physics phenomena along with their associated strengths and limitations are discussed extensively in [8]. Additionally, connections from first principles to the collective phenomena of many-particle systems still remains phenomenological for such approaches. Hence, we must explore other alternatives and nuclear density functional theory (NDFT) is a prime candidate. The technical details of this approach will be summarised here and discussed in further detail in the next chapter.
The main principle behind this approach lies in elementary quantum mechanics - *the variational principle*. At its core NDFT relies on expressing nuclear ground state properties in terms of the nucleon (proton and neutron) densities and their derivatives in constructing an energy density functional (for all intents and purposes this is our effective nucleon-nucleon interaction) and minimizing the energy through a Hartree-Fock (HF) or Hartree-Fock-Bogoliubov (HFB) procedure. This approach has the key benefit of being applicable across the nuclear chart as it is less computationally demanding than various other theories whilst by definition, as far as ground state properties are concerned, should provide an upper bound on the true energy of a given system. Depending on the task at hand any (and perhaps multiple) of these descriptions may be applicable or it may be the case that you simply restrict yourself to a particular nuclear property at a given energy scale which is itself a good approximation to the phenomena under examination. Additionally, there is scope to connect each resolution scale to one another and strengthen the connection between different theoretical descriptions of nuclear phenomena. In this thesis an attempt is made to do exactly that by connecting the density functional theory approach to that of collective excitations of a variety of nuclei.

1.1 The Research Project

Now that we have chosen an appropriate nuclear theory (NDFT) applicable across the nuclear chart we will outline the proposed research project. The main goal of this research is to examine the validity of the Generalised Bohr Hamiltonian (GBH) approach in describing collective quadrupole excitations of nuclei in the rare-earth region of the chart using a Skyrme functional - UNEDF0 - where the mass parameters are calculated via constrained HFB calculations. Figure 1.3 shows the proposed scale for the systematic survey of even-even nuclei. The grey points show all currently known nuclei present in the chart, the blue points indicate the even-even nuclei which are able to be studied via the current Bohr Hamiltonian approach and the green points indicate the rare-earth region of the chart which provides the basis for this systematic study. Over the course of the project this region expanded to include the red points also. Not all of these nuclei are included in the final results of this thesis for reasons discussed in the computational implementation chapter. However, over 450 nuclei in 20 isotopic chains are included from this proposed region.
The work presented here aims to address the following key questions:

1. Can the Bohr Hamiltonian approach reproduce the trends of the low-lying 2_1^+ and 4_1^+ states in even-even medium-to-heavy mass nuclei?

2. Can the Bohr Hamiltonian reproduce the trends associated with the electromagnetic transition rates $B\left(E2 : 4_1^+ \rightarrow 2_1^+\right)$ and $B\left(E2 : 2_1^+ \rightarrow 0_1^+\right)$ across the medium-to-heavy mass region of the nuclear chart?

3. What impact does the choice of functional have on the spectra and electromagnetic transition rates when calculated within the Bohr Hamiltonian approach?

Further benefits of the thesis, in addition to addressing the above key questions, include:

1. Offering direct support to nuclear experiment by the direct calculation of experimental observables such as energy spectra and electromagnetic transition rates for direct comparison with experimental observations.

2. Offering a region of prediction to future years exploration of the nuclear chart in currently unexplored regions - particularly in neutron rich nuclei moving towards the neutron dripline in the rare-earth region ($Z = 50$ to $Z = 82$).

3. Creation of a Bohr Hamiltonian results database and provide the basis for further theoretical studies such as the impact of pairing strengths on the approach and associated uncertainty analysis within the Bohr Hamiltonian approach.

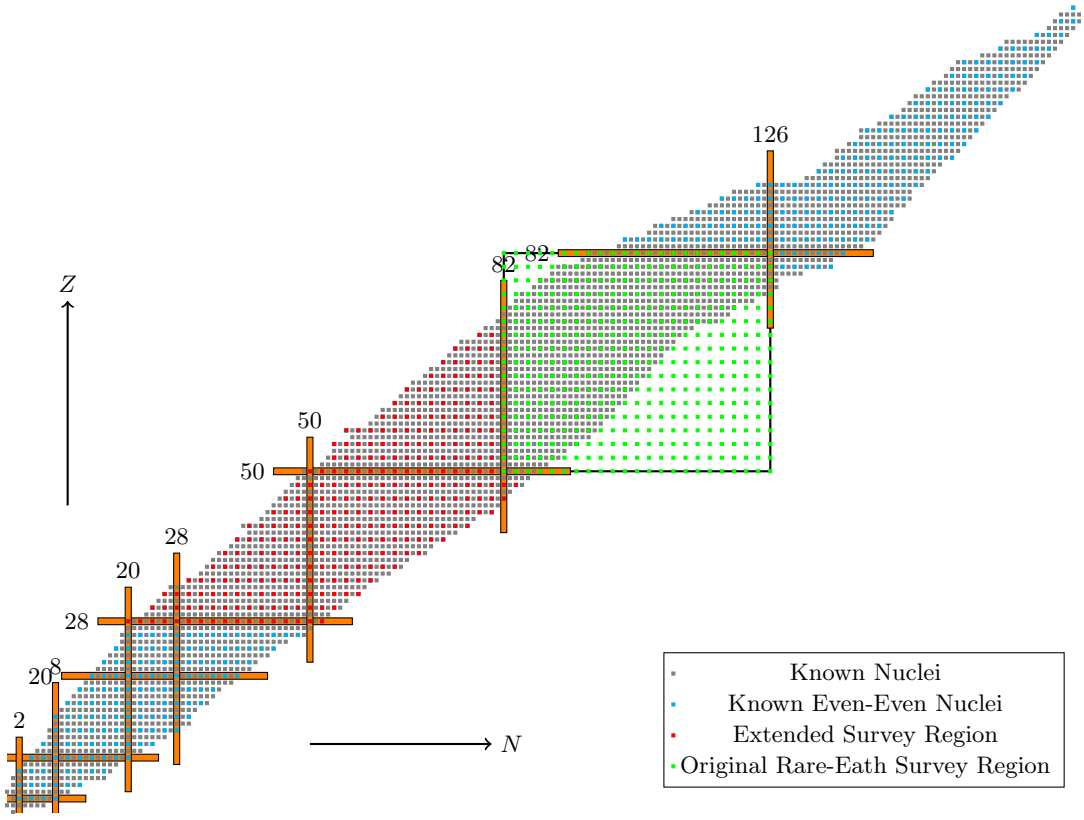

Figure 1.3: Proposed survey regions of the nuclear chart. Only even-even nuclei are considered. The rare-earth region of key interested (highlighted in green) to be surveyed is between $Z = 50 - 82$ and $N = 82 - 126$. The nuclei highlighted in red is the expanded region of calculations extending back towards the proton dripline and down to $Z = 28$ but only for known nuclei.

1.2 Thesis Structure

In chapter 2 the background theory required for this study is discussed. The chapter outlines the quantum many-body problem, summarises DFT for electronic systems and highlights distinctions with NDFT. It introduces the concept of constrained HFB calculations and the notion of Adiabatic Time-Dependent Hartree-Fock-Bogoliubov (ATDHFB) calculations. It summarises the concept of nuclear deformation, in particular quadrupole deformation, as well as discussing the choice of Skyrme functional used for the systematic survey. The chapter culminates in a derivation of the collective model of Bohr and Mottelson.
Chapter 3 builds on these theoretical foundations and the previous computational work in this area. It discusses the construction of the robust automated procedure implemented in order to carry out such systematic calculations for the proposed study. It presents several benchmarks and discusses both the computational difficulties and advances made in this work.
Chapter 4 presents the results of the systematic survey. It begins by outlining ground state properties via global plots before examining a particular case from the centre of the rare-earth region - the erbium isotopic chain. This chain is examined in terms of low-lying energy spectra and $B(E2)$ transition rates both of which are compared to the known experimental data. The evolution of the potential energy surface across the chain is also examined. Then the global results for the low-lying energy spectra are presented along with their associated $B(E2)$ transition rates. Following this, the krypton isotopic chain is examined for 3 UNEDFs to examine the impact the choice of functional may have on the BH approach. Finally, the chapter concludes with support provided to the nuclear physics community over the survey project examining subgroups of nuclei of particular interest to collaborators. Specifically, work was done on a group of even-even $N = Z$ nuclei and some preliminary work is presented on the mirror nuclei ^{70}Kr and ^{70}Se.
Finally, chapter 5 summaries the research project and draws the main conclusions from this work before highlighting multiple interesting extensions which could follow as future work.

Chapter 2

Background Theory

This chapter details a variety of key concepts along with a historical summary of their development in scientific literature. From the quantum many-body problem to density functional theory (DFT) applicable to electronic systems and further to how nuclear density functional theory (NDFT) is similar in approach yet fundamentally different in practice in its ability to describe nuclear observables. Following this we introduce and describe the nuclear functionals of particular interest in terms of this research and outline the key aspects of describing deformed nuclear systems.

2.1 Quantum Many-Body Problem

The principles at the heart of quantum mechanics exist throughout nature at all length and energy scales. However, quantum phenomena are observable on microscopic scales such as molecular, atomic and particle scales and not observable on macroscopic scales of people, planets and stars. The scale for quantum effects is set by the smallness of Planck's constant $h = 6.63 \times 10^{-34}$Js, a fundamental constant of nature. Therefore understanding the theory and applications of quantum mechanics is a key pursuit of physics. Quantum mechanics is used in a multitude of scientific research endeavours but is particularly rife in fields such as quantum chemistry, condensed matter physics, nuclear physics and particle physics.
Initially in physics one-body systems of electrons were studied in great detail analytically. Whilst this is in and of itself a key stepping stone in understanding the role quantum mechanics plays in nature it's applicability to complex structures of nuclei, atoms and molecules is somewhat limited. It is well reported that with regards to the single electron in orbit around a single proton we can analytically solve the hydrogen atom by means of separation of variables and our implementation of spherical harmonics. Beyond such a simple system, solving many-body systems becomes complicated and approximations are needed along with numerical calculations in order to successfully describe them.
One example for electron based systems is that introduced in the Hohenberg-Kohn (HK) theorem [9] which itself leads to the resultant field of density functional theory [10]. This has proved to be highly successful in quantum chemistry and condensed matter physics. Below is a summary discussion of many-body electronic systems.

2.2 Many Particle Problem in Electronic Systems

This section discusses a summary of DFT for many-body electronic systems and their associated theoretical descriptions built from [10] [11] and [12]. This section provides a brief introduction to the key concepts of the approach which will be edited in the following

discussions on nuclear density functional theory (NDFT) necessary for implementing the proposed research project.

2.2.1 The Born-Oppenheimer Approximation

The Born-Oppenheimer Approximation states that

$$m_{\text{nucleus}} \gg m_e, \tag{2.1}$$

where m_{nucleus} is the mass of the nucleus and m_e is the mass of the electron. This approximation essentially states that the dynamics of atoms (nuclei and electrons) can be separated into the dynamics of the nuclei and then separately the dynamics of the electrons. The ground state energy E is a unique functional of the energy density:

$$E = E\left[n\left(\mathbf{r}\right)\right]. \tag{2.2}$$

A functional is a function of a function i.e. an integral is a functional

$$I\left[f\left(x\right)\right] = \int f\left(x\right) dx. \tag{2.3}$$

The electron density that minimizes the energy of the overall functional is the true ground state electron density.

$$E\left[n\left(\mathbf{r}\right)\right] > E_0\left[n_0\left(\mathbf{r}\right)\right]. \tag{2.4}$$

Now we are forced to ask the question: what is the energy density functional? Well it must have the following form

$$E\left[\{\psi_i\}\right] = E_{\text{known}}\left[\{\psi_i\}\right] + E_{\text{XC}}\left[\{\psi_i\}\right], \tag{2.5}$$

where $E_{\text{known}}\left[\{\psi_i\}\right]$ is the known energy density functional consisting of the kinetic energy term(s) and the potential energy term(s) associated with the Coulomb interactions within the system. The explicit form of the known functional term is as follows

$$E_{\text{known}}\left[\{\psi_i\}\right] = -\frac{\hbar}{m_e}\sum_i \int \psi_i^* \nabla^2 \psi_i d^3r + \int V\left(\mathbf{r}\right) n\left(\mathbf{r}\right) d^3r + \frac{e^2}{2}\int\int \frac{n\left(\mathbf{r}\right) n\left(\mathbf{r}'\right)}{\mathbf{r}-\mathbf{r}'} d^3r d^3r' + E_{\text{ion}}. \tag{2.6}$$

Then we have the exchange-correlation functional $E_{\text{XC}}\left[\{\psi_i\}\right]$ which is not known. It is true that there is a perfect/exact functional whose composition is formed out of these two functionals but this is also unknown to us. The exchange-correlation functional includes all of the quantum mechanical terms and interactions. Since this is unknown it must be approximated in all calculations.

2.2.2 Hartree-Fock Atomic Energy

To begin a simple discussion on the key idea of the approach we begin with a toy model which is spinless. Of course in reality fermions (electrons like nucleons) are not spinless but to guide our discussion this model helps in introducing the key ideas which are extended later on. Starting from a Slater determinant for the wave function,

$$\psi\left(1,2,\ldots,N\right) = \frac{1}{\sqrt{N!}}\begin{vmatrix} \psi_1\left(\mathbf{r}_1\right) & \psi_2\left(\mathbf{r}_1\right) & \cdots & \psi_N\left(\mathbf{r}_1\right) \\ \psi_1\left(\mathbf{r}_2\right) & \psi_2\left(\mathbf{r}_2\right) & \cdots & \psi_N\left(\mathbf{r}_2\right) \\ \vdots & \vdots & \ddots & \vdots \\ \psi_1\left(\mathbf{r}_N\right) & \psi_2\left(\mathbf{r}_N\right) & \cdots & \psi_N\left(\mathbf{r}_N\right) \end{vmatrix}, \tag{2.7}$$

which is $3N$-dimensional in construction ($\mathbf{r} = (x, y, z)$). We also recall the antisymmetry property

$$\psi(1,2) = -\psi(2,1), \tag{2.8}$$

applies to interchanging any two electrons. Then we can consider the Hamiltonian operator (in atomic units i.e. where factors of $\hbar, m_e, 4\pi\varepsilon_0$ etc. are all equal to 1)

$$\hat{H} = \sum_{i=1}^{N} -\frac{1}{2}\nabla_i^2 + \sum_{i=1}^{N} -\frac{Z}{r_i} + \sum_{i=1}^{N}\sum_{j>i}^{N} \frac{1}{r_{ij}}, \tag{2.9}$$

where the first term represents the kinetic energy, the second represents the potential energy associated with the attractive Coulomb interaction between each electron and the nucleus and the third term represents the electron's repulsion to one another.
Now assuming a normalised orthogonal wavefunction, which we are, then the total energy of the system is given by

$$\begin{aligned} E &= \langle \psi(1,2,\ldots,N) | \hat{H} | \psi(1,2,\ldots,N) \rangle \\ &= \int d^3\mathbf{r}_1 \int d^3\mathbf{r}_2 \cdots \int d^3\mathbf{r}_N \psi^*(\mathbf{r}_1, \mathbf{r}_2, \ldots, \mathbf{r}_N) \hat{H} \psi(\mathbf{r}_1, \mathbf{r}_2, \ldots, \mathbf{r}_N) \\ &= \underbrace{\sum_{i=1}^{N} h_i}_{\text{1-electron term}} + \underbrace{\sum_{i=1}^{N}\sum_{j>i}^{N} (J_{ik} - K_{ij})}_{\text{2-electron term}}, \end{aligned} \tag{2.10}$$

where

$$h_i = \int d^3\mathbf{r}_1 \psi_i^*(\mathbf{r}_1) \hat{h}_i \psi(\mathbf{r}_1), \tag{2.11}$$

where

$$\hat{h}_i = -\frac{1}{2}\nabla_i^2 - \frac{Z}{r_i} \tag{2.12}$$

and J_{ij} are the matrix elements of the Coulomb interaction given by

$$J_{ij} = \int\int d^3\mathbf{r}_1 d^3\mathbf{r}_2 \psi_i^*(\mathbf{r}_1) \psi_j^*(\mathbf{r}_2) \frac{1}{r_{12}} \psi_i(\mathbf{r}_1) \psi_j(\mathbf{r}_2), \tag{2.13}$$

which can be interpreted classically as the electron repulsion of two different electrons. Finally, the exchange integral K_{ij} involves exchanging the last two ψ terms in the Coulomb interaction as follows

$$K_{ij} = \int\int d^3\mathbf{r}_1 d^3\mathbf{r}_2 \psi_i^*(\mathbf{r}_1) \psi_j^*(\mathbf{r}_2) \frac{1}{r_{12}} \psi_i(\mathbf{r}_2) \psi_j(\mathbf{r}_1). \tag{2.14}$$

This exchange integral is really a quantum effect and has no classical analogue.
If $i = j$ then $J_{ii} = K_{ii}$ and therefore the second term is zero i.e. electrons do not interact with themselves.

2.2.3 Hartree-Fock Operators

These ψs are eigenfunctions (and their corresponding eigenvalues) of the *Fock operator* $\hat{F}$ are given by

$$\hat{F}(\mathbf{r}_1) = \hat{h}(\mathbf{r}_1) + \underbrace{\sum_{i=1}^{N} \left(\hat{J}_i(\mathbf{r}_1) - \hat{K}_i(\mathbf{r}_1) \right)}_{\hat{V}_{\text{eff}}(\mathbf{r}_1)}. \tag{2.15}$$

Now

$$\hat{F}(\mathbf{r}_1)\,\psi_i(\mathbf{r}_1) = \varepsilon_i \psi_i(\mathbf{r}_1), \quad i = 1, 2, \ldots, N \tag{2.16}$$

i.e. there is a Fock operator for every electron in the system, in this case the formula depicts the i^{th} where ε_i is the orbital energy of the i^{th} electron where the energy is given by the following expectation value

$$\begin{aligned}\varepsilon_i &= \int d^3\mathbf{r}_1 \psi_i^*(\mathbf{r}_1)\,\hat{F}(\mathbf{r}_1)\,\psi_i(\mathbf{r}_1) \\ &= h_i + \sum_{j=1}^{N}(J_{ij} - K_{ij}).\end{aligned} \tag{2.17}$$

Now if we sum all of the orbital energies of each electron then we obtain

$$\sum_{i=1}^{N}\varepsilon_i = \sum_{i=1}^{N} h_i + \sum_{i=1}^{N}\sum_{j=1}^{N}(J_{ij} - K_{ij}). \tag{2.18}$$

So the total Hartree-Fock energy E_{HF} is given by

$$E_{HF} = \sum_{i=1}^{N} h_i + \frac{1}{2}\sum_{i=1}^{N}\sum_{j=1}^{N}(J_{ij} - K_{ij}), \tag{2.19}$$

where we have divided by a factor of two in order to remove the double counting of the two electron interaction terms as in practice we must realise that we can only count them once if we are to have a physically correct and consistent answer.

2.2.4 Hartree-Fock Spin

Now we will include the spin of the electron (fermions)

$$\begin{aligned}h_1 &= \int d^3\mathbf{r}_1 \psi_i^*(\mathbf{r}_1)\,\hat{h}_i\psi_i(\mathbf{r}_1)\int d\sigma\sigma^*(\omega_1)\,\sigma(\omega_1) \\ &= h_i\langle\sigma_1|\sigma_1\rangle \\ &= h_i \quad \text{since } \langle\sigma_1|\sigma_1\rangle = 1.\end{aligned} \tag{2.20}$$

Spin does not affect our 1-electron terms. Now for our 2-electron terms we have

$$\begin{aligned}J_{ij} &= \int d^3\mathbf{r}_1 \int d^3\mathbf{r}_2 \psi_i^*(\mathbf{r}_1)\,\psi_i(\mathbf{r}_1)\,\frac{1}{r_{12}}\psi_i^*(\mathbf{r}_2)\,\psi_i(\mathbf{r}_2)\int d\sigma\sigma^*(\omega_1)\,\sigma(\omega_1)\int d\sigma\sigma^*(\omega_2)\,\sigma(\omega_2) \\ &= [ii|jj]\,\langle\sigma_1|\sigma_1\rangle\langle\sigma_2|\sigma_2\rangle \\ &= J_{ij},\end{aligned} \tag{2.21}$$

which is also unaffected for the coulomb interaction. Let's now consider the exchange interaction term

$$\begin{aligned}K_{ij} &= \int d^3\mathbf{r}_1 d^3\mathbf{r}_2 \psi_i^*(\mathbf{r}_1)\,\psi_j(\mathbf{r}_1)\,\frac{1}{r_{12}}\psi_j^*(\mathbf{r}_2)\,\psi_i(\mathbf{r}_2)\int d\sigma\sigma_i^*\sigma_j\int d\sigma\sigma_j^*\sigma_i \\ &= [ij|ij]\,\langle\sigma_1|\sigma_2\rangle\langle\sigma_2|\sigma_1\rangle \\ &= [ij|ij]\,\delta_{\sigma_1\sigma_2}\delta_{\sigma_2\sigma_1}.\end{aligned} \tag{2.22}$$

Firstly, we note that each electron in each shell has both its kinetic term and its potential term generated by the nucleus. Hence, we have 2 electrons in the ψ_1 state resulting in

a factor of $2h_1$ (observe that the different spins are irrelevant in this factor as previously outlined). The same argument applies for the ψ_2 state i.e. we get a factor of $2h_2$ and there is only one electron in the ψ_3 state resulting in a factor of h_3. Now we can consider 2-electron terms. The two electrons in the 1s orbital repel each other resulting in a factor of J_{11}. Then each electron in orbital 1s are repelled by each of the electrons (2 electrons) in orbital 2s giving rise to a $4J_{12}$ term, given that there are four interactions here (up up $\uparrow\uparrow$, down down $\downarrow\downarrow$, up down $\uparrow\downarrow$ and down up $\downarrow\uparrow$). Now we can consider the exchange interactions between both up spins and both down spins in the 1s and 2s orbitals respectively. These give rise to the term $2K_{12}$. Similarly we construct the same arguments in order to consider the remaining Coulomb and exchange interaction between other pairs of electrons. Now we can write the Hartree-Fock energy as

$$E_{HF} = 2h_1 + 2h_2 + h_3 + J_{11} + 4J_{12} - 2K_{12} + 2J_{13} - K_{13} + 2J_{23} - K_{23}. \tag{2.23}$$

2.2.5 Hartree-Fock Roothaan Procedure/Equations

Now we will consider how to implement these ideas in practice and calculate both the orbital and total energy of electrons within an atom. This method is called the *Hartree-Fock Roothaan Procedure* or the *Hartree-Fock Roothaan equations*.
Firstly, we will expand the wavefunctions in terms of base functions

$$\psi_i(\mathbf{r}_1) = \sum_{\nu=1}^{K} c_{\nu i}\phi_\nu(\mathbf{r}_1), \tag{2.24}$$

where we have a choice of ϕ_ν which could take any of the following forms but typically, since the solution of the hydrogen atom is analytical, it is often a good choice to start with this solution for this orbital and vary it accordingly. Hence, our choices for $\phi_\nu(\mathbf{r}_1)$

$$\phi_\nu(\mathbf{r}_1) = Nx^a y^b z^c e^{-\zeta r}, \tag{2.25}$$

which is known as a Slater function. Alternatively we could use a *Gaussian orbital* of the form

$$\phi_\nu(\mathbf{r}_1) = Nx^a y^b z^c e^{-\zeta r^2}, \tag{2.26}$$

where N is some constant, the indices a, b and c are integers and ζ is some exponent dependent on what we pick for the basis function. Note that equation 2.25 is better in terms of the asymptotics of the wavefunction whereas equation 2.26 is more advantageous in terms of simplifying the evaluation of the matrix elements. For an s-orbital $a = b = c = 0$. The orbital angular momentum quantum number l is given by

$$l = a + b + c. \tag{2.27}$$

Note that these are strictly Cartesian base coordinates but it is possible to convert them to the spherical polar coordinates typically used to solve the hydrogen atom.
Now let us explore applying the Fock operator to this expansion

$$\hat{F}\left[\sum_{\nu=1}^{K} c_{\nu i}\phi_\nu(\mathbf{r}_1)\right] = \varepsilon_i\left[\sum_{\nu=1}^{K} c_{\nu i}\phi_\nu(\mathbf{r}_1)\right]. \tag{2.28}$$

Simplifying this by multiplying by ϕ^* and integrating over $\mathbf{r}$ gives

$$F_{\mu\nu} = \int d^3\mathbf{r}_1 \phi^*_\mu(\mathbf{r}_1)\hat{F}\phi_\nu(\mathbf{r}_1), \tag{2.29}$$

Table 2.1: Orbitals from the function ϕ_ν.

Orbital	l	Options
s	$l=0$	$a=b=c=0$
p	$l=1$	$a=1$ or $b=1$ or $c=1$
d	$l=2$	Any two of a, b and c can be 1 or any can be equal to 2.
f	$l=3$	etc.

where μ and ν may represent two different basis functions for the right-hand-side of our earlier expression. Now for the left-hand-side we obtain an "overlap matrix"

$$S_{\mu\nu} = \int d^3\mathbf{r}_1 \phi_\mu^* (\mathbf{r}_1)\, \phi_\nu (\mathbf{r}_1)\,. \tag{2.30}$$

Hence, we obtain

$$\sum_\nu c_{\nu i} F_{\mu\nu} = \varepsilon_i \sum_\nu c_{\nu i} S_{\mu\nu}. \tag{2.31}$$

Therefore,

$$F\mathbf{c} = \varepsilon S\mathbf{c}, \tag{2.32}$$

where F is the Fock matrix whose elements are the $F_{\mu\nu}$ integrals, $\mathbf{c}$ is a vector composed of the coefficients $c_{\nu i}$ and represents a single atomic orbital for some atom, ε is the orbital energy and finally S is an overlap matrix composed of the $S_{\mu\nu}$ integrals. Equation(s) (2.32) are known as the *Hartree-Fock Roothaaan equations.*
Points to note: we have K basis functions and hence F and S are $K \times K$ matrices; we would have K total orbitals; we would have N occupied spin orbitals for N electrons and finally we would have $K - N$ virtual spin orbitals i.e. orbitals with no electron in them.

2.2.6 Kohn-Sham Equations

The *Kohn-Sham* equation is the Schrödinger equation for a fictitious system of non-interacting particles (typically electrons in quantum chemistry and condensed matter physics and nucleons/nuclei in nuclear and atomic physics) which generate the same density as any given system of interacting particles. We define the Kohn-Sham potential $V_{\text{eff}}(\mathbf{r})$ as a local effective potential governing how the non-interacting particles move. Due to the fact that the particles under consideration are non-interacting fermions, the Kohn-Sham wavefunction may be represented by a single Slater determinant comprising of a set of orbitals which are the lowest energy solution of

$$\left(-\frac{\hbar^2}{2m}\nabla^2 + V_{\text{eff}}(\mathbf{r})\right)\psi_i(\mathbf{r}) = \varepsilon_i \psi_i(\mathbf{r})\,, \tag{2.33}$$

where ε_i is the energy of the $\psi_i{}^{\text{th}}$ orbital.
Now it is possible to construct the (charge) density $\rho(\mathbf{r})$ of an N-particle system from this definition which yields

$$\rho(\mathbf{r}) = \sum_i^N |\psi_i(\mathbf{r})|^2. \tag{2.34}$$

In density functional theory (using the Kohn-Sham equations) the total energy of a system $E[\rho]$ is expressed as a functional of the charge density as follows

$$E[\rho] = T_s[\rho] + \int d\mathbf{r} V_{\text{ext}}(\mathbf{r}) \rho(\mathbf{r}) + E_H[\rho] + E_{\text{XC}}[\rho], \tag{2.35}$$

where T_s is the Kohn-Sham kinetic energy given in terms of the orbital by

$$T_s[\rho] = \sum_{i=1}^{N} \int d\mathbf{r} \psi_i^*(\mathbf{r}) \left(-\frac{\hbar^2}{2m}\nabla^2\right) \psi_i(\mathbf{r}), \tag{2.36}$$

and V_{ext} is the external potential acting on the interacting system (at a minimum, for a molecular system, the electron-nucleus interaction), E_H is the Hartree (or Coulomb) energy given by

$$E_H = \frac{e^2}{2} \int d\mathbf{r} \int d\mathbf{r}' \frac{\rho(\mathbf{r}) \rho(\mathbf{r}')}{|\mathbf{r} - \mathbf{r}'|}, \tag{2.37}$$

and finally E_{XC} is the exchange correlation energy. The Kohn-Sham equations are found by means of varying the total energy expression with respect to the set of orbitals in order to obtain the Kohn-Sham potential

$$V_{\text{eff}} = V_{\text{ext}}(\mathbf{r}) + e^2 \int \frac{\rho(\mathbf{r}')}{|\mathbf{r} - \mathbf{r}'|} d\mathbf{r}' + \frac{\delta E_{\text{XC}}[\rho]}{\delta \rho(\mathbf{r})}, \tag{2.38}$$

where the last term is defined as the exchange-correlation potential as follows

$$V_{XC}(\mathbf{r}) \equiv \frac{\delta E_{\text{XC}}[\rho]}{\delta \rho(\mathbf{r})}. \tag{2.39}$$

The exchange correlation term and the corresponding energy expression are the only unknowns in the Kohn-Sham approach to density functional theory. It is possible to make an approximation where you choose not to vary the orbitals and this is known as *Harris functional theory.*

Finally, the Kohn-Sham orbital energies ε_i generally have very little physical meaning - see Koopmans' theorem. The sum of the total energies ε_i is related to the total energy by the following expression

$$E = \sum_{i}^{N} \varepsilon_i - E_H[\rho] + E_{\text{XC}}[\rho] - \int \frac{\delta E_{\text{XC}}[\rho]}{\delta \rho(\mathbf{r})} \rho(\mathbf{r}) d\mathbf{r}. \tag{2.40}$$

Again by Koopmans' theorem because the orbital energies are non-unique (i.e. degenerate) in the more general restricted open-shell case, this equation only holds for specific choices of the orbital energies.

Given that the HK theorem is applicable to many particle systems of fermions it should in principle be applicable to nucleons and therefore such an approach may be able to model nuclei successfully. Triumph! Sadly this is not the case. There are several additional complications in applying such an approach to nuclear systems in place of electronic systems which are eloquently discussed in [13] and summarised briefly in the following sections.

2.3 Hartree-Fock-Bogoliubov (HFB) Theory

Until now the discussion has been restricted to electronic systems of many electrons. In principle, the same formalism could be applied to nuclei however, now we have two species

of particle - the proton and the neutron - but this is not enough to describe the ground state properties of atomic nuclei due to the presence of pairing correlations. These correlations emerge systematically from experimental nuclear data for example in the observation of odd-even mass staggering of nuclear binding energies [14]. In order to describe such pairing effects it is necessary to extend the aforementioned HF procedure to the HFB procedure. The concept of pairing in nuclear physics is an in depth and ongoing discussion however from [15] there has been much work on the analogous concept of describing nuclear excitation spectra similarly to the description of states in a superconducting metal.
In HFB theory we invoke the so-called Bogoliubov transformation [14] which is the most general linear transformation from the particle creation and annihilation operators $c_l^\dagger$ and c_l to the quasi-particle operators $\beta_k^\dagger$ and β_k which are given by

$$\beta_k^\dagger = \sum_l U_{lk} c_l^\dagger + V_{lk} c_l, \tag{2.41}$$

where the indices k and l run over the whole configuration space and the $\beta_k^\dagger$ operator creates a mixture of particles and holes with some probability amplitude (U_{lk}, V_{lk}). This subsequently, defines a new vacuum state for our system

$$\beta_k \left|\Phi\right\rangle = 0, \tag{2.42}$$

where β_k is simply the hermitian conjugate of $\beta_k^\dagger$. In principle, the HFB formalism takes into account the pairing of nuclei via a pairing matrix Δ (neutron-neutron pairing, proton-proton pairing and current research work is under way in the community to address the problem of proton-neutron pairing). Subsequently, we can derive an expression for the HFB matrix which can be diagonalized and reduces to a simple eigenvalue problem as follows

$$\begin{pmatrix} h_0 - \lambda\hat{O} & \Delta \\ -\Delta^* & -h_0^* + \lambda\hat{O} \end{pmatrix} \begin{pmatrix} U_k \\ V_k \end{pmatrix} = \begin{pmatrix} U_k \\ V_k \end{pmatrix} \cdot E_k, \tag{2.43}$$

where h_0 is the Hartree-Fock Hamiltonian, the columns U_k and V_k belong to the matrices U and V which determine the quasi-particle operator $\beta^\dagger$ and E_k is the eigenvalue energy of the system obtained from solving the above eigenvalue problem. It can be observed in the case of zero pairing ($\Delta = 0$) the HFB formalism reduces to the HF formalism. The crucial note here is that as the Bogoliubov transformation mixes particles and holes, the number of particles is no longer conserved in this formalism. Clearly it is necessary to impose a condition on the system to preserve, on average, the particle number. This leads to the concept of a constrained HFB calculation where Lagrange multipliers λ are used to constrain various observables $\hat{O}$ such as particle number and in the case of this work the quadrupole moments which will be discussed more in the remainder of this chapter.

2.4 Nuclear Density Functional Theory (NDFT)

Nuclear density functional theory (NDFT) is built from the same underlying principle of the HK theorem describing a system of many interacting fermions. Given nucleons can themselves be considered as spin-1/2 particles i.e. fermions the same approach should, in principle, be applicable. However, there are a number of complexities that exist moving from electronic DFT to nuclear DFT.
The most obvious difference between the two approaches is that in electronic DFT there is one species of fermion - the electron - whilst in nuclear DFT their are two - the proton and neutron. This difference can be handled via the introduction of an additional quantum number - isospin - allowing us to consider generic nucleons within our calculations where

the protons and neutrons themselves are distinguished via the isospin quantum number. At this point it is noteworthy to point out that the Coulomb interaction of course distinguishes the proton from the neutron given the proton carries an overall charge where the neutron does not. However, given that protons and neutrons interact via the strong force and given our current understanding of the standard model of particle physics the strong interaction between a pair of protons, a pair of neutrons and between a proton and a neutron are all the same, this simplification in discussing the strong interactions between nucleons is a useful one.
One key difference is that treatment of the spin degree of freedom between the two theories. In electronic DFT the main contributing factor to the success of the approach is the particle positions resulting in other degrees of freedom - specifically the spin - being summed over as a local density and emerging as a statistical factor not imperative to the fundamental calculations. In nuclear physics this picture is far more complex. NDFT is built on the aforementioned HFB procedure with an associated effective nucleon-nucleon interaction represented by a density functional. These non-relativistic functionals broadly fall into 2 main families of functionals - *Skyrme* [16] and *Gogny* [17]. The families of these functionals have the same underlying mathematical structure designed to incorporate a variety of physical phenomena required to accurately describe nuclei. The coupling constants associated with each of the terms are fitted from experimental data for a selection of different nuclei and are often adjusted to best fit a particular observable property of nuclei such as binding energies or radii. The following subsections outline both the basic structure of the Skyrme and Gogny type family of functionals. There are a diverse range of functionals which currently exist within the domain of nuclear physics. These functionals widely fall into several classes of functionals, often referred to as families, built from an underlying functional generator fitted on experimental data to account for various physical phenomenon. The ultimate aim of these functionals is to model such properties of nuclei globally - typically binding energies and radii.
However, there are some classes of functionals which differ from the family structure by explicitly dropping, adding or editing the family structure. This is the case in functionals where the standard Skyrme terms have been extended to higher order in momenta. Another more crucial example of editing the standard functional form is that of the UNEDF family of functionals. Rather than include an explicit 3-body term in the functional a density dependent term is added to act as a 3-body term ([18] and [19]) in an attempt to simplify the computational implementation of the functional. The combined HFB approach and the underlying numerical implementation of NDFT calculations are detailed in [20].

2.4.1 The Skyrme Interaction

During the course of this research the Skyrme family of functionals are used in all calculations. This way we can use a functional which is well described and has been studied for several decades allowing the focus to be on implementing the computational method of using the Bohr Hamiltonian (BH) along with HFB calculations to describe collective excited states. This functional invokes the use of Dirac delta functions (i.e. it is a zero range interaction) which considerably simplifies the computations required and thus, dramatically reduces the computational time to compute the result.
The proposed Skyrme interaction is an effective interaction with a three-body term given by [14]

$$V = \sum_{i<j} V(i,j) + \sum_{i<j<k} V(i,j,k)\,. \tag{2.44}$$

It is important to stress here that the 3-body term above is usually not implemented in numerical calculations but is mimicked by a 2-body density dependent term. The basic form of this (2-body) interaction is a short range expansion of the form

$$\begin{aligned} V(1,2) = & \, t_0 (1 + x_0 P^\sigma) \delta(\mathbf{r}_1 - \mathbf{r}_2) \\ & + \frac{1}{6} t_3 (1 + x_3 P^\sigma) \rho_0^\gamma ((\mathbf{r}_1 + \mathbf{r}_2)/2) \delta(\mathbf{r}_1 - \mathbf{r}_2) \\ & + \frac{1}{2} t_1 (1 + x_1 P^\sigma) \left[\delta(\mathbf{r}_1 - \mathbf{r}_2) \mathbf{k}^2 + \mathbf{k}'^2 \delta(\mathbf{r}_1 - \mathbf{r}_2) \right] \\ & + t_2 (1 + x_2 P^\sigma) \mathbf{k}' \delta(\mathbf{r_1} - \mathbf{r}_2) \mathbf{k} \\ & + i W_0 \left(\boldsymbol{\sigma}^{(1)} + \boldsymbol{\sigma}^{(2)} \right) \cdot \left[\mathbf{k}' \times \delta(\mathbf{r}_1 - \mathbf{r}_2) \mathbf{k} \right], \end{aligned} \tag{2.45}$$

where P^σ is defined as the spin exchange operator and $\mathbf{k} = (1/\hbar)\mathbf{p}$ is the operator of relative momentum acting to the right

$$\mathbf{k} = \frac{1}{2i} (\boldsymbol{\nabla}_1 - \boldsymbol{\nabla}_2) \tag{2.46}$$

and $\mathbf{k}'$ is the complex conjugate acting to the left. The t_3 term is a 2-body density dependent term which mimics the role/effects of the 3-body term [18] in order to simplify the computational implementation. The constants contained within the Skyrme functional simulate the nuclear interaction that the nucleons within the nucleus feel. The t_0 term describes a pure δ-force with a spin exchange; t_1 and t_2 are used to simulate an effective interaction range while the fifth term of equation (2.45) represents a two-body spin-orbit interaction. The six constants - t_0, t_1, t_2, t_3, x_0 and W_0 - are chosen based on fits of experimental data of binding energies and radii of nuclei and γ is the power of the density dependent term which is fixed for the UNEDFs. Different fits naturally result in different versions of the Skyrme functional to be created whilst all of them follow the same general form. Given that this interaction is one of the most general forms of an effective interaction it is unsurprising that a family of Skyrme functionals has subsequently been constructed depending on their particular application.

Why were Skyrme functionals chosen for this work? Simply put, they are widely accepted by the nuclear theory community as a strong approach to describing the nucleon-nucleon interactions present within the nucleus. There are a couple of reasons for their confidence in this viewpoint. Firstly, Vautherin and Brink [14] were able to reproduce both the binding energies and the nuclear radii across the entire periodic table with this functional. It is important to note that different fits reproduce experimental data to different accuracies and no one fit best describes all observables to any one standard uncertainty. Furthermore, the general form of the functional is one of the more mathematically simple consisting of delta functions making it computationally more favourable than other more complicated functionals. This brings us to the choice of functional for the systematic survey - the UNEDF sub-family of functionals. These were constructed in an attempt to find an optimal universal nuclear energy density functional applicable for use in both nuclear structure and nuclear reaction calculations. The key benefit of this sub-family of Skyrme functionals is that the proton and neutron pairing strengths are fit on experimental data and unlike most Skyrme functionals not subject to alterations or fine-tuning. To be clear, referring to alterations and fine-tuning I explicitly mean that no further scaling or additional numerical parameters are added or free to be altered until better agreement with experiment is reached. The UNEDF parameters are fixed. Hence, this allows a constraint to be placed on one of the many factors that may influence the BH calculations and fix it at a set value. Furthermore, given that the functional has been adjusted to describe a variety of nuclear observables across the nuclear chart it is a prime candidate to

Table 2.2: Parameter (t, x) set for UNEDF0, UNEDF1 and UNEDF1$_{\mathrm{SO}}$.

Parameters	UNEDF0 [21]	UNEDF1 [22]	UNEDF1$_{\mathrm{SO}}$ [23]	Units
t_0	-1883.68781034	-2078.32802326	-2078.32802326	MeVfm^3
t_1	277.50021224	239.40081204	239.40081204	MeVfm^5
t_2	608.43090559	1575.11954190	1575.11954190	MeVfm^5
t_3	13901.94834463	4263.64624708	4263.64624708	MeVfm$^{3+3\gamma}$
x_0	0.00974375	0.05375692	0.05375692	-
x_1	-1.77784395	-5.07723238	-5.07723238	-
x_2	-1.67699035	-1.36650561	-1.36650561	-
x_3	-0.38079041	-0.16249117	-0.16249117	-
b_4	125.16100000	38.36807206	79.529	MeVfm^5
b'_4	-91.2604000	71.31652223	16.916	MeVfm^5
γ	0.32195599	0.27001801	0.27001801	-
V_0^n	-176.796	-186.065	-191.1	MeVfm^3
V_0^p	-203.255	-206.580	-235.3)	MeVfm^3

test the ability of the BH approach in modelling quadrupole collectivity across the chart. Each of the UNEDF functionals are subtly different in their construction. In the case of the UNEDFs they use equation 2.45 as a functional generator where the coupling constants of the functionals have been fitted independently [21] [22] [23] and are summarised in table 2.2. We see from this that the spin-orbit W_0 cannot be mapped in a straight forward way as in equation 2.45 hence, for the UNEDF sub-family we introduce parameters b_4 and b'_4 to replace the more standard W_0 with the so-called relativistic spin-orbit [24]. Finally, with regards to the UNEDF sub-family form, the pairing energy density is given by

$$\breve{\chi}(\mathbf{r}) = \sum_{q=n,p} \frac{V_0^q}{2} \left[1 - \frac{1}{2}\frac{\rho(\mathbf{r})}{\rho_0}\right] \breve{\rho}^2(\mathbf{r}), \tag{2.47}$$

where $\breve{\rho}(\mathbf{r})$ is the local pairing density and $\rho_0 = 0.16$ fm^{-3}. In addressing the main aim of the project one must be chosen for the systematic survey. Given the success of UNEDF0 in reproducing binding energies and radii across a vast array of nuclei it presents itself as a strong candidate. It is fit on experimental data from across the nuclear chart, with multiple nuclei from the same regions as this proposed study. Furthermore, this functional is not explicitly fitted using any deformation parameters and has not been built intentionally to accurately describe nuclear deformation properties such as the quadrupole moments. Although, deformed nuclei are included in the fitting of the parameters. Hence, this is an ideal functional to examine the BH approach with and identify how accurate this procedure can be given it was not specifically built for describing such deformations. Therefore, if good agreement is reached with experimental data, then it shows that explicitly fitting terms in future functionals to account for accurately reproducing nuclear deformation is unnecessary. Instead these collective phenomena can be reproduced by collective calculations rather than forcing functionals to reproduce the experimental trends themselves and we move closer to identifying the key physics phenomena that must be accounted for in the functional without constraining every parameter explicitly.

Finally, for selected chains of nuclei, predominately at experimental request, multiple UNEDF functionals are used for calculations - UNEDF0, UNEDF1 and UNEDF1$_{\mathrm{SO}}$. UNEDF1 is fit on different (heavier) nuclei to that of UNEDF0 and includes stronger proton and neutron paring strengths as a result. UNEDF1$_{\mathrm{SO}}$ is identical to UNEDF1 apart from the pairing strengths are stronger again and there is a difference in the strength of the spin-orbit term in the functional. These calculations were attempted in order to diversify

the theoretical calculations of any nuclei under analysis and aid in the discussion regarding the choice the impact of functional has on the results of BH calculations. Given the computational cost (see chapter 3) and the time restraints of this project it was not possible to reproduce the entire survey region with all 3 functionals but this work is ongoing. UNEDF2 was not considered as it includes tensor terms which drastically complicate this current computation process and is therefore out of scope for the current work.

2.4.2 The Gogny Interaction

Despite the success of the Skyrme interaction there is a particular criticism of it which is simply the doubt amongst theorists as to whether the zero range description can adequately model long range or even intermediate range parts of the realistic effective interaction. To this end, the Gogny family of functionals [14] replaces the t_0, t_1 and t_2 terms in the Skyrme functional with two Gaussians with spin-isopin exchange mixtures which leads to an interaction of the form

$$\begin{aligned} V(1,2) = &\sum_{i=1}^{2} e^{-(\mathbf{r}_1-\mathbf{r}_2)^2/\mu_i^2} \left(W_i + B_i P^\sigma - H_i P^\tau - M_i P^\sigma P^\tau\right) \\ &+ iW_0 \left(\boldsymbol{\sigma}_1 + \boldsymbol{\sigma}_2\right) \mathbf{k}^{'} \times \delta\left(\mathbf{r}_1 - \mathbf{r}_2\right) \mathbf{k} \\ &+ t_3 \left(1 + P^\sigma\right) \delta\left(\mathbf{r}_1 - \mathbf{r}_2\right) \rho^{1/3} \left(\frac{1}{2}\left(\mathbf{r}_1 + \mathbf{r}_2\right)\right). \end{aligned} \tag{2.48}$$

This is an example of a finite-range interaction which does not diverge in the pairing channel [25]. The Gogny force is included here for completeness as a similar investigation to this one was carried out previously using the Gogny D1S interaction [3] along with other supporting works [26] [27].

2.5 Nuclear Deformation

Excitation spectra for even-even nuclei up to $\sim$ 2 MeV are typically interpreted as rotations and vibrations of the nucleus. In this collective model framework an even-even nucleus is regarded as a piece of homogeneous nuclear matter - a quantum droplet of deformable matter. Unsurprisingly, the larger the number of nucleons in the nucleus, the more pronounced the collective effects are in that nucleus.
There are multiple collective excitations of nuclei corresponding to a variety of shapes (see figure 2.1) the nucleus may take in the intrinsic frame of reference. These are modernly described by multipole moments λ. It is a misconception that most nuclei are spherical in shape. Most exhibit some form of weak deformation with the deformations becoming more pronounced the heavier the nucleus is. This brings us to the different types of deformation nuclei can exhibit [28]. The monopole $\lambda = 0$ mode corresponds to the so-called breathing mode of the nucleus. The dipole $\lambda = 1$ mode corresponds the the trivial centre-of-mass translation of the nucleus. The quadrupole $\lambda = 2$ mode corresponds to the nucleus being deformed in shape to have a clear and unique axis of symmetry taking either a prolate (rugby ball/American football) type shape shown in figure 2.1(b) or an oblate (squashed sphere or pumpkin) type shape shown in figure 2.1(c). Given the axis of symmetry this allows the nucleus, in the intrinsic frame, to undergo vibrations and rotations which can ultimately be viewed from their measured energy spectra. Equally spaced energy spectra corresponds to vibrational states of the nucleus and rotational spectra are represented by an increasing separation of their energy spectra. Nuclear quadrupole deformation is the most common type of deformation across the nuclear chart and is pronounced in medium-to-heavy mass nuclei. Hence, this dictates the regions of exploration examined in this

study and given it is the most rife collective excitation the nucleus exhibits it clarifies why it is of keen interest to examine it robustly within the BH framework. For completeness, there are higher degrees of deformation such as the octupole $\lambda = 3$ mode corresponding to a pear-like shape of the nucleus shown in figure 2.1(d) which have been experimentally measured as well as more exotic hexadecapole $\lambda = 4$ modes which are yet to be observed experimentally.
Quadrupole deformation can be described through various parametrisations. Typically, as stated above, through it's quadrupole moments. In reality there are 5 parameters $\alpha_{2,\mu}$, $\mu = -2, -1, 0, 1, 2$ used to describe quadrupole deformation but in practice it is always possible to undergo a suitable rotation and arrive in the body-fixed frame where these simplify to two independent parameters: $\alpha_{2,0} \neq 0$, $\alpha_{2,-2} = \alpha_{2,2} \neq 0$ and $\alpha_{2,-1} = \alpha_{2,1} = 0$. These quadrupole moments are perfectly valid in describing the nuclear quadrupole shape. However, the BH itself is parametrised in terms of different deformation parameters and hence it is a choice to re-express these quadrupole moments as follows:

$$\alpha_{2,0} = \beta \cos(\gamma) \tag{2.49}$$

$$\alpha_{2,2} = \frac{1}{\sqrt{2}} \beta \sin(\gamma) \tag{2.50}$$

$$\Rightarrow \beta^2 = \sum_{\mu} |\alpha_{2,\mu}|^2 = \alpha_{2,0}^2 + 2\alpha_{2,2}^2. \tag{2.51}$$

Now the deformation is expressed in the polar plane where β is the radius and measures the strength of deformation i.e. how pronounced this deformation is and γ is an angle measure away from axiality i.e. γ corresponds to the shape of the nucleus. Figure 2.2 shows that by symmetry arguments it is possible to fully describe nuclear quadrupole deformation in the first sextant (where $\gamma = 0°$ represents a pure prolate shape to $\gamma = 60°$ representing a pure oblate shape). Every angle in between 0° and 60° represents a triaxial nucleus - a nucleus with no clear axis of symmetry. These sextants are commonly referred to as potential energy surfaces (PES) and will parametrise our constrained HFB BH calculations for the study. This will be discussed more in the chapter on computational implementation.

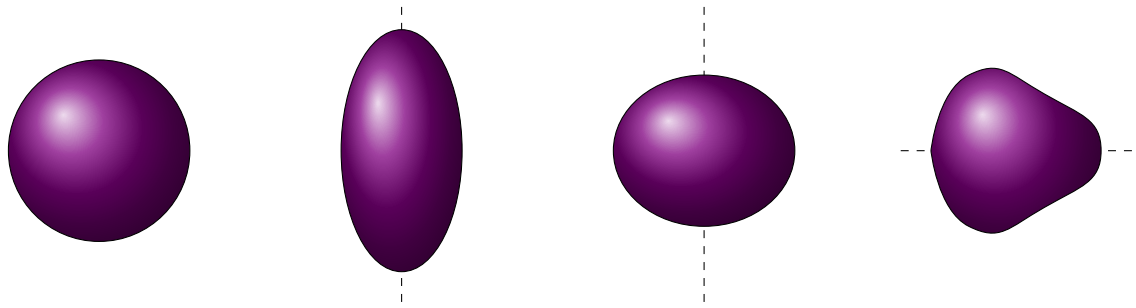

(a) Spherical (b) Quadrupole: Prolate (c) Quadrupole: Oblate (d) Octupole (Pear-like shape)

Figure 2.1: Intrinsic nuclear deformation shapes: (a) spherical nucleus, quadrupole deformation - (b) Prolate and (c) oblate - and (d) octupole deformation, where the symmetry axis is indicated by a dashed line.

This brings us to a pivotal point in our discussion of nuclear deformation. Are nuclei truly deformed? The short answer is yes. All nuclei across the nuclear chart are intrinsically deformed systems albeit the strength of this deformation can vary greatly across the nuclear chart. Deformation is unsurprisingly weaker in lighter systems and stronger in heavier systems as highlighted earlier and experimentally we observe that semi-magic and doubly magic nuclei generally have a weak (sometimes spherical) deformation. In the

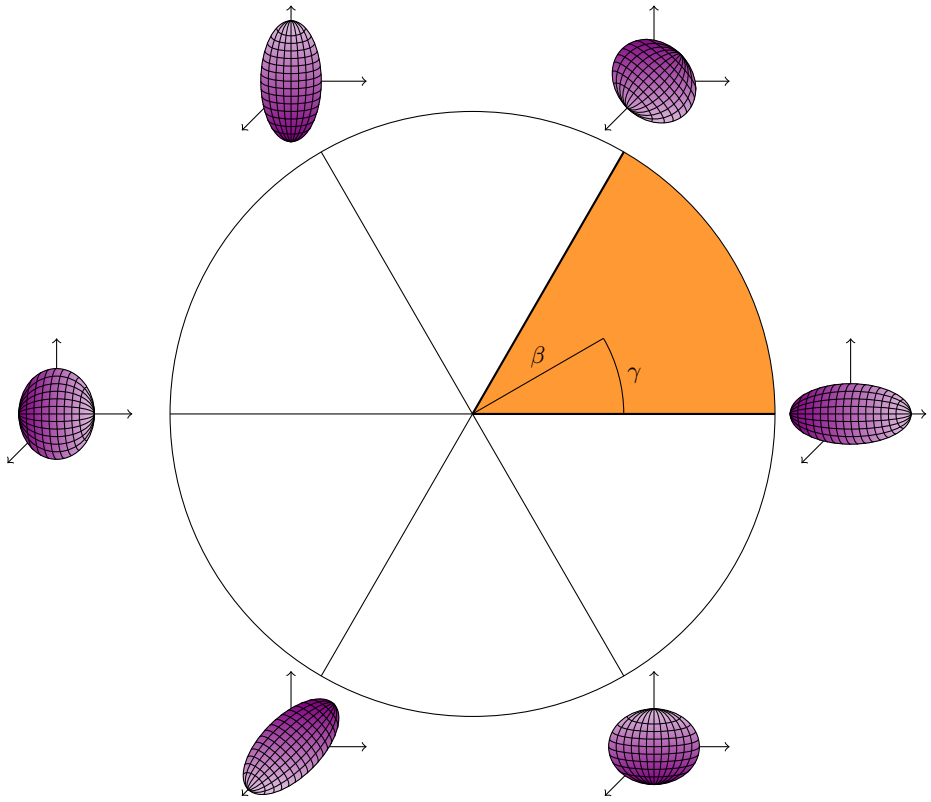

Figure 2.2: The (β, γ) plane describing nuclear deformation.

following work much discussion is make in terms of theoretical calculations of nuclei made in the intrinsic frame which may differ from the ground state experimental measurements made of nuclei in the laboratory frame. Over the years this has raised arguments between nuclear physicists as to whether nuclei are truly deformed in nature or if this is some artefact of mean-field calculations.
Furthermore, recent research summarised in a review article regarding symmetry-restoration in mean-field approaches [29] highlights that deformation is intrinsic within the domain of quantum mechanics where the ideas of quantum dots are developed. In the reported experiments a quantum dot (a well defined potential well) is created within a crystal which can hold a precise number of electrons due to the Pauli exclusion principle. Through various experimental manipulations of these particles it is observed at one level the system has a "washed out" symmetry associated with the system manifesting itself as a symmetric ring (see appendix J of [29] for further details). However, it is possible through detailed measurements to identify the underlying intrinsic density and probability distributions with the system which break the symmetry. This is of course a more complicated picture when we examine nuclei and current feasibility prevents us from these measurements directly. Nonetheless, this provides strong experimental evidence that these intrinsic deformations are not merely an artefact of the mean-field approach. Furthermore, another simplistic argument can be made. As far as quantum mechanics is concerned a sphere cannot undergo rotation. In order for this to occur we require a well-defined axis of symmetry about which the nucleus could rotate giving rise to rotational spectra.

2.6 ATDHFB Theory

The adiabatic approximation is valid when the collective motion of the nucleons is slow compared with the single-particle motion in the system. The applicability of this approx-

imation to all nuclei is debatable given a lack of understanding of the dynamics of nuclei. One way to gauge where this approximation does well is to implement the following BH study and look for areas of strong agreement with experiment and areas of discrepancies too. This will ultimately be the fastest and most useful methodology in evaluating the robustness of such an approximation.

2.6.1 The ATDHFB Equation

The time-dependent Hartree-Fock-Bogoliubov (TDHFB) method is an approximate method used to study the time evolution of a many-body fermion system which can be derived from the variational principle which is the topic of this subsection. In the following derivation we set $\hbar = 1$.

$$\delta\langle\Psi|i\frac{d}{dt} - \hat{H}|\Psi\rangle = 0, \tag{2.52}$$

where $\hat{H}$ is the many-body Hamiltonian given by

$$\hat{H} = \sum_{\mu\nu} T_{\mu\nu}\beta^\dagger_\mu\beta_\nu + \frac{1}{4}\sum_{\mu\nu\gamma\delta} V_{\mu\nu\gamma\delta}\beta^\dagger_\mu\beta^\dagger_\nu\beta_\delta\beta_\gamma \tag{2.53}$$

and $|\Psi\rangle$ denotes the vacuum state for the set of quasiparticle annihilation operators β_ν. These operators are related to the particle creation and annihilation operators by the Bogoliubov transformation

$$\beta_\nu = \sum_\mu \left(U^*_{\mu\nu}c_\mu + V^*_{\mu\nu}c^\dagger_\mu\right).$$

A full discussion on the ATDHF methodology along with an extensive derivation as applied to finite systems is discussed at length in [30], what follows is a summary of the ATDHFB approach used in this work which was obtained from [14]. Given a generalised density matrix R of the form

$$R = \begin{pmatrix} \rho & -\kappa \\ \kappa^* & 1-\rho^* \end{pmatrix}, \tag{2.54}$$

where

$$\rho_{\mu\nu} = \langle\Psi|c^\dagger_\nu c_\mu|\Psi\rangle = \left(V^*V^T\right)_{\mu\nu} \tag{2.55}$$

$$\kappa_{\mu\nu} = \langle\Psi|c_\nu c_\mu|\Psi\rangle = \left(V^*U^T\right)_{\mu\nu} \tag{2.56}$$

and where W is the self-consistent Hamiltonian given by

$$W = \begin{pmatrix} T+\Gamma-\lambda I & \Delta \\ -\Delta^* & -T^*-\Gamma^*+\lambda I \end{pmatrix}, \tag{2.57}$$

where T is the kinetic energy, λ is the chemical potential and both Γ and Δ are self-consistent potentials. It is possible to state a differential equation for the generalised density matrix R which is equivalent to the variational equation (2.52) given by the following expansion

$$R = e^{i\chi}R_0e^{-i\chi} \simeq R_0 + R_1 + R_2, \tag{2.58}$$

yielding the ATDHFB equations:

$$i\dot{R}_0 = [h_0, R_1] + [\Gamma_1, R_0] \tag{2.59}$$

$$i\dot{R}_1 = [h_0, R_0] + [\Gamma_1, R_1] + [\Gamma_2, R_0], \tag{2.60}$$

where the zeroth order in χ gives the static case $\dot{R}_0 = 0$ and $[W_0, R_0] = 0$ as highlighted in section 2.7.4.

$$i\dot{R} = [W, R]. \tag{2.61}$$

2.7 Mass Parameters

The following section is a combined summary, discussion and development of unpublished notes on mass parameters [31]. These are what the constrained HFB calculations will ultimately yield as input to the BH.

2.7.1 HFB In a Different Notation

For the following sections various matrix manipulations are required and so from here on we define all quantities as are illustrated here. The Bogoliubov transformation is given by

$$\mathcal{B} = \begin{pmatrix} U^\dagger & V^\dagger \\ V^T & U^T \end{pmatrix} \tag{2.62}$$

$$\Rightarrow \mathcal{B}^\dagger = \begin{pmatrix} U & V^* \\ V & U^* \end{pmatrix}. \tag{2.63}$$

Eigenvectors of the generalised density matrix R are expressed as follows. We define matrices of dimension $M \times 2M$

$$\phi = \begin{pmatrix} V^* \\ U^* \end{pmatrix} \tag{2.64}$$

$$\chi = \begin{pmatrix} U \\ V \end{pmatrix}, \tag{2.65}$$

given that matrices U and V are of dimension M. The matrices ϕ and χ are eigenvectors of the matrix R ([31] and [32])

$$R = \phi\phi^\dagger \tag{2.66}$$

$$R\phi = \phi \tag{2.67}$$

$$R\chi = 0. \tag{2.68}$$

More precisely columns ϕ_μ and χ_μ are eigenvectors of the one-particle Hamiltonian H_0

$$H_0\phi_\mu = -E_\mu\phi_\mu \tag{2.69}$$

$$H_0\chi_\mu = E_\mu\chi_\mu \tag{2.70}$$

$$H_0\phi = -\phi E \tag{2.71}$$

$$H_0\chi = \chi E. \tag{2.72}$$

2.7.2 Basics of Mass Parameters

Given (n) collective variables q_k for example, the quadrupole moments discussed previously, it is possible to implement a constrained HFB calculation within the ATDHFB framework by evaluating the ATDHFB equations as follows

$$i\hbar\dot{q}_k\frac{\partial R_0}{\partial q_k} = \left[H_1\left(R_1^{(k)}, R_0\right)\right] + \left[H_0, R_1^{(k)}\right]. \tag{2.73}$$

The basic expression for mass parameters is given by

$$B_{kj} = \frac{i\hbar}{2\dot{q}_j}\mathrm{Tr}_{2M}\left(R_1^j\left[\frac{\partial R_0}{\partial q_k}, R_0\right]\right), \tag{2.74}$$

where $\mathrm{Tr}\,()$ is the trace of the matrix in parenthesis. We can define the following mathematical expression

$$F_k = \mathcal{B}\partial_k R_0\mathcal{B}^\dagger, \tag{2.75}$$

where ∂_k is a partial derivative with respect to the collective variable indexed by k. Now using the Bogoliubov transformation matrix for R_0 i.e.

$$\mathcal{B}R_0\mathcal{B}^\dagger = P_0 = \begin{pmatrix} 0 & 0 \\ 0 & \mathbb{I} \end{pmatrix}. \tag{2.76}$$

Hence, we can obtain a matrix form of F_k as follows

$$F_k = \begin{pmatrix} 0 & f_k \\ \tilde{f}_k & 0 \end{pmatrix}, \tag{2.77}$$

where

$$\tilde{f}_k = -f_k^*. \tag{2.78}$$

Analogously we can define

$$Z_j = \mathcal{B}R_1^{(j)}\mathcal{B}^\dagger, \tag{2.79}$$

yielding

$$Z_j = \begin{pmatrix} 0 & z_j \\ -z_j^* & 0 \end{pmatrix}. \tag{2.80}$$

Thus, we can calculate the trace in the quasiparticle basis by remembering that $\mathcal{B}$ is unitary i.e. $\mathcal{B}\mathcal{B}^\dagger = \mathbb{I}$ as follows

$$\begin{aligned}
\mathrm{Tr}_{2M}\left(\mathcal{B}R_1^j\left[\frac{\partial R_0}{\partial q_k}, R_0\right]\mathcal{B}^\dagger\right) &= \mathrm{Tr}_{2M}\left(\mathcal{B}R_1^j\mathcal{B}^\dagger\mathcal{B}\left[\frac{\partial R_0}{\partial q_k}, R_0\right]\mathcal{B}^\dagger\right) \\
&= \mathrm{Tr}_{2M}\left(\mathcal{B}R_1^j\mathcal{B}^\dagger\mathcal{B}\left(\frac{\partial R_0}{\partial q_k}R_0 - R_0\frac{\partial R_0}{\partial q_k}\right)\mathcal{B}^\dagger\right) \\
&= \mathrm{Tr}_{2M}\left(\mathcal{B}R_1^j\mathcal{B}^\dagger\left(\mathcal{B}\frac{\partial R_0}{\partial q_k}\mathcal{B}^\dagger\mathcal{B}R_0\mathcal{B}^\dagger - \mathcal{B}R_0\mathcal{B}^\dagger\mathcal{B}\frac{\partial R_0}{\partial q_k}\mathcal{B}^\dagger\right)\right) \\
&= \mathrm{Tr}_{2M}\left(Z_j\left(F_kP_0 - P_0F_k\right)\right) \\
&= \mathrm{Tr}_{2M}\left(Z_j\left[F_k, P_0\right]\right) \\
&= \mathrm{Tr}_{2M}\left(Z_j\left[\begin{pmatrix} 0 & f_k \\ -f_k^* & 0 \end{pmatrix}\begin{pmatrix} 0 & 0 \\ 0 & \mathbb{I} \end{pmatrix} - \begin{pmatrix} 0 & 0 \\ 0 & \mathbb{I} \end{pmatrix}\begin{pmatrix} 0 & f_k \\ -f_k^* & 0 \end{pmatrix}\right]\right) \\
&= \mathrm{Tr}_{2M}\left[\begin{pmatrix} 0 & z_j \\ -z_j^* & 0 \end{pmatrix}\left(\begin{pmatrix} 0 & f_k \\ 0 & 0 \end{pmatrix} - \begin{pmatrix} 0 & 0 \\ -f_k^* & 0 \end{pmatrix}\right)\right] \\
&= \mathrm{Tr}_{2M}\left[\begin{pmatrix} 0 & z_j \\ -z_j^* & 0 \end{pmatrix}\begin{pmatrix} 0 & f_k \\ f_k^* & 0 \end{pmatrix}\right] \\
&= \mathrm{Tr}_{2M}\begin{pmatrix} z_jf_k^* & 0 \\ 0 & -z_j^*f_k \end{pmatrix} \\
&= \mathrm{Tr}_M\left(z_jf_k^* - z_j^*f_k\right).
\end{aligned} \tag{2.81}$$

2.7.3 Cranking

The cranking approximation is used throughout this work as it allows for the treatment of the full quadrupole motion of the nucleus, classically about one of the intrinsic axes of the nucleus. It is key to highlight the deficiency of this approach - mainly the wavefunctions are not eigenstates of the angular momentum operator and hence the angular momentum has to be obtained from the expectation value of its projection onto the given rotation

axis. The mathematics associated with this concept were first introduced by Inglis [33] and is summarised in a variety of other texts too [28].
In the cranking approximation,

$$z_{k,\mu\nu} = i\hbar\dot{q}_k \frac{f_{k,\mu\nu}}{E_\mu + E_\nu}, \tag{2.82}$$

where E_μ and E_ν are quasi-particle energies and so

$$\begin{aligned} \mathrm{Tr}_M \left(z_j f_k^* - z_j^* f_k\right) &= \sum_{\mu\nu} \left(z_{j,\mu\nu} f^*_{k,\nu\mu} - z^*_{j,\mu\nu} f_{k,\nu\mu}\right) \\ &= i\hbar\dot{q}_j \sum_{\mu\nu} \frac{f_{j,\mu\nu} f^*_{k,\nu\mu} + f^*_{j,\mu\nu} f_{k,\nu\mu}}{E_\mu + E_\nu}. \end{aligned} \tag{2.83}$$

Note that the indices between z and f are reversed due to the definition of matrix multiplication. The mass parameter is therefore given by

$$\begin{aligned} B_{kj} &= \frac{i\hbar}{2\dot{q}_j} i\hbar\dot{q}_j \sum_{\mu\nu} \frac{f_{j,\mu\nu} f^*_{k,\nu\mu} + f^*_{j,\mu\nu} f_{k,\nu\mu}}{E_\mu + E_\nu} \\ \Rightarrow B_{kj} &= \frac{\hbar^2}{2} \sum_{\mu\nu} \frac{f_{j,\mu\nu} f^*_{k,\mu\nu} + f^*_{j,\mu\nu} f_{k,\mu\nu}}{E_\mu + E_\nu}. \end{aligned} \tag{2.84}$$

Notice in the final step that the factor of $i^2 = -1$ has been used to reverse the indices ($\nu\mu \to \mu\nu$) in both of the terms in the numerator, specifically the f_k matrix elements as they are antisymmetric.

2.7.4 Relation between the Derivatives of R_0 and H_0

This subsection is included for completeness in our new notation. We start by differentiating the HFB equation $[R_0, H_0] \approx 0$ given that we cannot solve the exact ground state of the system using NDFT. To be clear, the computational HFB approach is a numerical approach not an analytical one. Whilst in principle it should converge to the correct value there is always some discrepancy. Hence the commutation relation is never numerically equal to zero. Hence,

$$\begin{aligned} \frac{\partial}{\partial q}\left[R_0, H_0\right] &= \frac{\partial}{\partial q}\left(R_0 H_0 - H_0 R_0\right) \\ &= \frac{\partial R_0}{\partial q} H_0 + R_0 \frac{\partial H_0}{\partial q} - \frac{\partial H_0}{\partial q} R_0 - H_0 \frac{\partial R_0}{\partial q} \\ &= \left[\frac{\partial R_0}{\partial q}, H_0\right] + \left[R_0, \frac{\partial H_0}{\partial q}\right] \\ &= 0. \end{aligned}$$

Therefore,

$$\begin{aligned} \chi^\dagger_\mu \left[\frac{\partial R_0}{\partial q}, H_0\right] \phi_\nu &= -\chi^\dagger_\mu \left[R_0, \frac{\partial H_0}{\partial q}\right] \phi_\nu \\ \Rightarrow -E_\nu \chi^\dagger_\mu \frac{\partial R_0}{\partial q}\phi_\nu - E_\mu \chi^\dagger_\mu \frac{\partial R_0}{\partial q}\phi_\nu &= \chi^\dagger_\mu \frac{\partial H_0}{dq}\phi_\nu \\ \Rightarrow \chi^\dagger_\mu \frac{\partial R_0}{\partial q}\phi_\nu &= -\frac{1}{E_\mu + E_\nu} \chi^\dagger_\mu \frac{\partial H_0}{\partial q}\phi_\nu, \end{aligned} \tag{2.85}$$

where the left-hand side (LHS) is just the $f_{k,\mu\nu}$ element of the f_k matrix.

2.7.5 Constrained HFB

By definition, we wish to minimize the energy functional

$$\langle\Phi|\hat{H}|\Phi\rangle. \tag{2.86}$$

For the microscopic calculations in the $\beta\gamma$-deformation plane we require further constraints on the quadrupole moments (Q_{20} and Q_{22}) which can be obtained from the corresponding β and γ deformation parameters. These constraints manifest themselves in a constrained HFB calculation as follows

$$q_j = \langle\Phi|Q_j|\Phi\rangle. \tag{2.87}$$

This leads to the constraint $-\lambda Q_j$ in a one body Hamiltonian H_0 as follows

$$H_0 = \begin{pmatrix} h_0 - \lambda_j Q_j & \Delta \\ -\Delta^* & -h_0^* + \lambda_j Q_j^* \end{pmatrix}, \tag{2.88}$$

where λ_j are Lagrange parameters, so

$$\frac{\partial H_0}{\partial \lambda_j} \equiv \partial_{\lambda_j} H_0 = -\begin{pmatrix} Q_j & 0 \\ 0 & -Q_j^* \end{pmatrix}. \tag{2.89}$$

So we can now express our components of f as

$$\begin{aligned}
\left(f_{\lambda_j}\right)_{\mu\nu} &= \frac{1}{E_\mu + E_\nu}\chi_\mu^\dagger \begin{pmatrix} Q_j & 0 \\ 0 & -Q_j^* \end{pmatrix} \phi_\nu \\
&= \frac{1}{E_\mu + E_\nu} \begin{pmatrix} U \\ V \end{pmatrix}_\mu^\dagger \begin{pmatrix} Q_j & 0 \\ 0 & -Q_j^* \end{pmatrix} \begin{pmatrix} V^* \\ U^* \end{pmatrix}_\nu \\
&= \frac{1}{E_\mu + E_\nu} \begin{pmatrix} U^\dagger & V^\dagger \end{pmatrix}_\mu \begin{pmatrix} Q_j & 0 \\ 0 & -Q_j^* \end{pmatrix} \begin{pmatrix} V^* \\ U^* \end{pmatrix}_\nu \\
&= \frac{1}{E_\mu + E_\nu} \begin{pmatrix} U^\dagger & V^\dagger \end{pmatrix}_\mu \begin{pmatrix} Q_j V^* \\ -Q_j^* U^* \end{pmatrix}_\nu \\
&= \frac{1}{E_\mu + E_\nu} \left(U^\dagger Q_j V^* - V^\dagger Q_j^* U^*\right)_{\mu\nu} \\
&= \frac{1}{E_\mu + E_\nu} \left(U^\dagger Q_j V^* - \left(U^\dagger Q_j^\dagger V^*\right)^T\right)_{\mu\nu}.
\end{aligned} \tag{2.90}$$

2.7.6 Derivatives $\partial q_k/\partial\lambda_j$

The average value of the collective coordinates q_k can be expressed as

$$q_k = \langle\Phi|Q_k|\Phi\rangle = \mathrm{Tr}\,(Q_k R_0), \tag{2.91}$$

where Q_k has the following form in the doubled space

$$Q_k = \begin{pmatrix} Q_k & 0 \\ 0 & 0 \end{pmatrix} \tag{2.92}$$

and next we use here a constant basis yielding

$$\frac{\partial q_k}{\partial \lambda_j} = \mathrm{Tr} Q_k \frac{\partial R_0}{\partial \lambda_j}. \tag{2.93}$$

We evaluate the trace in the quasi-particle basis as follows

$$\begin{aligned}
\mathrm{Tr} Q_k \frac{\partial R_0}{\partial \lambda_j} &= \mathrm{Tr}_{2M} \mathcal{B} Q_k \mathcal{B}^\dagger \mathcal{B} \frac{\partial R_0}{\partial \lambda_j} \mathcal{B}^\dagger \\
&= \mathrm{Tr}_{2M} \mathcal{B} Q_k \mathcal{B}^\dagger F \\
&= \mathrm{Tr}_{2M} \begin{pmatrix} U^\dagger & V^\dagger \\ V^T & U^T \end{pmatrix} \begin{pmatrix} Q_k & 0 \\ 0 & 0 \end{pmatrix} \begin{pmatrix} U & V^* \\ V & U^* \end{pmatrix} \begin{pmatrix} 0 & f_j \\ -f_j^* & 0 \end{pmatrix} \\
&= \mathrm{Tr}_{2M} \begin{pmatrix} U^\dagger & V^\dagger \\ V^T & U^T \end{pmatrix} \begin{pmatrix} Q_k & 0 \\ 0 & 0 \end{pmatrix} \begin{pmatrix} -V^* f_j^* & U f_j \\ -U^* f_j^* & V f_j \end{pmatrix} \\
&= \mathrm{Tr}_{2M} \begin{pmatrix} U^\dagger & V^\dagger \\ V^T & U^T \end{pmatrix} \begin{pmatrix} Q_k & 0 \\ 0 & 0 \end{pmatrix} \begin{pmatrix} -Q_k V^* f_j^* & Q_k U f_j \\ 0 & 0 \end{pmatrix} \\
&= \mathrm{Tr}_{2M} \begin{pmatrix} -U^\dagger Q_k V^* f_j^* & U^\dagger Q_k U f_j \\ -V^T Q_k V^* f_j^* & V^T Q_k U f_j \end{pmatrix} \\
&= \mathrm{Tr}_M \left(V^T Q_k U f_j - U^\dagger Q_k V^* f_j^* \right) \\
&= \mathrm{Tr}_M \left(g_k^\dagger f_j - g_k f_j^* \right), \qquad (2.94)
\end{aligned}$$

where we have defined

$$g_k \equiv U^\dagger Q_k V^* \qquad (2.95)$$

$$g_k^\dagger \equiv V^T Q_k U. \qquad (2.96)$$

Given that $\frac{\partial q_k}{\partial \lambda_j}$ is real we can write

$$\begin{aligned}
\frac{\partial q_k}{\partial \lambda_j} &= \frac{1}{2} \mathrm{Tr}_M \left(g_k^\dagger f_j - g_k f_j^* + g_k^T f_j^* - g_k^* f_j \right) \\
&= \frac{1}{2} \mathrm{Tr}_M \left(\left(g_k^T - g_k \right)^* f_j + \left(g_k^T - g_k \right) f_j^* \right). \qquad (2.97)
\end{aligned}$$

If we introduce a term w_k (where the sign of w compared to the above equation has been reversed), defined as

$$w_k \equiv g_k - g_k^T, \qquad (2.98)$$

we obtain the following

$$(f_j)_{\mu\nu} = \frac{1}{E_\mu + E_\nu} w_{j,\mu\nu}, \qquad (2.99)$$

resulting in

$$\begin{aligned}
\frac{\partial q_k}{\partial \lambda_j} &= -\frac{1}{2} \sum_{\mu\nu} \frac{(w_k^*)_{\mu\nu} (w_j)_{\nu\mu} + (w_k)_{\mu\nu} \left(w_j^* \right)_{\nu\mu}}{E_\mu + E_\nu} \\
&= -\mathrm{Re} \left(\sum_{\mu\nu} \frac{(w_k^*)_{\mu\nu} (w_j)_{\nu\mu}}{E_\mu + E_\nu} \right). \qquad (2.100)
\end{aligned}$$

Now we notice that w_j is antisymmetric and hence we can simplify the above expression to

$$\frac{\partial q_k}{\partial \lambda_j} = \mathrm{Re} \left(\sum_{\mu\nu} \frac{(w_k^*)_{\mu\nu} (w_j)_{\mu\nu}}{E_\mu + E_\nu} \right), \qquad (2.101)$$

which in the case of one variable may be simplified further to

$$\frac{\partial q_j}{\partial \lambda_j} = \left(\sum_{\mu\nu} \frac{\left| \left(w_j^* \right)_{\mu\nu} \right|^2}{E_\mu + E_\nu} \right). \tag{2.102}$$

Now it is possible to pull all of these expressions together and calculate the vibrational mass parameters and subsequently the rotational mass parameters from the moments of inertia in the next two subsections. These have been obtained via the cranking approximations in a constrained HFB calculation which yields the microscopic mass parameters from an underlying theory as opposed to phenomenology.

2.7.7 Vibrational Mass Parameters

The mass parameters $B_{\lambda_j \lambda_k}$ are calculated according to (2.84) and (2.99), note the factor of 2 in equation (2.84) is cancelled out by taking the real part of the full numerator i.e. two terms simplify to one with a factor of 2 as follows

$$\begin{aligned} B_{\lambda_j \lambda_k} &= \hbar^2 \mathrm{Re} \left(\sum_{\mu\nu} \frac{f_{j,\mu\nu} f^*_{k,\mu\nu}}{E_\mu + E_\nu} \right) \\ &= \hbar^2 \mathrm{Re} \left(\sum_{\mu\nu} \frac{w_{j,\mu\nu} w^*_{k,\mu\nu}}{\left(E_\mu + E_\nu\right)^3} \right). \end{aligned} \tag{2.103}$$

Now in order to get the mass parameters $B_{q_j q_k}$ we use the derivatives $\partial_{\lambda_j} q_k$, expression (2.101), but first we must explicitly add proton (p) and neutron (n) terms:

$$\begin{aligned} \left(B_{\lambda_j \lambda_k}\right)_{\mathrm{Total}} &= \left(B_{\lambda_j \lambda_k}\right)_{\mathrm{p}} + \left(B_{\lambda_j \lambda_k}\right)_{\mathrm{n}} \\ \partial_{\lambda_j} \left(q_k\right)_{\mathrm{Total}} &= \partial_{\lambda_j} \left(q_k\right)_{\mathrm{p}} + \partial_{\lambda_j} \left(q_k\right)_{\mathrm{n}} \end{aligned} \tag{2.104}$$

and finally we obtain

$$\left(B_{q_j, q_k}\right)_{\mathrm{Total}} = \left[\partial_{\lambda_j} \left(q_k\right)_{\mathrm{Total}}\right]^{-1} \left(B_{\lambda_j \lambda_k}\right)_{\mathrm{Total}} \left[\partial_{\lambda_j} \left(q_k\right)_{\mathrm{Total}}\right]^{-1}. \tag{2.105}$$

2.7.8 Moments of Inertia

This section concerns the rotational aspects of the work - in particular obtaining moments of inertia which are used to obtain the rotational mass parameters. We assume that we have a one parameter group of unitary operators $\mathcal{G}(\beta)$ acting in the Fock space and Φ_c is a given (constant) quasi-particle vacuum with a corresponding generalized density matrix R_c. The group $\mathcal{G}(\beta)\Phi_c$ is a set of quasi-particle vacuums with $R(\beta)$ density matrices given by

$$\begin{aligned} & R(\beta) = G(\beta) R_c G^\dagger(\beta) \\ & \Rightarrow R_c = G^\dagger(\beta) R(\beta) G(\beta) \qquad \text{since } G(\beta) G^\dagger(\beta) = \mathbb{I}, \end{aligned} \tag{2.106}$$

where $G(\beta)$ represents a rotation operator. We will explore the connection between the group $\mathcal{G}$ and the matrix G in the following discussion.
We need to obtain an expression for $F_\beta = \mathcal{B} \partial_\beta R(\beta) \mathcal{B}^\dagger$. So,

$$\begin{aligned} \partial_\beta R(\beta) &= \partial_\beta G R_c G^\dagger + G R_c \partial_\beta G^\dagger \\ &= \partial_\beta G G^\dagger R(\beta) G G^\dagger + G G^\dagger R(\beta) G \partial_\beta G^\dagger. \end{aligned} \tag{2.107}$$

Given that $G(\beta)$ is unitary and by employing the product rule we can see that

$$\begin{aligned} \partial_\beta (\mathbb{I}) &= 0 \\ \Rightarrow \partial_\beta \left(GG^\dagger\right) &= 0 \\ \Rightarrow \partial_\beta (G) G^\dagger + G\partial_\beta \left(G^\dagger\right) &= 0 \\ \Rightarrow G\partial_\beta \left(G^\dagger\right) &= -\partial_\beta (G) G^\dagger. \end{aligned} \tag{2.108}$$

Therefore,

$$\begin{aligned} \partial_\beta R(\beta) &= \partial_\beta G G^\dagger R(\beta) \underbrace{GG^\dagger}_{\mathbb{I}} + \underbrace{GG^\dagger}_{\mathbb{I}} R(\beta) G\partial_\beta G^\dagger \\ &= \boldsymbol{\chi} R(\beta) - R(\beta)\boldsymbol{\chi} \quad \text{where } \boldsymbol{\chi} = \partial_\beta (G) G^\dagger \\ \Rightarrow \partial_\beta R(\beta) &= [\boldsymbol{\chi}, R(\beta)]. \end{aligned} \tag{2.109}$$

Given that

$$F_\beta = \mathcal{B}\partial_\beta R(\beta)\mathcal{B}^\dagger = \left[\mathcal{B}\boldsymbol{\chi}\mathcal{B}^\dagger, P_0\right], \tag{2.110}$$

given $\mathcal{B}$ is unitary.
The matrix $G(\beta)$ has the form

$$G(\beta) = \begin{pmatrix} g & 0 \\ 0 & g^* \end{pmatrix} \qquad \text{where } g = e^{-i\beta s}, \tag{2.111}$$

where s is a hermitian matrix representing a generator of rotation (in this case J_z). So,

$$\partial_\beta G = \begin{pmatrix} -ise^{-i\beta s} & 0 \\ 0 & is^* \left(e^{-i\beta s}\right)^* \end{pmatrix} \tag{2.112}$$

and therefore

$$\boldsymbol{\chi} = -i \begin{pmatrix} s & 0 \\ 0 & -s^* \end{pmatrix}. \tag{2.113}$$

Hence,

$$\begin{aligned} F_\beta &= -i \left[\begin{pmatrix} U^\dagger & V^\dagger \\ V^T & U^T \end{pmatrix} \begin{pmatrix} s & 0 \\ 0 & -s^* \end{pmatrix} \begin{pmatrix} U & V^* \\ V & U^* \end{pmatrix}, \begin{pmatrix} 0 & 0 \\ 0 & \mathbb{I} \end{pmatrix} \right] \\ &= -i \left[\begin{pmatrix} U^\dagger & V^\dagger \\ V^T & U^T \end{pmatrix} \begin{pmatrix} sU & sV^* \\ -s^*V & -s^*U^* \end{pmatrix}, \begin{pmatrix} 0 & 0 \\ 0 & \mathbb{I} \end{pmatrix} \right] \\ &= -i \left[\begin{pmatrix} U^\dagger sU - V^\dagger s^* V & U^\dagger sV^* - V^\dagger s^* U^* \\ V^T sU - U^T s^* V & V^T sV^* - U^T s^* U^* \end{pmatrix}, \begin{pmatrix} 0 & 0 \\ 0 & \mathbb{I} \end{pmatrix} \right] \\ &= -i \left[\begin{pmatrix} 0 & U^\dagger sV^* - V^\dagger s^* U^* \\ 0 & V^T sV^* - U^T s^* U^* \end{pmatrix} - \begin{pmatrix} 0 & 0 \\ V^T sU - U^T s^* V & V^T sV^* - U^T s^* U^* \end{pmatrix} \right] \\ &= -i \begin{pmatrix} 0 & U^\dagger sV^* - V^\dagger s^* U^* \\ -\left(V^T sU - U^T s^* V\right) & 0 \end{pmatrix} \\ &= \begin{pmatrix} 0 & -i\left(U^\dagger sV^* - V^\dagger s^* U^*\right) \\ i\left(V^T sU - U^T s^* V\right) & 0 \end{pmatrix} \\ &= \begin{pmatrix} 0 & -i\left(U^\dagger sV^* - V^\dagger s^* U^*\right) \\ -\left(i\left(U^T s^* V - V^T sU\right)\right) & 0 \end{pmatrix} \\ &= \begin{pmatrix} 0 & -i\left(U^\dagger sV^* - V^\dagger s^* U^*\right) \\ -\left(-i\left(U^\dagger sV^* - V^\dagger s^* U^*\right)\right)^* & 0 \end{pmatrix}. \end{aligned} \tag{2.114}$$

Finally, we obtain an expression representing fixed rotations around various axes given by

$$f_{\beta_k} = -i\left(U^\dagger s_k V^* - \left(U^\dagger s_k V^*\right)^T\right). \tag{2.115}$$

Here s_k is a matrix of the total angular momentum operator $\hat{J}_k$ and hence, the moment of inertia in the cranking approximation is given by

$$I_k = \sum_{\mu\nu} \frac{|f_{\beta_k}|^2}{E_\mu + E_\nu}. \tag{2.116}$$

Generally speaking the case of rotation around one axis is simple. In this case the collective variable is the angle of rotation and the mass parameter, I_k, is a moment of inertia. Note that the case of three Euler angles must be treated more carefully and more rigorously where the three Euler angles are used to orientate the axis of the nucleus allowing a connection between the intrinsic and laboratory frames to be made. These angles ultimately allow the angular momentum to be included in the Bohr Hamiltonian (derived in section 2.8) and a full discussion of this is made in ([34] and [35]).

2.8 Derivation of the Collective Model

Now it is possible to derive and discuss the Bohr Hamiltonian (BH) as described by the collective model and subsequently generalise it to the more common form of the *Generalised Bohr Hamiltonian* used in this work. The mathematics is presented in detail in several appendices to highlight any and all definitions used within this work which will ultimately be the basis of the computational procedure outlined in chapter 3. Finally, a discussion on the known advantages and disadvantages of this methodology is presented.
The collective model of Bohr and Mottelson [6] [34] [35] connected the phenomenon of collective motion of nucleons within a nucleus with the non-interacting single particle motions. They subsequently constructed a phenomenological model - the collective model - to accurately describe such phenomenon in nuclei.
These collective motions specifically manifest themselves in two ways - rotational motion of the nucleons and vibrational motion of the nucleus. These phenomena play a key role in the area of nuclear deformation and shape coexistence for example. To this end, it is key to be clear on several key physical and mathematical concepts discussed in the remainder of this chapter. In the remainder of the present section we explore, in detail, the construction of the BH.

2.8.1 Collective Coordinates

Multipole moments are a useful choice for our collective coordinates for two key reasons, firstly because they are directly related to observable moments of the nuclear charge distribution and secondly because they have a microscopic description in terms of many-nucleon coordinates of a microscopic theory.
We can define a radial coordinate β in $\mathbb{R}^5$ analogous to $r^2 = x^2 + y^2 + z^2$ in $\mathbb{R}^3$ by

$$\beta^2 \equiv \sum_m |q_m|^2, \tag{2.117}$$

where q_m are the quadrupole moments as discussed in section 2.5 and we can describe the laboratory frame coordinates with respect to the intrinsic frame coordinates by making use of Euler angles Ω

$$Q_{ij} \to \left(\Omega Q \Omega^{-1}\right)_{ij} = \sum_{kl} \Omega_{ik} Q_{kl} \Omega_{jl}, \quad \Omega \in SO(3). \tag{2.118}$$

The following is a review of the current derivation (more specifically construction) of the collective Hamiltonian - the BH.
For clarity it is useful to start with a review of the foundational mathematics required for the derivation - the metric tensor and the Laplace-Beltrami operator. Then we will derive both the volume element and the Laplacian associated with the 5-dimensional Hamiltonian. This 5-dimensional Hamiltonian is constructed using the previously discussed nuclear deformation parameters (β, γ) and the rotational frame euler angles θ_k where $k = 1, 2, 3$. The first trivial mathematical criteria to outline with regards to the construction of this 5-dimensional Hamiltonian is that we assume a Euclidean geometry associated with the real space $\mathbb{R}^5$. Appendix B summarises the metric tensor for a flat Euclidean space where the volume element for that n-dimensional space is given by

$$dV = d^n x = \prod_i dx_i. \tag{2.119}$$

In this case we are dealing with a 5-dimensional Euclidean space and wish to express it in arbitrary curvilinear coordinates as follows

$$dV = J d^5\xi \equiv J \prod_\sigma d\xi^\sigma, \tag{2.120}$$

where J is the Jacobian associated with the transformation $\{dx_i\} \rightarrow \{d\xi^\sigma\}$ from the standard Cartesian coordinates to arbitrary curvilinear coordinates and is the determinant of the matrix $\{\partial x_i / \partial \xi^\sigma\}$. It subsequently follows that

$$J = \sqrt{\det(g)}. \tag{2.121}$$

The Laplace-Beltrami operator, expressed in arbitrary curvilinear coordinates, is derived in Appendix C making use of the metric tensor definitions as discussed in Appendix B and is given by

$$\Rightarrow \nabla^2 = \sum_{\kappa\lambda} \frac{1}{J} \frac{\partial}{\partial \xi^\kappa} J \overline{g}^{\kappa\lambda} \frac{\partial}{\partial \xi^\lambda} \quad \text{(Laplace-Beltrami Operator)}. \tag{2.122}$$

The full derivation of both the metric tensor and corresponding Jacobian used in the construction of the BH are presented in Appendix D. Given that the quadrupole moments q_m are given by

$$q_m = \beta \left[\cos(\gamma) \mathscr{D}^2_{0m}(\Omega) + \sqrt{\frac{1}{2}} \sin(\gamma) \left(\mathscr{D}^2_{2m}(\Omega) + \mathscr{D}^2_{-2m}(\Omega) \right) \right], \tag{2.123}$$

the metric tensor is given by

$$g = \begin{pmatrix} 1 & 0 & 0 & 0 & 0 \\ 0 & \beta^2 & 0 & 0 & 0 \\ 0 & 0 & 4\beta^2 \sin^2(\gamma - 2\pi/3) & 0 & 0 \\ 0 & 0 & 0 & 4\beta^2 \sin^2(\gamma - 4\pi/3) & 0 \\ 0 & 0 & 0 & 0 & 4\beta^2 \sin^2(\gamma) \end{pmatrix} \tag{2.124}$$

and since the matrix is diagonal the Jacobian J is given by the product of the diagonal terms yielding

$$J^2 = 64\beta^8 \sin^2(\gamma) \sin^2(\gamma - 2\pi/3) \sin^2(\gamma - 4\pi/3), \tag{2.125}$$

which can be simplified with trigonometric identities to

$$\begin{aligned} J^2 &= 4\beta^8 \sin^2(3\gamma) \\ \Rightarrow J &= \pm 2\beta^4 \sin(3\gamma). \end{aligned} \tag{2.126}$$

Noting that for a physical coordinate system we will use the real positive i.e. $J = 2\beta^4 \sin(3\gamma)$. Thus, both the volume element and the Laplacian operator are derived as follows

$$\begin{aligned} dV &= J d^5\xi \\ \Rightarrow dV &= 2\beta^4 \sin(3\gamma)\, d\beta d\gamma d\Omega, \end{aligned} \tag{2.127}$$

where $d\Omega$ are the "volume elements" associated with the Euler angles describing the coordinate frame rotation. It is useful to note that most sources omit the factor of 2 from the volume element and write it simply as $dV = \beta^4 \sin(3\gamma)\, d\beta d\gamma d\Omega$, either way the same Laplacian is obtained.
The Laplacian is given by

$$\begin{aligned} \nabla^2 &= \sum_{\kappa\lambda} \frac{1}{J} \frac{\partial}{\partial \xi^\kappa} J \overline{g}^{\kappa\lambda} \frac{\partial}{\partial \xi^\lambda} \\ &= \frac{1}{2\beta^4 \sin(3\gamma)} \frac{\partial}{\partial \beta} \left(2\beta^4 \sin(3\gamma)\right)(1) \frac{\partial}{\partial \beta} + \frac{1}{2\beta^4 \sin(3\gamma)} \frac{\partial}{\partial \gamma} \left(2\beta^4 \sin(3\gamma)\right) \left(\frac{1}{\beta^2}\right) \frac{\partial}{\partial \gamma} \\ &+ \sum_{k=1}^{3} \frac{1}{2\beta^4 \sin(3\gamma)} \frac{\partial}{\partial \theta^k} \left(2\beta^4 \sin(3\gamma)\right) \left(\frac{1}{4\beta^2 \sin^2(\gamma - 2\pi k/3)}\right) \frac{\partial}{\partial \theta^k} \\ &= \frac{1}{2\beta^4 \sin(3\gamma)} \frac{\partial}{\partial \beta} \left(2\beta^4 \sin(3\gamma)\right)(1) \frac{\partial}{\partial \beta} + \frac{1}{2\beta^4 \sin(3\gamma)} \frac{\partial}{\partial \gamma} \left(2\beta^4 \sin(3\gamma)\right) \left(\frac{1}{\beta^2}\right) \frac{\partial}{\partial \gamma} \\ &+ \frac{1}{\beta^2} \sum_{k=1}^{3} \frac{\left(i\overline{L}_k\right)^2}{4\sin^2(\gamma - 2\pi k/3)} \\ &= \frac{1}{\beta^4} \frac{\partial}{\partial \beta} \beta^4 \frac{\partial}{\partial \beta} + \frac{1}{\beta^2 \sin(3\gamma)} \frac{\partial}{\partial \gamma} \sin(3\gamma) \frac{\partial}{\partial \gamma} - \frac{1}{\beta^2} \sum_{k=1}^{3} \frac{\overline{L}_k^2}{4\sin^2(\gamma - 2\pi k/3)} \\ &= \frac{1}{\beta^4} \frac{\partial}{\partial \beta} \beta^4 \frac{\partial}{\partial \beta} - \frac{\Lambda^2}{\beta^2}, \end{aligned} \tag{2.128}$$

where

$$\Lambda^2 = -\frac{1}{\sin(3\gamma)} \frac{\partial}{\partial \gamma} \sin(3\gamma) \frac{\partial}{\partial \gamma} + \sum_{k=1}^{3} \frac{\overline{L}_k^2}{4\sin^2(\gamma - 2\pi k/3)}. \tag{2.129}$$

Hence, the Bohr Hamiltonian is given by

$$\hat{H} = -\frac{\hbar^2}{2B} \left[\frac{1}{\beta^4} \frac{\partial}{\partial \beta} \beta^4 \frac{\partial}{\partial \beta} + \frac{1}{\beta^2 \sin(3\gamma)} \frac{\partial}{\partial \gamma} \sin(3\gamma) \frac{\partial}{\partial \gamma} - \frac{1}{\beta^2} \sum_{k=1}^{3} \frac{\overline{L}_k^2}{4\sin^2(\gamma - 2\pi k/3)} \right] + \hat{V}(\beta, \gamma). \tag{2.130}$$

Note from equation 2.130 that B is the mass parameter operator/tensor which will be made explicit in the following subsection. From the formalisim as shown above it would be possible to choose mass parameters phenomenologically. However, the endeavour of this work is to ensure they are obtained microscopically through constrained HFB calculations. Since the inception of this version of the BH multiple advancements have been made to generalise the form to include the specific vibrational and rotational mass parameters explicitly in the Hamiltonian and this gives rise to the Generalised Bohr Hamiltonian summarised in the following subsection.

2.8.2 The Generalised Bohr Hamiltonian

Here we will discuss the generalisation of the earlier derivation leading to what is commonly referred to as the Generalised Bohr Hamiltonian (GBH). The kinetic energy tensor takes a block diagonal for

$$B = \begin{pmatrix} B_{\text{vib}} & 0 \\ 0 & B_{\text{rot}} \end{pmatrix}, \tag{2.131}$$

where the vibrational part of the tensor is given by

$$B_{\text{vib}} = \begin{pmatrix} B_{\beta\beta} & \beta B_{\beta\gamma} \\ \beta B_{\beta\gamma} & \beta^2 B_{\gamma\gamma} \end{pmatrix}. \tag{2.132}$$

The so-called GBH, where quadrupole variables α_μ are proportional to the quadrupole mass tensor is given by

$$\begin{aligned} \hat{T}_{\text{vib}} = &-\frac{1}{2\sqrt{wr}} \left\{ \frac{1}{\beta^4} \left[\partial_\beta \left(\beta^4 \sqrt{\frac{r}{w}} B_{\gamma\gamma} \right) \partial_\beta - \partial_\beta \left(\beta^3 \sqrt{\frac{r}{w}} B_{\beta\gamma} \right) \partial_\gamma \right] \right. \\ &\left. + \frac{1}{\beta \sin(3\gamma)} \left[-\partial_\gamma \left(\sqrt{\frac{r}{w}} \sin(3\gamma) B_{\beta\gamma} \right) \partial_\beta + \frac{1}{\beta} \partial_\gamma \left(\sqrt{\frac{r}{w}} \sin(3\gamma) B_{\beta\beta} \right) \partial_\gamma \right] \right\} \end{aligned} \tag{2.133}$$

$$\hat{T}_{\text{rot}} = \frac{1}{2} \sum_{k=1}^{3} I_k^2(\Omega) / J_k; \tag{2.134}$$

where $I_k(\omega)$'s are components of angular momentum in the intrinsic frame and the simplifying expressions above are given by

$$J_k = 4B_k(\beta,\gamma)\beta^2 \sin^2(\gamma - 2\pi k/3); \quad w = B_{\beta\beta}B_{\gamma\gamma} - B_{\beta\gamma}^2; \quad r = B_x B_y B_z. \tag{2.135}$$

The 6 mass parameters presented above are the quantities that are obtained microscopically from the constrained HFB calculations. These mass parameters are connected to describing the explicit vibration ($B_{\beta\beta}, B_{\beta\gamma}, B_{\gamma\gamma}$) and rotation ($B_x, B_y, B_z$) of the nucleus and connects the intrinsic frame with the laboratory frame. This creates a systematic way of carrying out BH calculations across all nuclei instead of fine-tuning or phenomenologically choosing the mass parameters by hand or intuition. Appendix A has further mathematics associated with the structure of the mass parameters, in particular the conventions used in the BH code which will be discussed in the next chapter.
Here is a brief discussion on a list of limitations and advantages of the Bohr Hamiltonian approach. A more comprehensive discussion is presented in [36] with comparison to other collective models.

2.8.3 Limitations of the Bohr Hamiltonian

The main limitations of the Bohr Hamiltonian are listed below.

1. The BH is only applicable to even-even systems. The BH is limited to even-even nuclei and does not inherently describe odd or odd-odd nuclei. It should be noted that this may be possible to overcome for some nuclei if it is reasonable to approximate a given nucleus as a combination of an even-even core (described by the BH) and one (or two) quasi-particles. To date, it remains an open question if such an approximation is reasonable - whether this approximation applies to all nuclei is an open question - but initial work in this area is presented in [37].

2. The BH is restricted to quadrupole deformation. Whilst theoretical research has lead to the development of possible mathematical foundations which could include higher order multipoles within the BH approach these are not currently practical to implement and hence, we are restricted to describing quadrupole deformed systems. This is a limitation albeit not a major one as the most common/pronounced deformation across the nuclear chart, especially in medium-to-heavy mass nuclei, is quadrupole and hence we have a large number of nuclei for which BH should be applicable to. Some more recent works [38] exploring higher multipole moments within the BH framework indicate that they may have a significant affect on nuclei which exhibit such deformations and from [39] some preliminary work with axial octupole deformations have been attempted in the actinides.

3. The BH appears to have a deficiency for magic and semi-magic nuclei. A known limitation of the BH which we should see manifesting within this massive survey is a inaccuracy of the observables for semi-magic nuclei. This appears to be a pairing effect regarding magic and semi-magic nuclei is considerably different. It may also be true that results will not only be off for such nuclei but also as we approach such magic and semi-magic nuclei.

4. The BH neglects explicit coupling to the collective pairing degrees of freedom [40] which will naturally affect the energy spectra and the associated structure of the states.

5. The BH also neglects the feedback from collective excitations to the Hamiltonian resulting in a non-adiabatic cranking approach in the current scheme. Ideally, a full Adiabatic Time Dependent Hartree-Fock-Bogoliubov (ATDHFB) calculation would be a better approach but to date no such work has been implemented and thus approximations, such as this one, have to be made.

2.8.4 Advantages of the Bohr Hamiltonian

The main advantages of the Bohr Hamiltonian are listed below.

1. Unlike more sophisticated methods such as that of the Generator Coordinate Method (GCM), BH itself does not have complications in numerical calculations with poles which can often stifle GCM calculations [41]. This can result in quicker computational convergence of BH calculations compared with other more computationally intensive methods. Additionally, [29] describes the advantages of BH over certain types of symmetry restoration in various models.

2. The BH intrinsically links theoretical calculations performed in the intrinsic frame of reference to measurements of experimental observables in the laboratory frame of reference. Thus, we can access direct predictions and comparisons to experiment through using this approach.

3. The code is computationally efficient and quick to run. The bottleneck associated with these calculations is converging, to the correct degree of numerical accuracy, the microscopic HFB calculations associated with each deformation point for a given nucleus. This is discussed in chapter 3.

Chapter 3

Computational Implementation

This chapter explores the computational codes performing both the constrained HFB calculations of mass parameters - HFODD249t [42] - and the Bohr Hamiltonian code of Leszek Próchniak (unpublished code). The most computational intensive part of these calculations are the vast array of constrained HFB calculations which can take up to 2 days to fully converge one deformation point in the $\beta\gamma$-plane. The advantage of the automated computational procedure is that multiple deformation points can be run in parallel and therefore the crucial limitation of these calculations is how many cores on a computing cluster you are granted access too - in my case a few 100 cores when the cluster is busy and needing to be shared. Thus, progress over the survey region is slow. Detailed are the edited versions of the codes and supporting scripts developed over this research project allowing these codes to consistently and robustly undertake the desired systematic survey of nuclei. This chapter includes sample benchmark calculations of the xenon isotopic chain with two UNEDF functionals - UNEDF0 used to test that the resultant computational procedure is consistent with previous work and UNEDF1$_{\mathrm{SO}}$ used to test that the code is adaptable to different interactions for future ongoing work. Further computational benchmark tests were made using ^{126}Xe and ^{128}Xe in order to evaluate computational time to fully converge the minimum required number of points within the Potential Energy Surface (PES) in order to balance computational runtime and accuracy of the results for both the energy spectra and associated reduced $B\left(E2\right)$ transition rates. All of the benchmark tests and subsequent BH study were carried out on the Viking computing cluster at the University of York. Details can be found at: `https://www.york.ac.uk/it-services/services/viking-computing-cluster/`

3.1 Global Computational Procedure

List of prerequisite codes pre-dating this research and minor edits made by David Muir:

1. Modified HFODD249t [42].

   This is an older version of the well known HFODD nuclear DFT code. Initial edits were made by Leszek Próchniak to allow the extraction of the moments of inertia calculated at any $\beta\gamma$ deformation point in the PES. From this the 6 mass parameters B_k (3 vibrational mass parameters in the deformation plane $B_{\beta\beta}$, $B_{\beta\gamma}$, $B_{\gamma\gamma}$ and 3 rotational mass parameters B_x, B_y, B_z) are calculated. It is key to stress that in this work these mass parameters have been calculated microscopically from DFT calculations instead of obtained through some phenomenology. Ultimately, this provides a much more robust procedure for evaluating the BH approach than phenomenological educated guesses for particular nuclei. Crucially these microscopic calculations are carried out on a deformed harmonic oscillator basis where the oscillator lengths

are adjusted in this code automatically. Additionally, as an adapted older version of HFODD code it did not already include the functionals used in the later part of the project such as UNEDF1 or UNEDF1$_{\mathrm{SO}}$ and so these were added as minor edits to the code. Additionally, during the benchmarks and testing phase outlined in this chapter it became necessary to examine all of the convergence parameters in order to improve convergence. It became clear that over a wide range of nuclei there were vast differences in the ability to converge the output to a satisfactory level and in the end these "speed-up" functions were not used and the input convergence parameters were heavily edited. Furthermore, various difficulties in converging HFODD to a satisfactory standard were encountered throughout the project and this lead to manual edits of the HFODD input to many deformation point of the majority of nuclei throughout the duration of the project, often occurring several times over. This was the ultimate bottleneck of the study as a whole but there was no way to actively foresee deformation points in any nucleus which would fail (see subsection 3.3.3 for further details). Given the current implementation of HFODD this is a severe bottleneck but could potentially be overcome by other computational approaches to solving the constrained HFB calculations such as the gradient method of diagonalisation which does not appear to encounter the same convergence difficulties as the current approach. This is something that should be under consideration for future studies of this type. However, within the current approach the convergence difficulties arise from numerical instabilities in computational parameter space which is difficult to account for and cannot be predicted ahead of time. However, for the nuclei calculated in this work which achieved convergence, all of these numerical parameters are now known and so reproducing these triaxial constrained HFB calculations would be able to be converged much faster without the need for manual re-runs.

2. Bohr Hamiltonian Code of Leszek Próchniak.

   This code provides the basis of carrying out the BH procedure and all of the associated calculations utilising the microscopic mass parameters from HFODD as outlined in the background theory chapter. From this it is possible to calculate energy spectra and their associated reduced transition probabilities as is the key aim of this work. Again, similar to HFODD whilst these codes work they do not automatically work together. It requires specific input from HFODD in a particular format and the output from this BH code is human readable but difficult to analyse in a global survey of this nature so a large amount of computational edits were required in order to carry out the proposed study.

3. GMT software package.

   The GMT software package is a plotting tool originally designed for use in the geographical sciences. The benefit of this plotting tool over others is the feasibility of coding this into the automated procedure and automatically generate plots of the potential energy surfaces and mass parameters.

Therefore, it is important to build an automatic procedure which integrates these two codes uniformly together in a global computational procedure and essentially provide clear and accessible output for each deformation point within each nucleus for each nuclear chain leading to an easily accessible global analysis of the nuclear chart. Additionally, in cases that fail there must be appropriate output to minimise the manual labour in computational re-runs of the codes. Finally, a lot of work is required to correctly extract and represent

this global data once convergence is achieved. A list of prerequisite scripts and codes created solely by David Muir are below.

1. Nuclear_Chart_Survey.f90

   Dependencies: Chemical_Elements, Nuclear_Chart_Survey_Input
   Outputs: (Master Directory) containing a list of nuclei (in this case isotopic chains) specified within the input file.

2. Beta_Gamma_Points.f90

   Creates a list of $\beta\gamma$ deformation mesh points as specified by the user and calculates the corresponding quadrupole deformation parameters Q_{20} and Q_{22} necessary for HFODD.

3. HFODD_Script.sh Based on the $\beta\gamma$ mesh density calculated in the previous code based on user input it generates and runs an HFODD calculation for each deformation point in the $\beta\gamma$ plane.

4. BH_Script.sh

   Compiles and runs the following codes:

   (a) HFODD_Convergence_Test.f90 Tests all of the deformation point HFODD calculations in the map and gathers data on the convergence of these calculations in a simplistic and accessible way for the user to identify needed re-runs. Extracts needed outputs from HFODD needed for the following code to run. Specifically, the $\beta\gamma$ deformation points, their associated constrined HFB energies (which will be used as input to the BH code and to the GMT code in order to generate the PES) and finally the moments of inertia - from which the mass parameters are explicitly calculated, again for use in the BH code.
   (b) Scaled_Energies.f90 Creates the BH input files based on the extracted data obtained in (a) for both scaled and unscaled mass parameters up to the highest fully converged β point in the map. It also creates input files for GMT in order to generate the PES as well as a list of each of the 6 mass parameters which can subsequently be plotted.

5. Analysis.sh

   Runs the BH code with the created converged input from all of the deformation point HFODD calculations for both scaled and unscaled mass parameter files. Extracts desired user defined energy spectra and $B\left(E2\right)$ reduced transition probabilities. Constructs output files for user requested states and generates GMT input with its associated potential energy surface data and runs the GMT plotting software to generate the potential energy surfaces.

6. Isotopic_Chain_Analysis.f90

   Gathers all of the outputs for each nucleus in a given isotopic chain generated from Analysis.sh and creates an output file summarising key outputs in a single document which can be published as a readable database of these calculations.

From this work and the remaining discussions of benchmarks and appropriate fixes in this chapter, a robust automated BH framework was created and implemented to obtain the global survey discussed in the following results chapter. Figure 3.1 shows a computational flowchart for the robust systematic implementation of the Bohr Hamiltonian procedure.

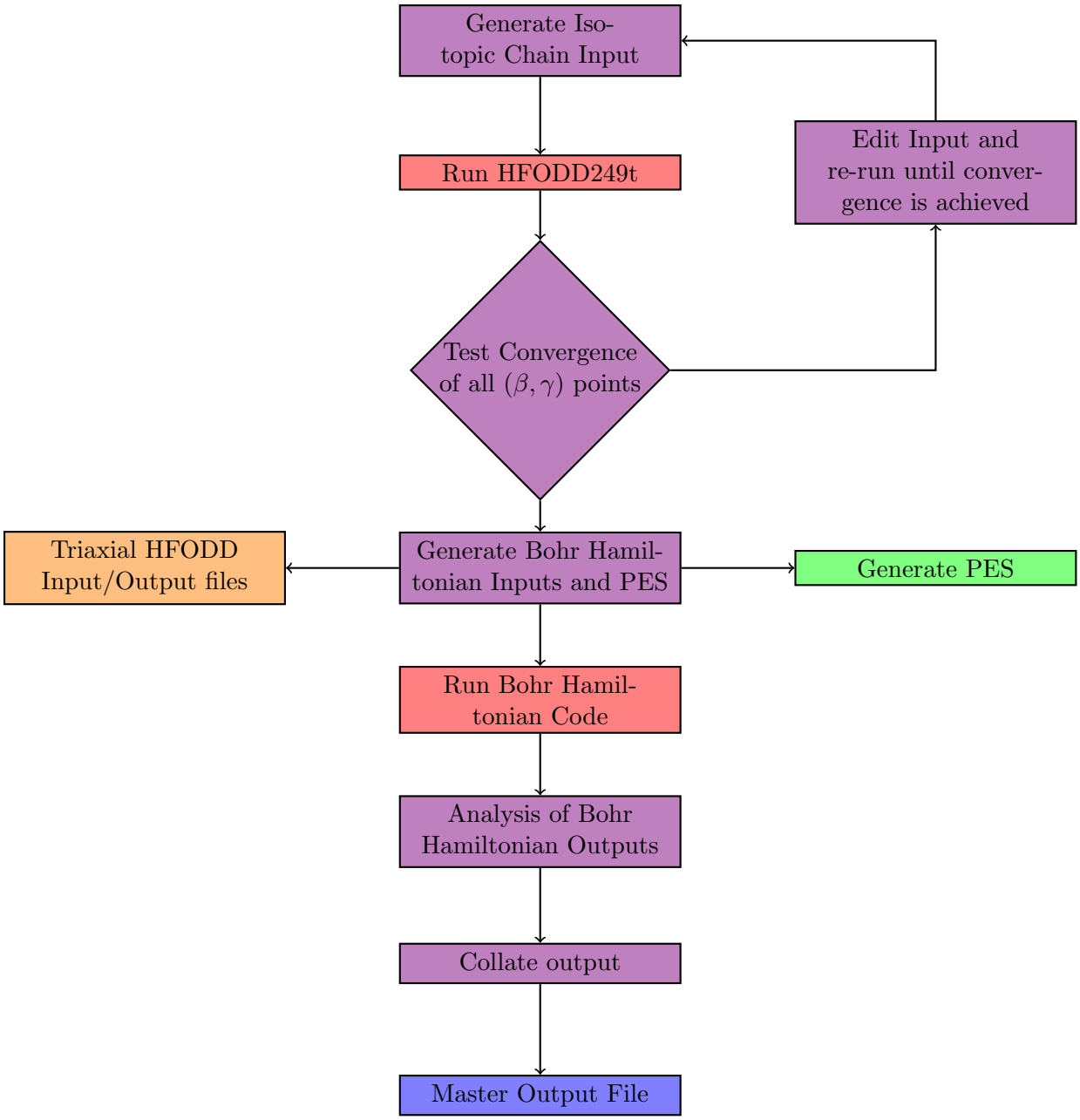

Figure 3.1: Flowchart of the global computational procedure employed in the systematic study of even-even nuclei within the Bohr Hamiltonian methodology. Steps and codes highlighted in red are pre-existing standalone codes which have been incorporated into the global implementation. Steps, codes and scripts shown in violet have been solely created and implemented by David Muir in order to construct a logical and robust implementation of the methodology which can be built on in future work. Highlighted in green are outputs obtained systematically for this study and in blue we highlight the resultant isotopic chain document created to summarize these known outputs.

3.2 Experimental Data

All experimental data was mined from the National Nuclear Data Center (NNDC) [2] (version available as of January 2020). From this vast database of experiments, low-lying energy spectra - specifically 2_1^+ and 4_1^+ states - along with known $B(E2)$ transition probabilities were mined by hand. This was an unfortunate necessity as the experimental

data files are not uniform in structure and in some cases uncertainties are "tacked" onto the end of the quantity. Hence, accessing these via a code or script for a large variety of nuclei is simply not feasible. Additionally, all of these experimental quantities are not known for each nucleus under study. Consequently, when examining certain nuclei they may have a known 2_1^+ state and a known or unknown 4_1^+ state and/or associated transition rate. Hence, the number of theoretical BH calculation data points compared to experiment will vary depending on the quantity under discussion. Furthermore, given the region of prediction for nuclei yet to be observed/measured, no such comparison to experiment can be made. In an attempt to mitigate this some comparisons are made to the previous Gogny D1S BH study [3]. The essential results gathered from the BH study will be made publicly available via an online database which will provide an opportunity to be continuously revised and updated with new content in the future.

3.2.1 Experimental β_2 Deformation Parameter

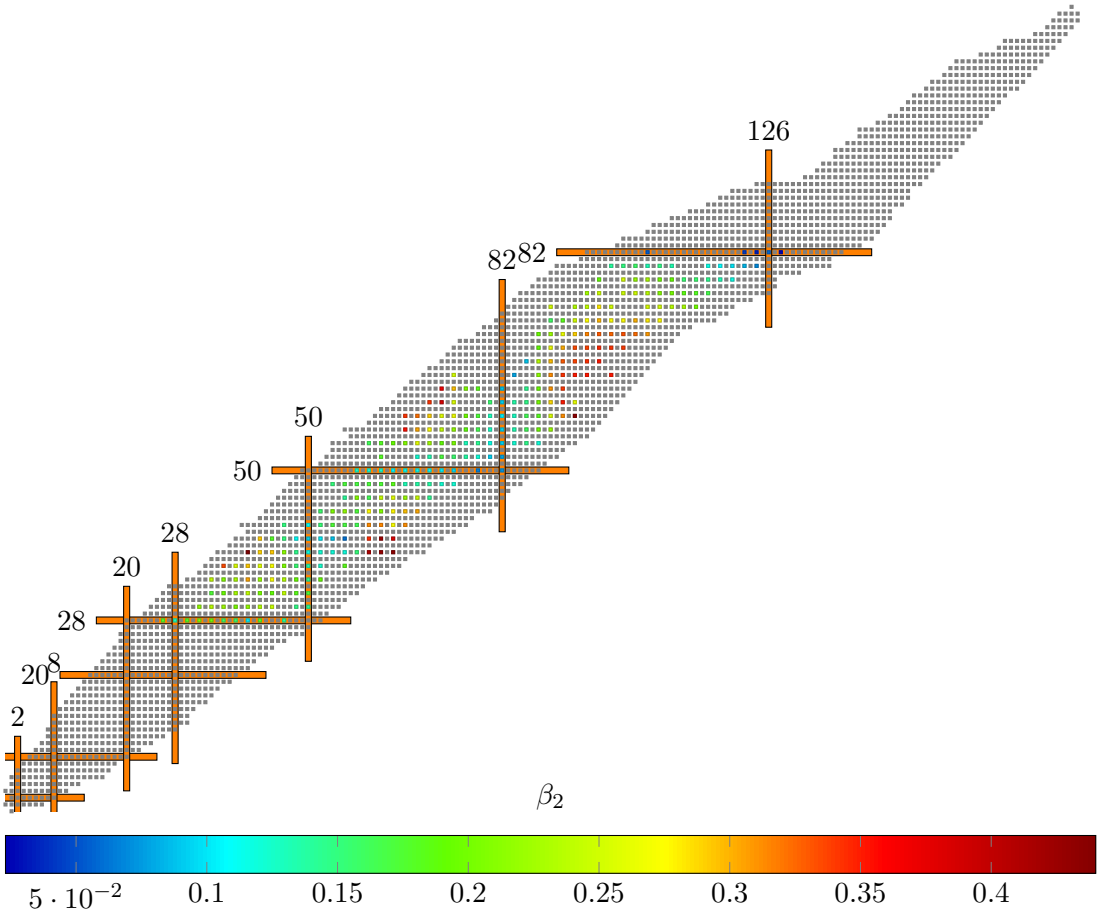

Figure 3.2: Experimental β_2 deformation parameter across the even-even nuclei of the nuclear chart [2].

Figure 3.2 shows the known experimental data from NNDC for the deformation parameter β_2. Caution should be applied in utilising this data as the deformation parameter itself is not an observable. In reality it is calculated from phenomenological models based on observable measurements - typically $B(E2)$ transition rates. Therefore, whilst this provides a guide for theoretical model comparisons, it itself is based on a model and good or bad agreement is not overly strong evidence as to the accuracy or robustness of your theoretical model. Furthermore, as can be observed from the figure, that most of the β_2 values are unknown in the experimental data, typically due to the lack of $B(E2)$ transition rates for the low lying states (specifically between the first 4_1^+ and 2_1^+ states). Nevertheless, having highlighted this warning, given it is a parameter built from experimental data it still provides an interesting comparison of the global trends of nuclei with regards to regions of strong quadrupole deformation and regions of spherical nuclei such as those of magic and semi-magic nuclei which are useful to gauge the successfulness of a model such as BH in this global survey.

3.2.2 First excited $E_{2_1^+}$ state

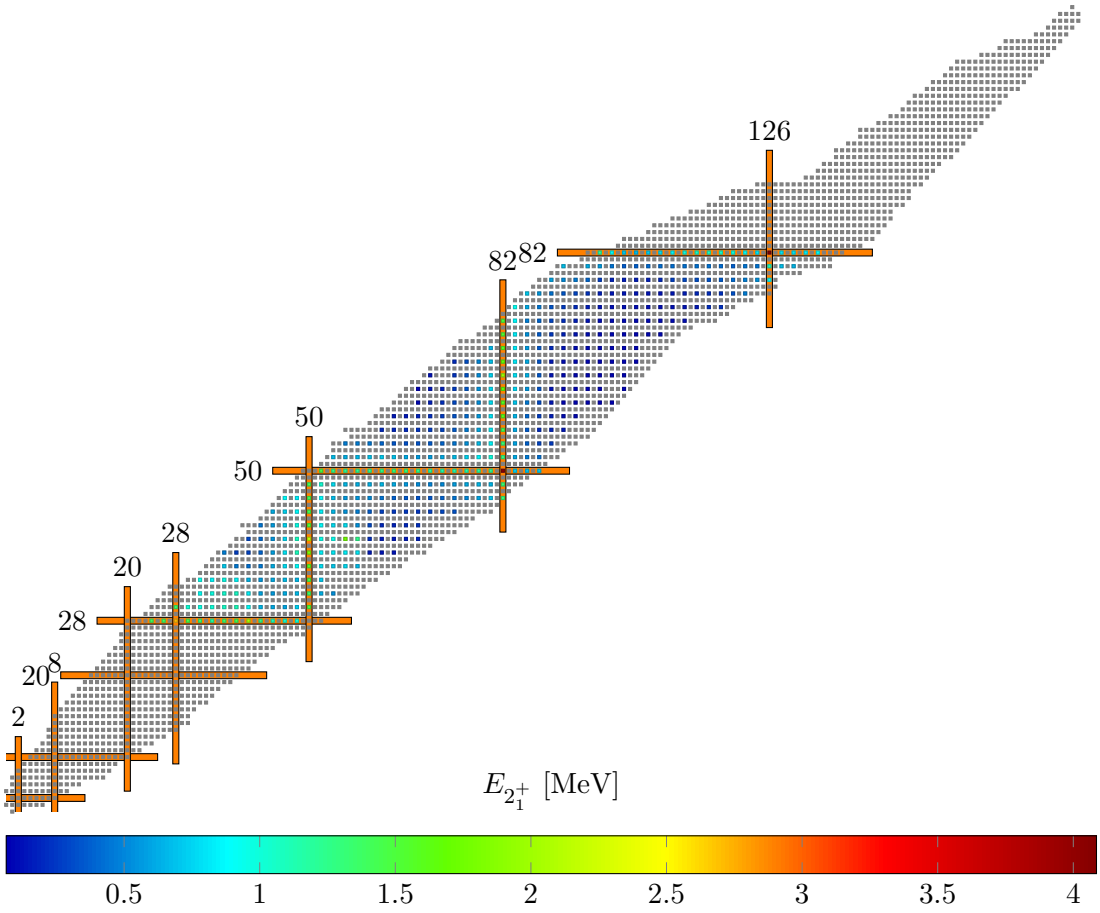

Figure 3.3: Experimental $E_{2_1^+}$ across the nuclear chart [2].

Figure 3.3 shows the first excited 2_1^+ energy levels for the experimentally known nuclei within the survey region. These values are formed from direct experimental measurements (usually a variety of different experimental measurements) all consistent with each other and averaged to minimize the uncertainty in the experimental results. On this point it is noteworthy to point out that generally speaking, the uncertainties associated with the experimental measurements of low-lying states are incredibly small. All theoretical models are far from this level of precision (with the experimental uncertainty sometimes being as small as a few tens of electronvolts (eV)), especially when applied across a large array of nuclei and no fitting on particular observables of a particular nucleus is made. Given that this energy is an observable (i.e. it is directly measurable) and is known for almost every even-even nucleus observed, it provides a key point of comparison to any theoretical model looking to accurately describe deformation properties of nuclei.
The energy of this state peaks for magic and semi-magic nuclei given their magic proton and/or neutron numbers i.e. they have closed shells leading to a substantial increase in the energies of all of their low-lying states as can be seen from figure 3.3. In the cases of magic nuclei where both the proton and neutron numbers are both magic numbers a substantial increase to the region of 1 MeV can be noted for this state.

3.2.3 First excited $E_{4_1^+}$ state

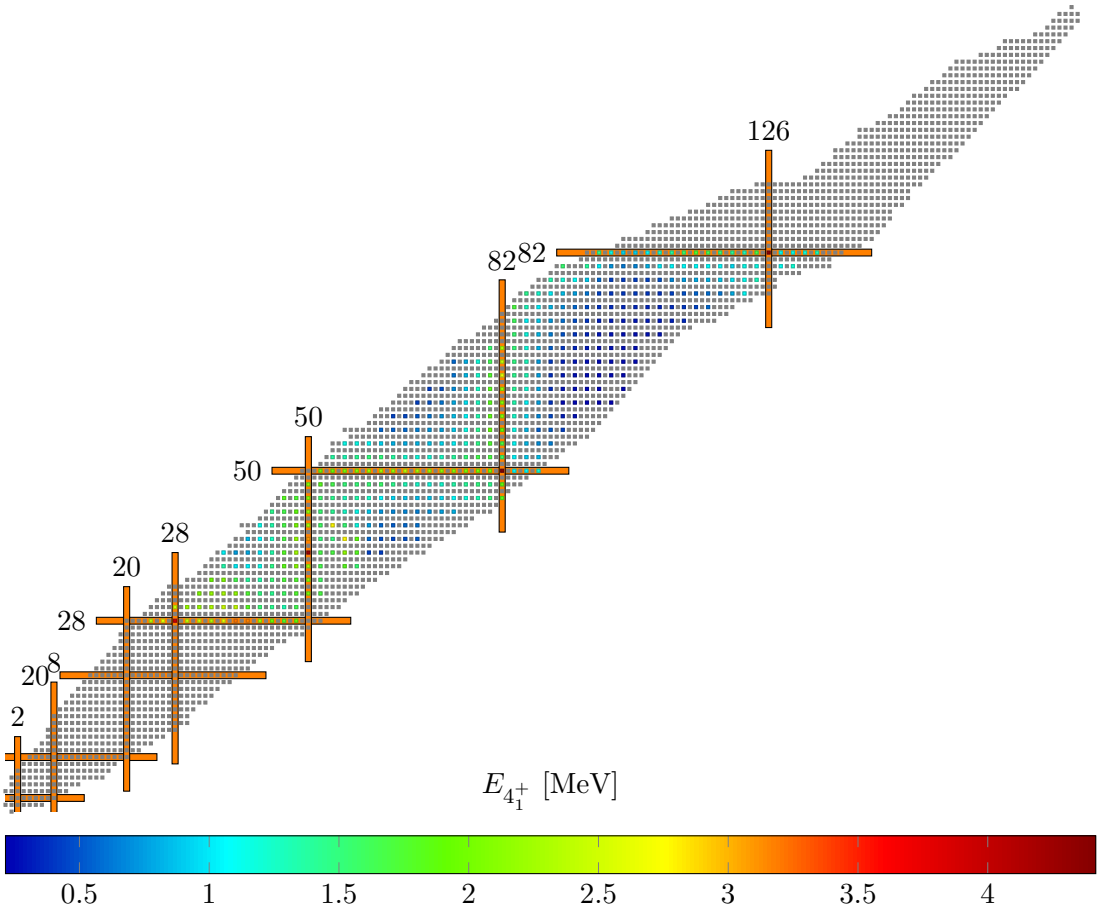

Figure 3.4: Experimental $E_{4_1^+}$ across the nuclear chart [2].

Figure 3.4 follows a similar trend to the that of the 2_1^+ (figure 3.3). The energy of the first excited 4_1^+ lies above that of the 2_1^+ and again peaks for magic and semi-magic nuclei. The ratio between these two states provides a good indication of whether the nucleus is a nucleus which undergoes pure vibration (an equal spacing of the states i.e. a harmonic oscillator) or shows a higher ratio (a coupled vibrational-rotational spectra), a plot of which is available at NNDC [2]. Together, these two observables make for essential analysis in any study of collective excitations.

3.3 Computational Benchmark Tests and Convergence

3.3.1 The Xenon isotopic Chain

Building on the work of [43] and [32] the xenon isotopic chain is reproduced using UNEDF0 in 12 shells with HFODD and the BH code. This was primarily done to become familiar with the existing HFODD code and BH code and begin the outline for the automated computational procedure outlined above. Additionally, this afforded the opportunity of a direct comparison between the outputs of published results and the new automated procedure. It is observed that the minimum $\beta\gamma$ deformation points (figure 3.5), the low-lying 2_1^+ and 4_1^+ states (figure 3.6) along with a collection of other low-lying spectra (figure 3.7) are consistently reproduced in comparison to previous work. These benchmark calculations agree with the aforementioned published work indicating that the automated procedure is working as expected.

Then the isotopic chain was recalculated for the UNEDF1$_{\mathrm{SO}}$ functional to ensure that the procedure could be adapted to calculations with a new choice of functional which it ultimately was. It is easily observed that UNEDF0 is a better fit for the experimental data than that of UNEDF1$_{\mathrm{SO}}$. This isn't overly surprising as it has been fitted on heavier nuclei with a different spin-orbit strength compared to UNEDF1. What is interesting, however, is that the general structure of the states and the low-lying trends of the experimental data appear consistent with the BH procedure regardless of the choice of functional. The functional simply appears to affect the absolute values of the theoretical quantities calculated in the procedure. On this point it is necessary to point out that although these two functionals have differences they are members of the same family of functionals and so it may not be too surprising that the same general structure is reproduced. To finally address this point it would require a wider array of functionals to compare to these calculations. In figure 3.7 there are two columns for each functional - theoretical and theoretical (sc = 1.3). These relate to the bare unscaled BH calculations and a scaled set of BH calculations where the mass parameters are all scaled by 30% to account for the missing Thouless-Valatin terms which account for the dynamical collective component i.e. these terms make a correction to the momentum of the collective motion adding to the static collective component which is present in the current approach ([44] and [45]). This point will be discussed further in subsection 3.3.5.

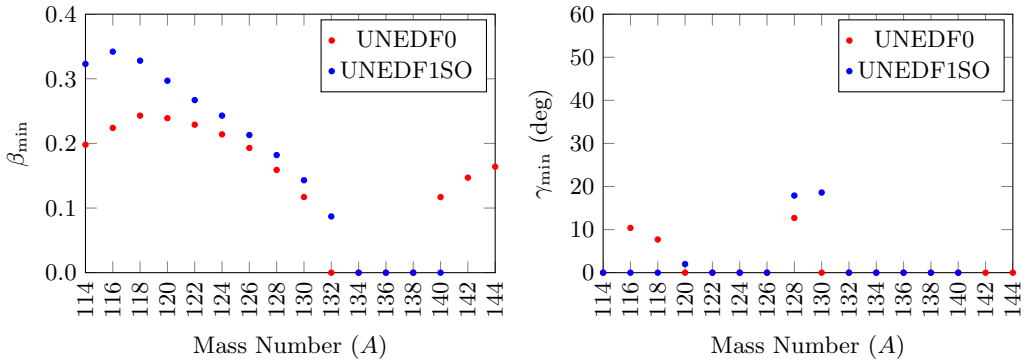

Figure 3.5: (Colour Online) Values of the deformation parameters β_{min} (left panel) and γ_{min} (right panel) at the minimum of the potential energy surfaces for the Xe isotopic chain for UNEDF0 (red) and UNEDF1$_{\mathrm{SO}}$ (blue).

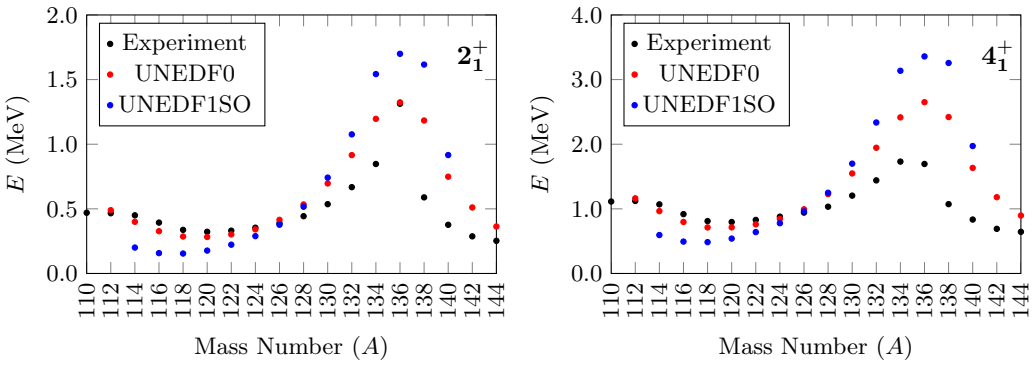

Figure 3.6: (Colour Online) Shows the 2_1^+ (left panel) and 4_1^+ (right panel) energy spectra for the Xe isotopic chain for UNEDF0 (red) and UNEDF1$_{\mathrm{SO}}$ (blue).

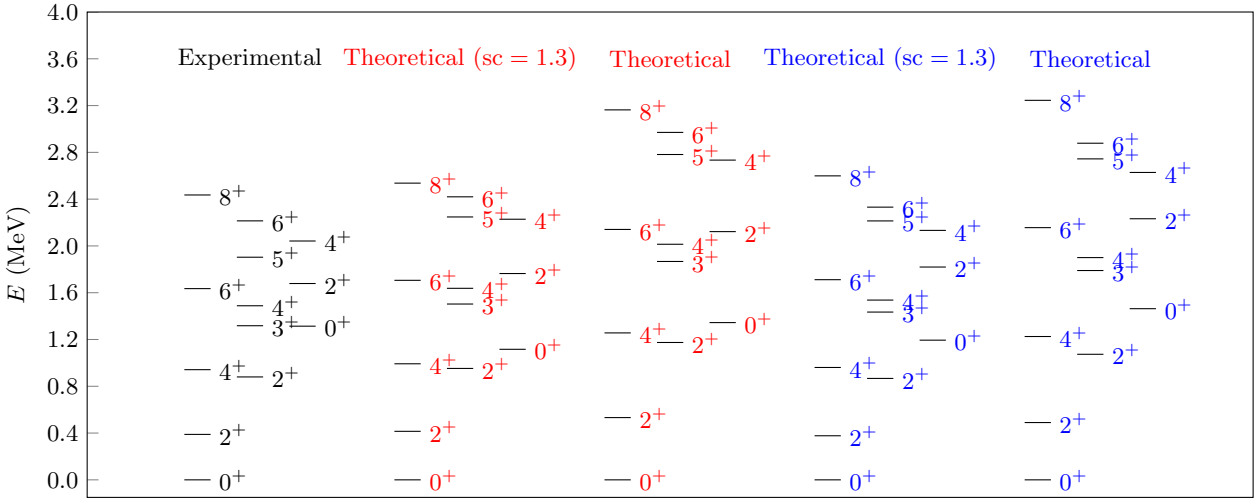

Figure 3.7: (Colour Online) Shows the experimental (left), theoretical with scaling (sc = 1.3) and theoretical without scaling BH calculations for UNEDF0 (red/centre) and UNEDF1$_{\mathrm{SO}}$ (blue/right) energy level schemes for ^{126}Xe.

3.3.2 Computational Runtime and Convergence

Previous BH microscopic calculations of mass parameters from Skyrme functionals were all conducted in 12 shells. To this end, it would be useful to carry out a convergence test examining the impact the number of shells and mesh density of the $\beta\gamma$ deformation plane has on the results of this approach. Hence, a test case nucleus was selected - ^{128}Xe - where it was calculated in 10, 12, 14, 16, 18 and 20 shells for three different (β, γ) mesh densities of $(0.10, 12°)$, $(0.05, 6°)$ and $(0.025, 3°)$.
For clarity, each constrained HFB calculation run at each (β, γ) point will achieve convergence in a different way. Generally speaking small β (and γ) points converge in a matter of hours whilst larger points take between 1-2 days given the chosen convergence criteria. Hence, for any given nucleus it is ideal to allow up to 2 days to run before examining the result. Some nuclei won't fully converge in this time frame whilst others will converge quicker assuming that the individual points can be run in parallel (at the same time) on a computing cluster. A note of caution at this point is essential. In practice most nuclei will not fully converge in the first run and multiple re-runs will be necessary. In reality this means it is impossible to put a time frame on any given calculation as some will converge with minor changes to the numerical parameters whilst others won't achieve convergence with any parameter set implemented over the course of this research. Therefore, it is es-

sential to leave a large amount of additional time to make re-runs (accounting for the fact that these problematic points will themselves generally take longer to run). Furthermore, these re-runs must be made manually as there is no uniform fix for the points which fail. It should be stressed at this point that given these convergence difficulties it was essential to allow multiple points to be run in parallel which speeds up the computational progress of the entire study as low-lying β points tend to converge faster than larger β values. Hence, as each point converges the next point in that nucleus and/or in the next nucleus in the isotopic chain can be run. This leads to the points which may take up to 2 days to run and the points that will not converge to not hinder the runs of the next nucleus. Hence, progress can be made as rapidly as possible whilst acknowledging that manual re-runs will be required after a review of the first run of each nucleus. After convergence is achieved and a converging set of numerical input parameters is found then it will massively speed up reproduction of this work and provide a strong indicator to future research as to how to converge any given nucleus in full triaxial calculations. This is one substantial bi-product benefit of the due-diligence of this work, not only is a database of HFODD calculations for triaxial maps of a wide variety of nuclei made along with the corresponding Bohr Hamiltonian results of observables which can ultimately advance our physics knowledge but it can also provide a template for future studies of single nuclei, chains of nuclei (isotopic or isotonic) in terms of what is required to adequately achieve convergence with other functionals. Additionally, this work (and those which follow) allow a better understanding of the nuclear BH approach to be obtained in terms of nuclei where it applies well and where it is particularly weak in reproducing any given observables.

From figure 3.8 it can be observed that the least dense mesh grid does not identify the same minimum as in the case for the other two more dense meshes. Therefore, we can rule out using a mesh density of $(0.10, 12^\circ)$. Whilst the most dense mesh $(0.05, 3^\circ)$ would in principle be best for calculations it would require 841 calculations per nucleus compared to 221 for the $(0.05, 6^\circ)$ mesh density. Therefore, it is possible to calculate almost 4 complete nuclei compared to 1 at the most dense mesh and it does not appear to add much more detail to the PES. Furthermore, from figure 3.9 and figure 3.10 which compares the results for the energy of two low-lying states (2_1^+ and 4_1^+) and two reduced $B\left(E2\right)$ transition probabilities as a function of the number of shells for the 3 mesh densities, it further highlights that there is little to no differences between the two most dense mesh densities. Whilst it can be observed from figure 3.9 that the energy of the states are not substantially different between the 3 mesh densities or the number of shells there is a slow convergence to the observed experimental energy of these states for a higher number of shells. However, from figure 3.10 there is a far more substantial difference between the lowest dense mesh and the two higher dense meshes. Furthermore, it is clear that the results depend on the number of shells and that a higher number of shells appear to tend to a more consistent converged result than those in a smaller number of shells. Hence using a mesh density of $(0.05, 6^\circ)$ appears to adequately balance computational runtime with accuracy of the PES. Furthermore, it is clear that there are key differences between a low number of shells and a higher number of shells as expected for all of the observables. However, it is clear that the increase in computational time for higher numbers of shells does not show a significant enough return in terms of accuracy to warrant the runtime cost. Hence, calculations should be conducted in 16 shells.

Therefore in principle for each nucleus examined there are 221 (β, γ) points required to cover the $0^\circ - 60^\circ$ deformation sextant in 6° increments in the γ coordinate and 0.05 increments in the β coordinate up to $\beta = 1.0$. In reality, the range $0 - 0.7$ in the β coordinate should be sufficient to describe most nuclei examined resulting in 155 deformation points in the sextant.

Figure 3.11 shows the chosen (β, γ) step-size chosen for the study. The β coordinate step-

size will be 0.05 and the γ coordinate step-size will be 6°. These were chosen to balance (along with the other convergence criteria) computational time to achieve convergence and an appropriate level of accuracy in representing the nuclei examined in the study in 16 shells.
Now that a mesh density for the study has been established the next question is - what constitutes an adequately converged nucleus? This question of course does not have a rigorous answer and so certain criteria must be considered in order to address it appropriately. Initially, the aim is to converge as much of this coordinate map as is possible all the way up to $\beta = 1.0$. At large deformations in and around $\beta = 1.0$ it may often become energetically favourable for a variety of nuclei to undergo nuclear fission. The Bohr Hamiltonian is not intrinsically designed to describe such physics and so going any higher in the β deformation parameter would be extreme overkill and it should not be expected that we could accurately model nuclei at these deformation scales. Furthermore, when scaled by the spherical point, all nuclear studies presenting potential energy surfaces show that the interesting PES features particularly those of competing minima are primarily located at smaller β deformations.

3.3.3 Numerical Stability of Convergence

The HFODD stability criterion [46] is a numerical parameter within the code to measure the convergence between consecutive iterations of the constrained HFB calculations. After a set number of consecutive iterations where this parameter is below the criterion set, the result of the calculation will be identified as converged. This stability criterion was substantially reduced from 10^{-4} to 10^{-6} which can lead to previously converged results becoming unstable given the more stringent criterion placed on the convergence of the HFB procedure. For the survey calculations a choice of enforcing the convergence for 5 consecutive iterations of the code was made (which is an increase from 3 in previous calculations). Nevertheless several deformation points require this more stringent stability criterion to be applied in order to ensure that the microscopic calculations converge for small $\beta\gamma$ deformations. In terms of the manual labour required to converge points that initially fail it is a rather complicated picture. There is no way to predict ahead of the initial computational run which points in any given nucleus will not converge and the subsequent reasons for this lack of convergence. Over the duration of the BH survey many issues with regards to convergence of the microscopic calculations were encountered and are listed below along with steps taken to achieve convergence:

1. Cluster runtime limitations.
   (Maximum of 2 days on the Viking Cluster at the University of York).

   In such cases as this the HFODD slowness parameter [46] can be lowered, providing it does not lead to chaotic divergences, which will accelerate the convergence of the code in fewer iterations. Thus, convergence can be reached within the cluster runtime limitations. For large β values decreasing the slowness parameters to 0.8 and if necessary to 0.7 often adequately addresses this minor issue.

2. Converged to incorrect $\beta\gamma$-deformation points.

   In some cases the code meets the required stability criterion for convergence but in the case of small deformations (low β) they may not correctly have converged to the right β and/or γ values. In this case even more stringent stability criteria must be implemented - typically between $10^{-7} - 10^{-10}$ - and a re-run made.

3. HFODD chaotic divergence.

Chaotic divergences can be caused by several things. Choosing poor numerical parameters in the HFODD input file or calculating a nucleus in the deformation plane where convergence progresses up to a point before getting stuck and oscillating back and forth between consecutive iterations. This phenomenon is due to the switching of single particle states which are very close to one another in energy and results in these states interchanging with each other in consecutive iterations of the HFB procedure and convergence is never obtained. In this case the slowness parameter of HFODD should be increased effectively allowing smaller and smaller step-sizes which can, though not always, prevent the code from getting caught between consecutive iterations. Occasionally, you can get stuck in oscillations in a local minimum rather than the true minimum you wish to converge to and in this case lowering the slowness parameter will allow the code to take larger step-sizes and escape such local oscillations and converge to the desired minimum.
If the slowness parameters cannot address the chaotic divergence encountered then it may become necessary to alter the stiffness [46] of the quadrupole constraints Q_{20} and Q_{22}. These stiffness parameters are another example of a numerical parameter in HFODD which can affect the convergence. Typically these are set to small values of the order of 0.01 but in a limited number of cases where the code fails to converge for any slowness parameters it could be increased, particularly for lighter nuclei, to 0.1.

4. Unbound positive proton chemical potentials in nuclei approaching the proton dripline.

   See section 3.3.4 for details.

The slowness parameter is the key parameter to edit to achieve convergence. It is responsible for the rate at which the self-consistent HFB calculations are carried out. In a sense, it can be thought of as a numerical parameter governing the step-size between consecutive iterations of HFODD. The slowness and stiffness parameters cannot be changed during the running of HFODD. Therefore, any updates to them must be made before manually re-running them based on the convergence of the previous run(s). The true bottleneck lies in choosing an appropriate choice of slowness parameter. Only if you encounter chaotic divergences in early iterations of HFODD should you consider editing the stiffness parameter of the quadrupole constraints. For the first run of a nucleus I recommend, based on my benchmark tests and subsequent experience, choosing a slowness parameter of 0.9 and stiffness for both quadrupole constraints of 0.01. The majority of deformations in the plane converge using these combination of parameters and any which don't can be manually addressed by reviewing the HFODD convergence report for the first run and implementing the appropriate step from the outlined list above. Further discussions on the convergence of HFODD can be found in the manual [46].

3.3.4 Nuclei near the Proton Dripline

In nuclei approaching the proton dripline it is more common for points in the (β, γ) deformation plane to have a zero or slightly positive proton chemical potential resulting in the given nucleus being unbound for that given deformation. This is related to the states near the Fermi energy becoming unbound by the constrained (harmonic oscillator) potential (illustrated by the black dashed lines) implemented in HFODD which may still be bound by the pronounced Coulomb barrier (red) of such proton rich nuclei as illustrated in figure 3.12. Whilst this is strictly speaking true and in principle warrants the exclusion of this nucleus from the following analysis, given the large Coulomb barrier present in (proton rich) nuclei it is reasonable to conclude that the nucleus does indeed remain bound

and provided that any positive proton chemical potential emerging from the microscopic calculations are small (< 0.5 MeV) they can be included in the following work. In such cases presented in this study it is often known that the nuclei exist experimentally and are therefore bound in nature but little to no information with regards to the states and electromagnetic transition rates may be known experimentally at the current time. This can be problematic given that different NEDFs (and more widely different nuclear models) all predict some differences in where they predict both the proton and neutron driplines to be. Hence, guided by experimental evidence, albeit incomplete in many cases approaching the driplines it is reasonable to include such experimentally known nuclei in this study with this given functional.

3.3.5 Thouless-Valatin Scaling

This section highlights a variety of points yet to be made on the survey results and the Bohr Hamiltonian approach more generally. In particular the uniform Thouless-Valatin scaling parameter used in this study. Previous works ([43], [44] and [45]) often quote a range of scaling factors for the mass parameters typically ranging from 1.2 to 1.4 to account for the missing Thouless-Valatin terms in the current implementation of BH. It must be stressed that this factor is not well motivated by any theory work and is applied, usually, in an attempt to obtain better agreement with experiment. However, when this is done on a case by case basis, for a small group of nuclei or one particular chain it is possible to be lead astray by this factor. Hence, in this study it was decided to calculate unscaled BH results and BH results with a uniform choice of scaling factor of 1.3 for all mass parameters over all nuclei included in the study. This allows some analysis to be made regarding the use of this scaling factor. For example, do nuclei in different regions of the chart appear better or worse aligned with specific values of the scaling? Implementing no scaling and a uniform scaling opens a discussion on this question which will undoubtedly take more detailed analysis to ultimately settle but at this point no global calculations exist to base any form of robust argument off of.
There is no fundamental reason why the different mass parameters could not have different scaling parameters. This is too difficult to implement a rigorous test of in the time frame of the study but a future attempt could be made to vary the scaling factors between the different mass parameters in order to see if any mass parameters affect the results of the observables more than others.
It is probable that the scaling accounting for the missing Thouless-Valatin terms would be different for each individual nucleus - the only way to construct such a model rigorously would be through the calculation of a full ATDHFB calculation which is currently beyond the abilities of the theoretical community. It is essential to stress this point firmly. It is a key goal of future work for the whole nuclear theory community to comprehensively implement a full ATDHFB calculation where the Thouless-Valatin terms are explicitly calculated and contribute to the dynamical component of the moments of inertia/mass parameters. The direct inclusion of these terms will combine with the current static component calculated within the current approach and remove the need for any such scaling altogether. Given that this full ATDHFB approach has yet to be implemented there is nothing to compare with the current scaling factor for the inertias. Therefore employing the scaling factor along with unscaled BH results as aforementioned previous works have done, is the best that can currently be done in this survey. It is noted that some initial work has been carried out [44] but even this work acknowledges that their calculations of Thouless-Valatin terms are not complete and employ approximations. Finally, as highlighted in that article people also have carried out these calculations in a variety of different nuclear models which makes any comparison with their results unwise and ultimately inconclusive. In future, once these terms can be fully incorporated into the current

procedure the need for the scaling factor will vanish and this approach will be even more rigorous. This is a promising area of study that strongly deserves further attention in the future. A highly interesting and recent addition has been made in this field in the work of [47] where collective inertias are calculated via a constrained HFB calculation with Skyrme EDF in an attempt to better describe spontaneous fission. This work notes that there is a substantial increase in the collective inertia compared to those calculated in the cranking approximation.
Finally, on this point about the ability to scale results successfully it should be strongly emphasised that the study carried out in the present work is to critic the effectiveness of the Bohr Hamiltonian method with a Skyrme nuclear energy density functional and not to achieve the best (but non-rigorous) agreement with experiment. To this end, figure 3.13 and figure 3.14 highlight the ability of the scaling parameter to fine-tune the energy spectra to achieve stronger agreement with the known experimental results for ^{80}Zr. It is observed that the scaling parameter affects higher angular momentum states more than the low-lying states which are of particular interest in this work. Hence, it is feasible to manipulate this factor to reproduce consistency between theoretical calculations and experimental measurements in the energy spectra. However, a note of caution is needed here. There are many physical effects that will impact the higher order states in nuclei which BH does not account for. Therefore, to blindly look to achieve strong agreement between theory and experiment of many higher states is not good practice. Thus, we focus on the low-lying energy spectra in the present work and the associated transitions between them. Furthermore, this work provides the opportunity to identify observables and/or nuclei where the BH assumptions do not appear to work and fail to reproduce the trends of experiment.

3.4 Summary

Below is a summary of the multiple advances made to this project and the overall computational implementation of the systematic survey of Bohr Hamiltonian calculations which have been discussed in this chapter.

1. Experimental data has been manually mined in a uniform way to allow easier comparison with the computational UNEDF0 BH study.

2. Full triaxial calculations for all nuclei can now be carried out rigorously. Most theory databases to date only contain axial calculations of given nuclear energy density functionals.

3. Convergence of all $\beta\gamma$ points up to at least $\beta = 0.7$ (and in the vast majority of cases up to $\beta = 1.0$) has been achieved. These results require no interpolation or rounding of deformation points in the $\beta\gamma$ plane i.e. a more accurate result is achieved.

4. Convergence of the microscopic HFB calculations is achieved for 5 consecutive HFODD iterations instead of 3 i.e. a more numerically stable computational result is now obtained.

5. The numerical stability criterion of the microscopic HFB calculations in HFODD has been reduced from 10^{-4} to 10^{-6} i.e. a more numerically stable and accurate computational result is now obtained.

6. Benchmark tests have been carried out with regards to the number of shells and number of $\beta\gamma$ mesh points required to achieve accurate results whilst balancing the computational runtime cost. Calculations will be carried out in 16 shells. This is an

improvement on previous calculations done in 12 shells and leads to a more accurate result in principle. Additionally, the general structure of the $\beta\gamma$ deformation plane along with the accuracy of the results for both energy spectra and $B\left(E2\right)$ transition rates appears satisfactory for a mesh density of $\beta_{\text{stepsize}} = 0.05$ and $\gamma_{\text{stepsize}} = 6°$.

7. A benchmark has been made to show the adaptability of the systematic procedure to different NEDFs with the initial work on UNEDF1$_{\text{SO}}$ for the xenon isotopic chain in 12 shells.

The work presented in this chapter laid the foundations for a rigorous systematic survey of medium-to-heavy mass nuclei to be carried out. Much effort and coding was needed to create the outlined procedure to efficiently flow through a wide range of adaptable inputs, run numerous microscopic calculations (221 deformation point calculations per nucleus) across a vast array of (over 500) even-even nuclei and generate converged outputs necessary to apply the Bohr Hamiltonian procedure to them. In addition to the systematic construction, benchmarks and stability tests as well as numerical convergence have been rigorously investigated over the course of the resultant survey and substantial computational improvements have been made to previous work. All of this work allows the following systematic survey to be carried out robustly and compare theoretical BH predictions for multiple nuclear observables, such as energy spectra and reduced $B\left(E2\right)$ transition probabilities, directly to experimental measurements.

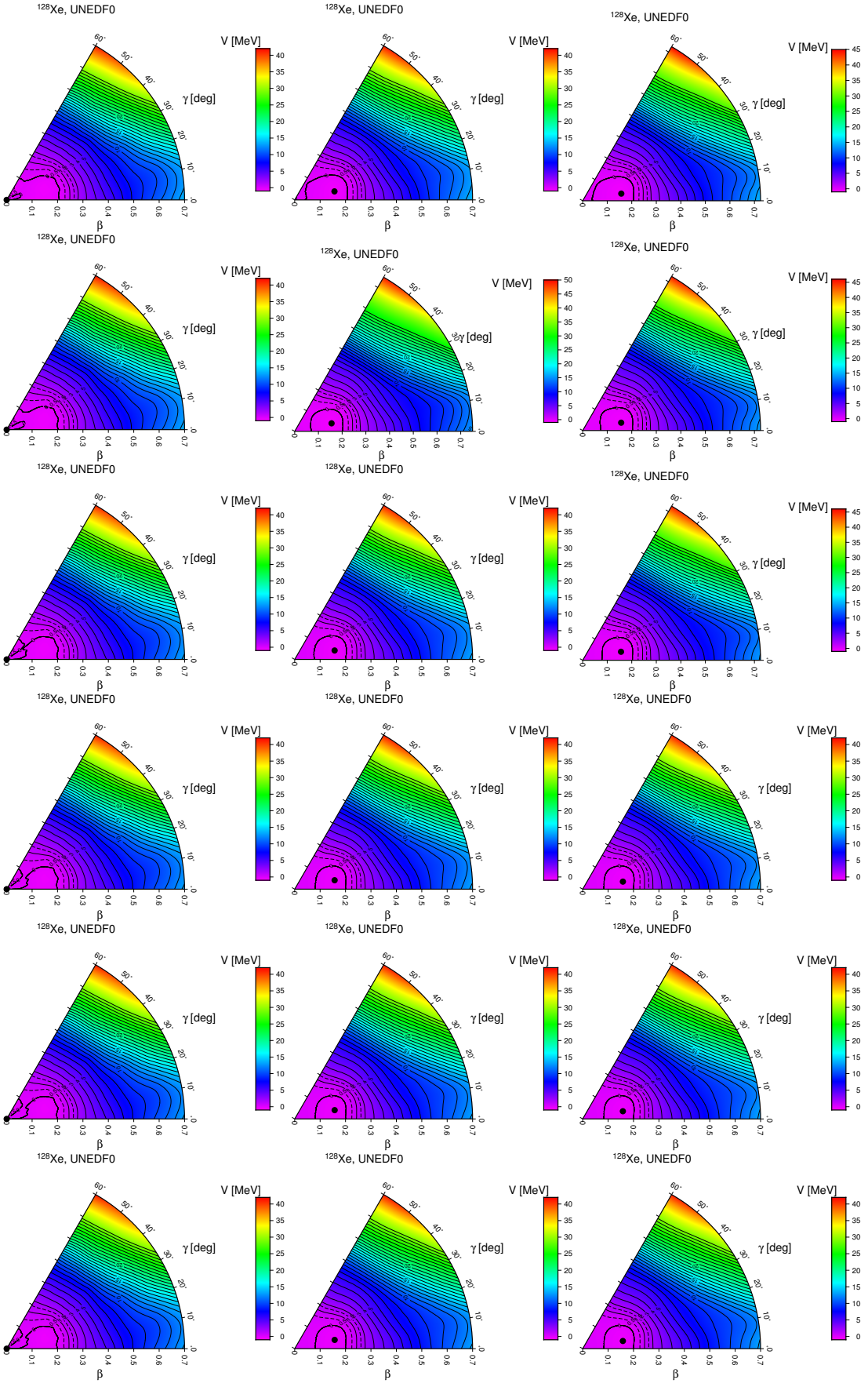

Figure 3.8: (Colour Online) Convergence Tests: Potential energy surfaces for the ^{128}Xe test case with 10, 12, 14, 16, 18 and 20 shells (from top row to bottom row) for the three following mesh densities $(\beta_{\text{Step}}, \gamma_{\text{Step}}) = (0.100, 12°), (0.050, 6°), (0.025, 3°)$ (shown left to right in the diagram above).

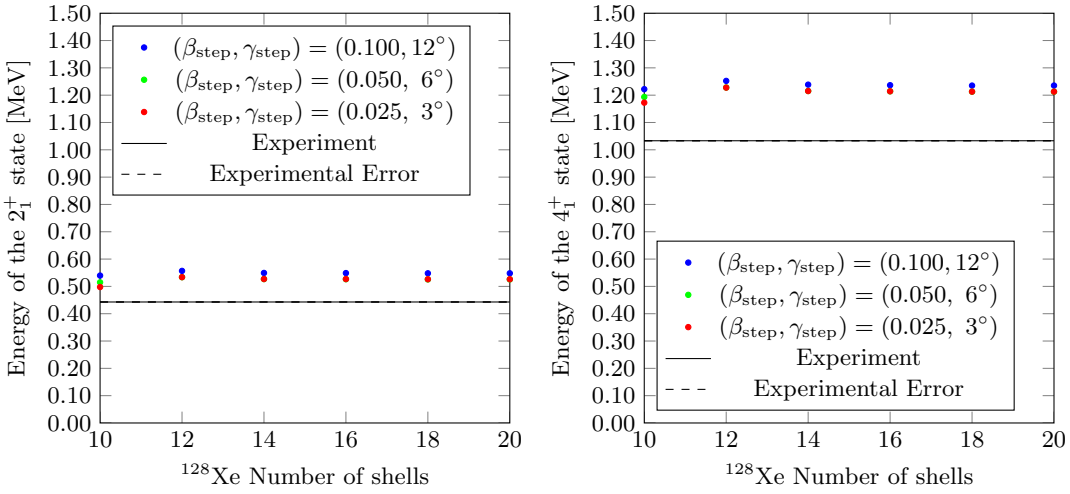

Figure 3.9: Comparison of the 2_1^+ and the 4_1^+ for different $\beta\gamma$ mesh densities in a varying number of shells.

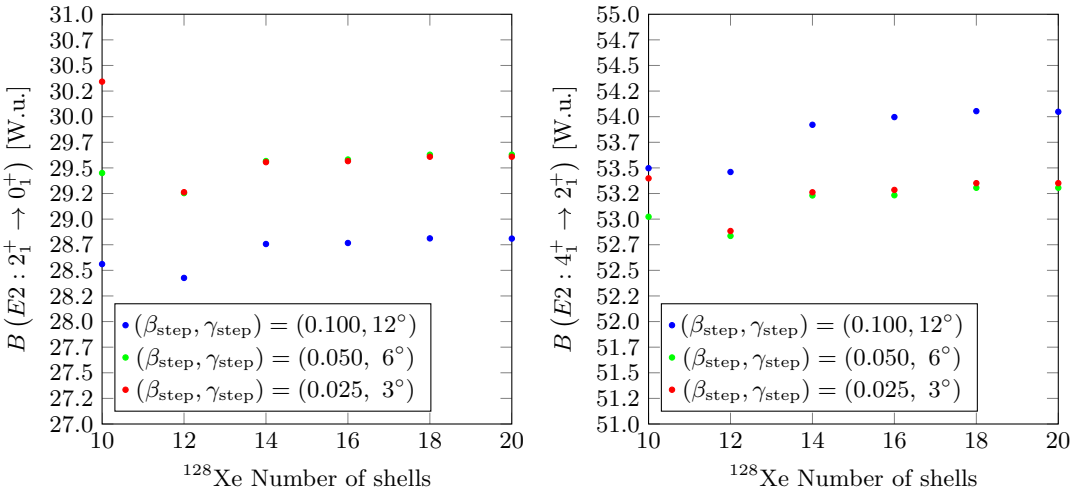

Figure 3.10: Comparison of the $B\,(E2)$ transition probabilities for different mesh densities in a varying number of shells.

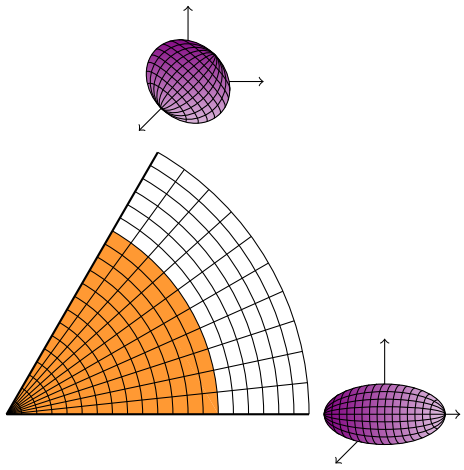

Figure 3.11: The (β, γ) plane sextant describing nuclear quadrupole deformation.

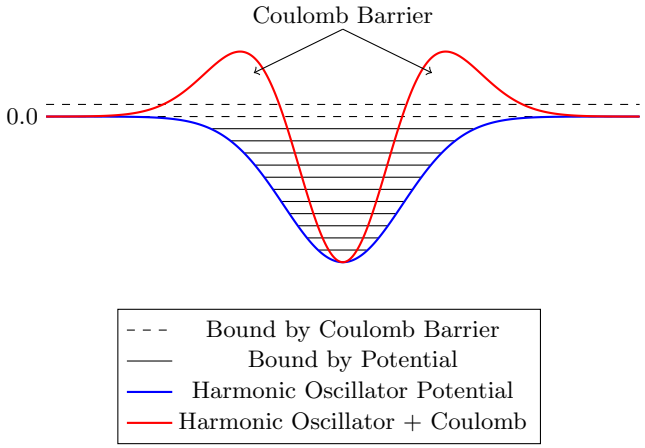

Figure 3.12: Illustration of certain states with zero or small positive energies unbound by the given potential but still bound by the Coulomb barrier.

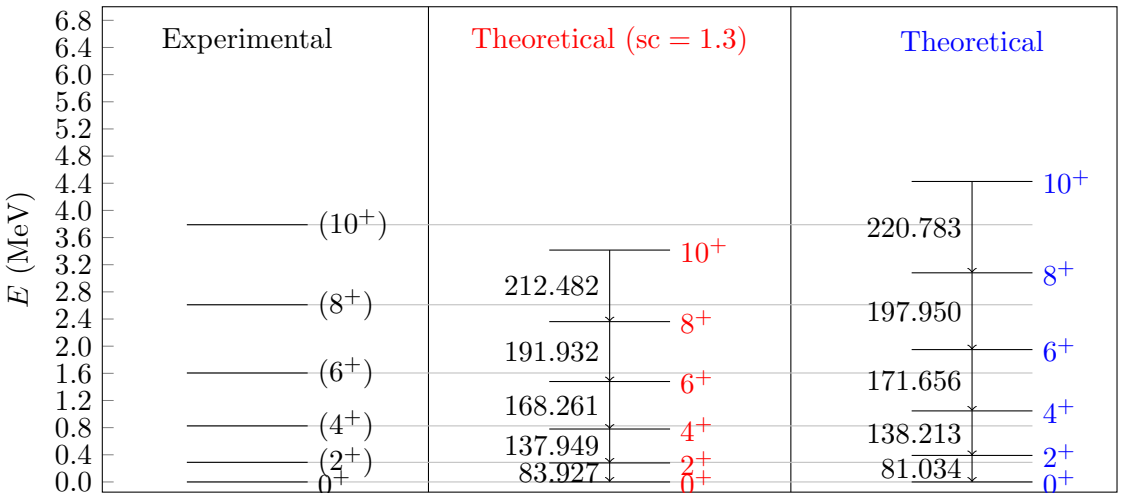

Figure 3.13: (Colour Online) Experimental (left panel), theoretical with scaling (sc = 1.3) (centre panel) and theoretical (right panel) energy level schemes for ^{80}Zr with the UNEDF0 functional.

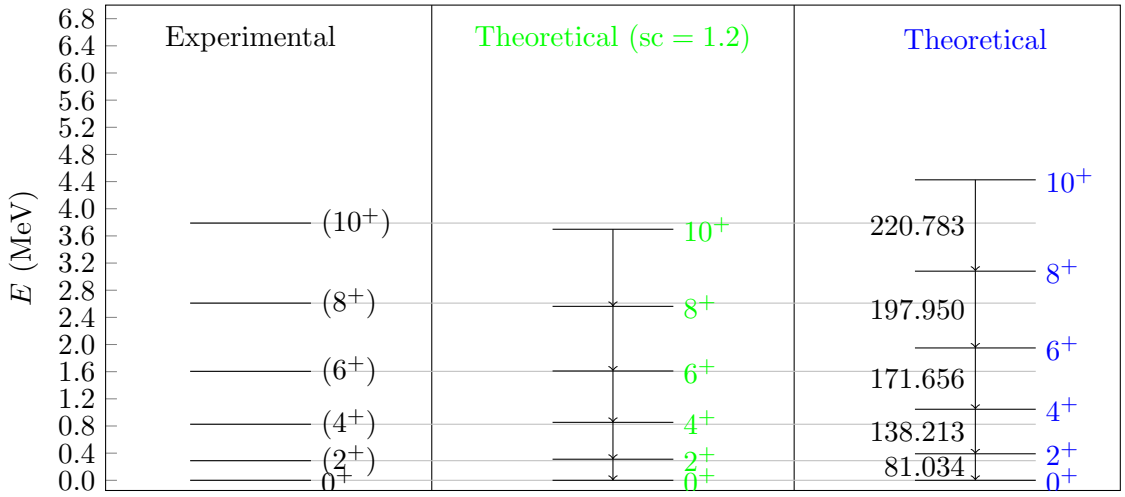

Figure 3.14: (Colour Online) Experimental (left panel), theoretical with scaling (sc = 1.2) (centre panel) and theoretical (right panel) energy level schemes for ^{80}Zr with the UNEDF0 functional.

Chapter 4

Bohr Hamiltonian Survey Results

Outlined in this chapter are the global trends of the results for the systematic UNEDF0 study through illustrations of the nuclear chart as well as individual isotopic chains (and nuclei of specific interest) which are examined in further detail. These aim to address the key aims and objectives outlined in the introduction by shedding light on the reliability of the Bohr Hamiltonian (BH) method as a systematic approach to describing collective quadrupole deformation across the nuclear chart with a Skyrme functional - UNEDF0. Specifically, the erbium isotopic chain is examined in further detail as it lies in the middle of the rare-earth region which provides a strong candidate to explore both strengths and weaknesses in the approach. Following this, the lighter example of the krypton isotopic chain is explored in detail with 3 Skyrme functionals - UNEDF0, UNEDF1, UNEDF1$_{\mathrm{SO}}$ to examine what impact the choice of functional has on the approach. Following this is a discussion of the approach applied to even-even $N = Z$ nuclei which was of particular interest to experimental collaborators along with a brief study of the mirror nuclei ^{70}Kr and ^{70}Se. This chapter culminates in a summary discussion of the collective wavefunctions for a group of nuclei all exhibiting different nuclear deformation properties.

Given the large number of even-even nuclei encompassed by this study it is impossible to present and discuss, in detail, each nucleus. Furthermore, given the main aim of the study is to examine global isotopic trends and any potential evolution of these trends across the nuclear chart it is not a necessity of this work to get involved in such a detailed analysis. To this end, a database is under construction encompassing all of the individual data gathered in this study and is accessible at the following link: `https://webfiles.york.ac.uk/nuclearBH/`
The aim of this database is to continue to grow in terms of both the number of theoretical calculations of nuclei included and the accompanying analysis of these results. Hence, the database will continue to be updated and improved over time.

4.1 Ground State Properties

In this section we look at the global trends in ground state properties of the nuclei examined in this study - specifically the strength of the deformation through the β_2 parameter and the type of deformation (axial (prolate or oblate) or triaxial) through the γ parameter.

4.1.1 Minimum $\beta\gamma$ Deformations

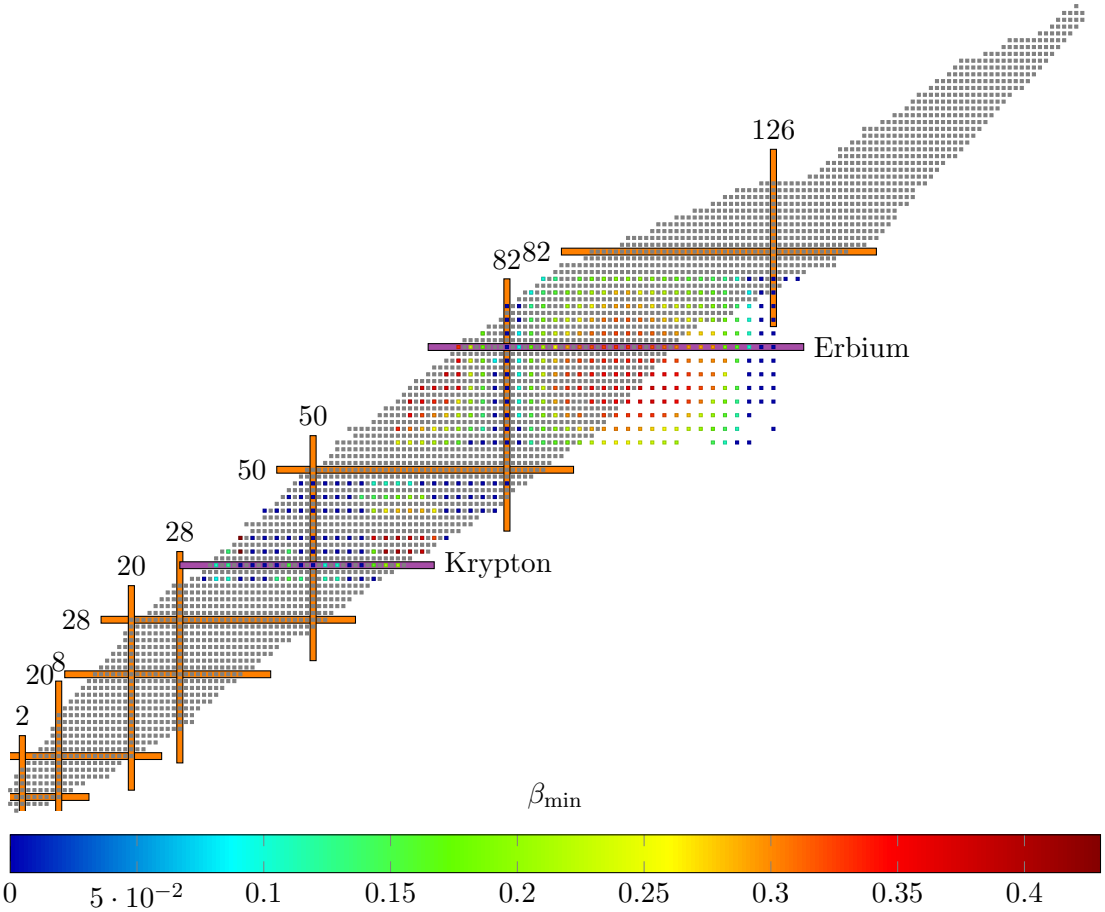

Figure 4.1: $\beta_{\min}$ deformation across the nuclear chart.

Figure 4.1 shows the results of the minimum β_2 deformation parameter for the UNEDF0 BH study. Recall that the deformation in this work is defined through both $\beta\gamma$ deformation parameters resulting in β being a strictly positive quantity here. Several key features are observed which are consistent with previous theoretical work - the Gogny D1S BH Study [3]. Firstly, the calculations clearly show that the majority of nuclei across the survey region are deformed. The original survey region ($Z = 50 - 82$, $N = 82 - 126$) of the rare-earth isotopes shows a very strong region of deformation with the maximum deformation in this region lying between $\beta = 0.4$ and $\beta = 0.5$. Furthermore, as we approach magicity we see this pronounced deformation weakens towards zero (as should be the case for spherical nuclei).

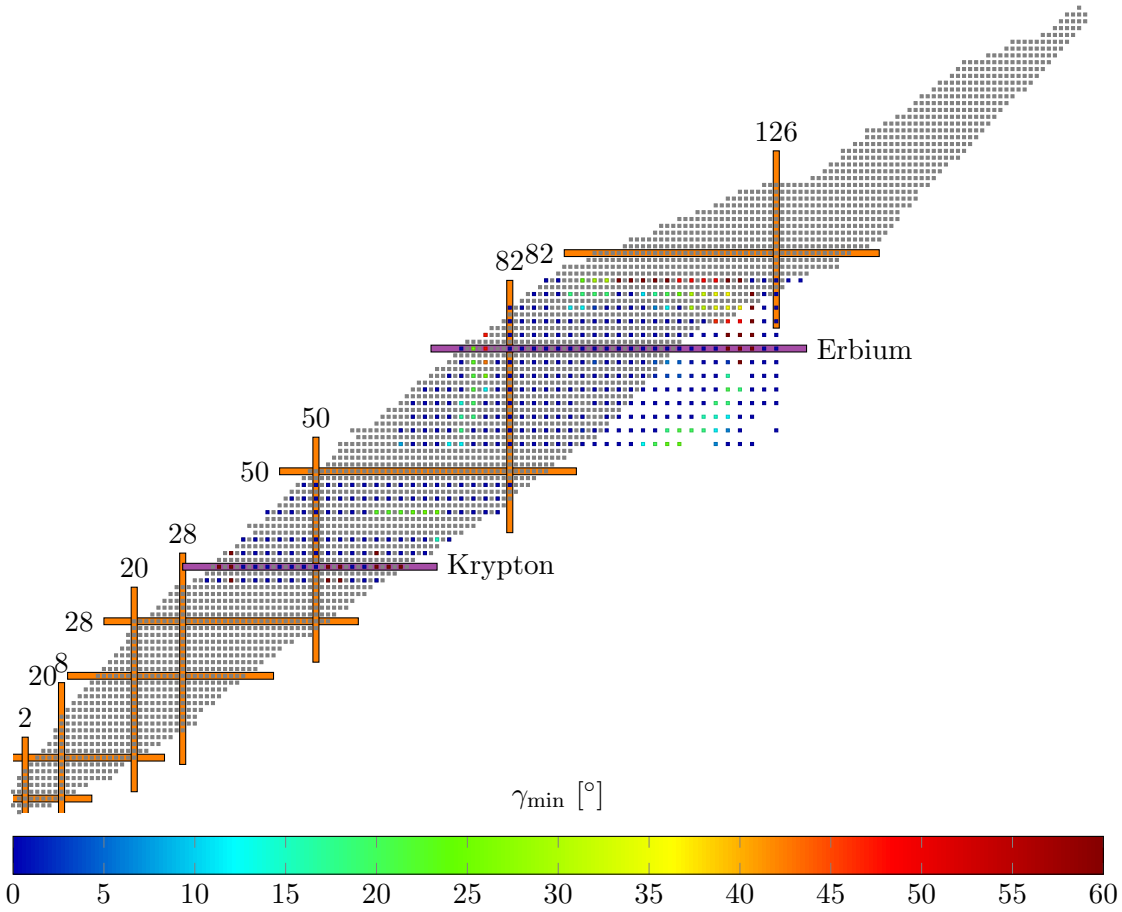

Figure 4.2: γ_{min} deformation across the nuclear chart.

Figure 4.2 shows that the majority of nuclei in the rare-earth region are predicted to be axially deformed. Moreover, the majority of nuclei have a prolate shape from our calculations ($\gamma_{\text{min}} = 0°$) as this is more energetically favourable. Throughout the BH study the potential energy surfaces indicate that a prolate shape is, generally speaking, far more energetically favourable that that of an oblate shape. Some nuclei, specifically lighter than those studied in the rare-earth region (located between $Z = 28 - 50$ and $N = 28 - 82$) can show oblate deformation usually where the PES is relatively flat for small β deformation leading to a less well-defined minimum or in some cases competing minima which can lead to nuclei exhibiting shape coexistence. Furthermore, the heavier the nucleus, the more energetically favourable it is for the shape to transition from prolate through a region of triaxiality reaching an oblate shape towards the lead isotopic chain and/or as isotopic chains become neutron rich, according to these theoretical calculations.

4.2 Excited States

This section outlines the global survey results for selected low-lying energy spectra $\left(2_1^+\right.$ and $\left.4_1^+\right)$ and associated $B\left(E2\right)$ transition rates.

4.2.1 The Erbium Isotopic Chain

The erbium isotopic chain provides an ideal example to examine the robustness of the BH approach with as it is a medium to heavy mass nuclei lying in the centre of the rare-earth region of the nuclear chart which, from several theoretical studies - including this one - is theorised to be highly deformed and provides a long isotopic chain which can be compared to experiment as well as offering a (neutron rich) region of prediction for future experimental efforts.
We will begin by examining the ground state properties of the chain. From the top panel of figure 4.3 it is clear that the erbium chain appears strongly deformed, peaking at around $\beta_{\text{min}} = 0.4$, in these calculations. As expected for the semi-magic nuclei contained within the chain (^{150}Er and ^{194}Er) they are indeed spherical i.e. $\beta_{\text{min}} = 0$. From the bottom panel of figure 4.3 it is clear that the calculations predict nuclei closer to the proton dripline to be triaxial, specifically ^{144}Er and ^{146}Er. Other than 3 neutron rich nuclei (^{186}Er, ^{188}Er and ^{190}Er) which appear oblate in shape, the remainder of the isotopic chain is clearly axially prolate deformed in these calculations.

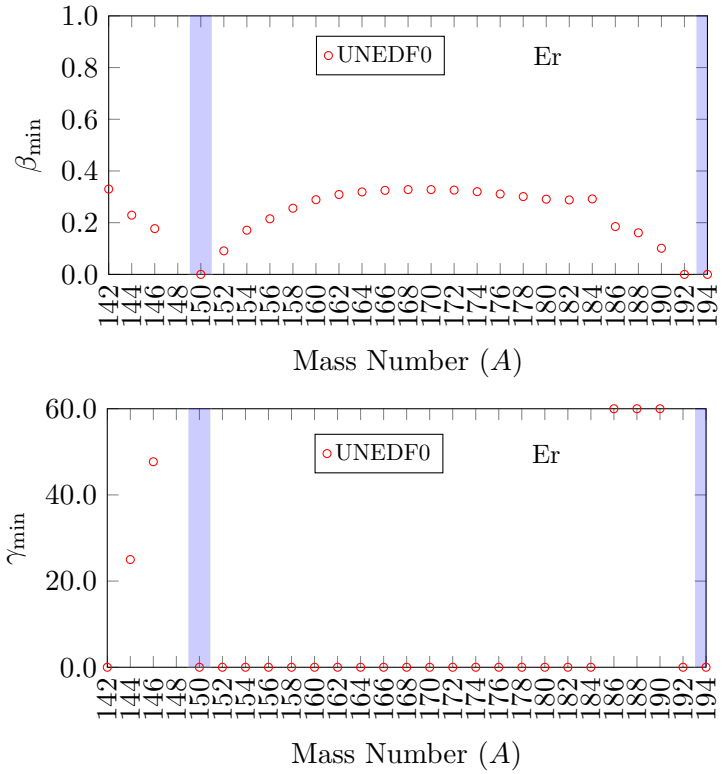

Figure 4.3: (Colour Online) Shows the evolution of the β_{min} (top panel) and γ_{min} (bottom panel) across the erbium isotopic chain for UNEDF0 BH calculations (red hollow circles). The light blue bands highlight the semi-magic nuclei ^{150}Er and ^{194}Er.

From figure 4.4 it is clear that the BH calculations with UNEDF0 accurately reproduce the general trend of the known experimental data for this isotopic chain. As previously stated, there are inaccuracies around the semi-magic erbium nuclei (^{150}Er and likely ^{194}Er) but away from magicity the low-lying states for the deformed nuclei in this chain are

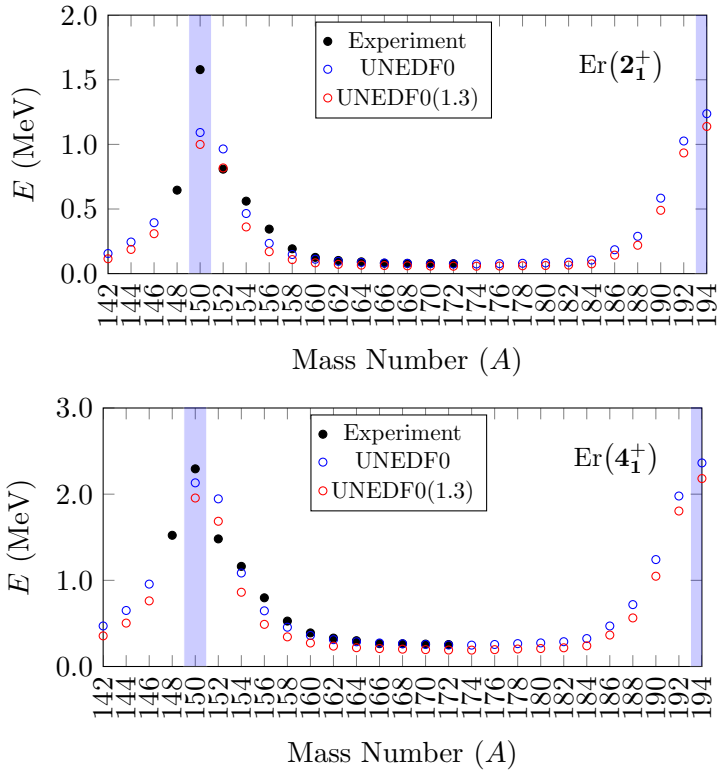

Figure 4.4: (Colour Online) Shows the evolution of the energies expressed in MeV of the first excited 2_1^+ (top panel) and 4_1^+ (bottom panel) states across the erbium isotopic chain for scaled UNEDF0 BH calculations represented by red hollow circles and unscaled UNEDF0 BH calculations represented by blue hollow circles and compare them to the experimental results [2] represented by the solid black dots. The light blue bands highlight the semi-magic nuclei ^{150}Er and ^{194}Er.

consistent with known experiment. The consistency with experiment is more easily seen through figure 4.5, a plot of theory calculations against experimental observations, where it is observed that the unscaled BH calculations are a more accurate fit for the experimental data than those where the mass parameters have been scaled with a factor of 1.3 to account for the missing Thouless-Valatin terms in our calculations. Ultimately this is a consequence of the pairing strength of the model. It is important to take this scaling in context as little is understood about the best way to uniformly apply such a scaling factor in these calculations and hence why it is often used to adjust individual calculations to obtain the best agreement with experiment. In this context however, it can be used to provide an insight into the uncertainty associated with such calculations by observing its impact across the survey region when uniformly applied.

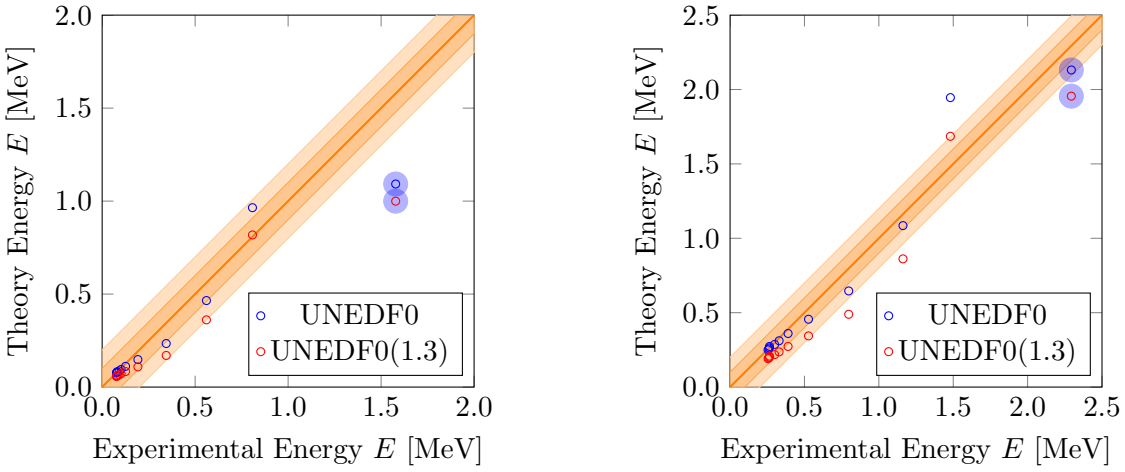

Figure 4.5: (Colour Online) Shows the first 2_1^+ (left panel) and 4_1^+ (right panel) theoretical energy states against the corresponding experimentally measured states [2] for scaled and unscaled UNEDF0 BH calculations. To guide the eye we add errorbars of ±100 keV (inner bound) and ±200 keV (outer bound). Highlighted in large circles is the semi-magic ^{150}Er nuclei.

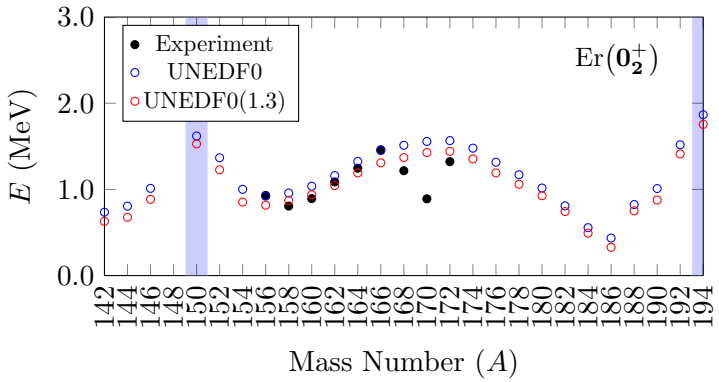

Figure 4.6: (Colour Online) Shows the first excited 0_2^+ state predictions from scaled (red hollow circles) and unscaled (blue hollow circles) UNEDF0 BH calculations along with the known experimental states shown by solid black dots.

Figure 4.6 shows the first excited 0_2^+ state. It is interesting to compare the BH calculations to a variety of states in order to evaluate its robustness further. Given the energies of the 2_1^+ and 4_1^+ are well matched it implies that the erbium chain is likely well described, in terms of low-lying spectra, as a mixture of vibrational and rotational spectra. The 0_2^+ state also appears well reproduced for the known experimental data which is encouraging. Furthermore, from figure 4.7 which shows the first four excited states (2^+, 4^+, 6^+ and 8^+) in the ground state band all exhibit the same trend with these calculations. The semi-magic nucleus ^{150}Er (which is spherical) should not exhibit rotational spectra given its spherical nature and should appear as a solely vibrational spectra as it does in these calculations. In terms of the remaining nuclei in the chain, which are believed to show strong quadrupole deformation, the ratio of their low-lying 4_1^+ and 2_1^+ states is not a pure vibrational spectrum but instead a coupling of rotational and vibrational spectra as expected for nuclei with axial symmetry [27].

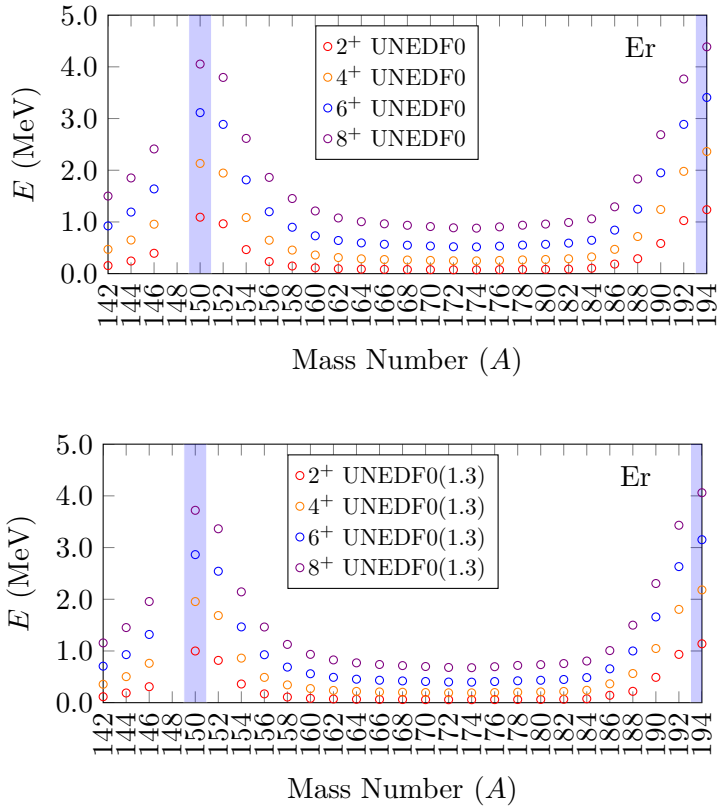

Figure 4.7: (Colour Online) A collection of the low-lying energy spectra of the erbium isotopic chain calculated using UNEDF0 BH calculations. The top panel presents the unscaled results whilst the bottom panel includes the Thouless-Valatin scaling of a factor of 1.3 of the microscopic HFB mass parameters.

The following discussion regarding the calculation of the reduced transition probabilities was obtained from [48]. In order to calculate the $B\left(E2\right)$ transition probabilities we require matrix elements of the following type

$$\langle \Psi_j^{I_j M_j} | W_m^{l,\mathrm{LAB}} | \Psi_i^{I_i M_i} \rangle, \tag{4.1}$$

where Ψ_j^{IM} is the j^{th} eigenfunction of the Bohr Hamiltonian and W is an operator (the $E2$ operator in the case of the $B\left(E2\right)$ transition probabilities) which transforms like an l rank tensor under rotations. Moreover we assume that this operator is known in the intrinsic frame (see equation 4.8). For completeness, the connection between the operator in the intrinsic frame $W_m^{l,\mathrm{INT}}$ and the laboratory frame $W_m^{l,\mathrm{LAB}}$ is given by the following expression

$$W_m^{l,\mathrm{LAB}} = \sum_n D_{mn}^{*l}\left(R\right) W_n^{l,\mathrm{INT}}. \tag{4.2}$$

The matrix element (equation 4.1) can also be expressed by the reduced matrix element of W as follows

$$\langle \Psi_j^{I_j M_j} | W_m^{l,\mathrm{LAB}} | \Psi_i^{I_i M_i} \rangle = \frac{(I_i M_i l m | I_j M_j)}{\sqrt{2I_j + 1}} \langle \Psi_j^{I_j} || W^{l,\mathrm{LAB}} || \Psi_i^{I_i} \rangle, \tag{4.3}$$

where $(I_i M_i l m | I_j M_j)$ is the Clebsch-Gordan coefficient.
In the intrinsic frame of reference and as input to the BH the quadrupole operator Q is

determined by two functions

$$q_0(\beta,\gamma) = \frac{1}{2}\sqrt{\frac{5}{4\pi}}Q_0 \tag{4.4}$$

$$\sqrt{2}q_2(\beta,\gamma) = \frac{1}{2}\sqrt{\frac{5}{4\pi}}Q_2, \tag{4.5}$$

where

$$Q_0 = \left\langle \sum_{i=1}^{Z} \left(2z_i^2 - x_i^2 - y_i^2\right) \right\rangle \tag{4.6}$$

$$Q_2 = \left\langle \sum_{i=1}^{Z} \sqrt{3}\left(x_i^2 - y_i^2\right) \right\rangle, \tag{4.7}$$

as calculated in the constrained HFB calculation within HFODD. Hence, the appropriate numerical scaling factors in equations 4.4 and 4.5 is required when porting the quadrupole moments from HFODD to the BH code. This step is automated by the codes and scripts created in order to automate these calculations and is discussed fully in chapter 3. The final result for the reduced $E2$ matrix element obtained from the BH via the collective wavefunctions is given by

$$\begin{aligned}\langle \Psi_j^{I_j} || E2^{\mathrm{LAB}} || \Psi_i^{I_i} \rangle = \sqrt{2I_j+1} \Bigg[& \sum_{K\in\Delta_{I_i}} (I_i K 2, 0 | I_j K) \int_{\mathrm{def}} \psi_{j,K}^{I_j} q_0 \psi_{i,K}^{I_i} d\tau_0 \\ & + \frac{1}{\sqrt{2}} \Bigg(\sum_{K\in\Delta_{I_i}} \sqrt{1+\delta_{K0}}\,(I_i K 2, 2 | I_j K+2) \int_{\mathrm{def}} \psi_{j,K}^{I_j} q_2 \psi_{i,K+2}^{I_i} d\tau_0 \\ & + \sum_{K\in\Delta_{I_i}, K\geqslant 2} \sqrt{1+\delta_{K2}}\,(I_i K 2, -2 | I_j K-2) \int_{\mathrm{def}} \psi_{j,K}^{I_j} q_2 \psi_{i,K-2}^{I_i} d\tau_0 \Bigg) \Bigg] .\end{aligned} \tag{4.8}$$

The spectroscopic $E2$ moment for a given state is defined as

$$Q_{\mathrm{spec},I_j} = \frac{(II20|II)}{\sqrt{2I+1}} \langle \Psi_j^I || E2^{\mathrm{LAB}} || \Psi_j^I \rangle. \tag{4.9}$$

In order to calculate reduced matrix elements within the BH code the user must provide the values of the q_0 and q_2 functions at the same $\beta\gamma$ grid points as used for the Hamiltonian functions. Apart from the definitions of the intrinsic quadrupole moments no additional approximations or assumptions are made during evaluation of the reduced $B(E2)$ transition probabilities.
Figure 4.8 shows the $B\left(E2: 2_1^+ \to 0_1^+\right)$ and $B\left(E2: 4_1^+ \to 2_1^+\right)$ transition rates between the low-lying states (in W.u.) where the reduced transition probabilities are given by

$$B(E\lambda: J_i \to J_f) = \frac{\langle f|\hat{E\lambda}|i\rangle^2}{2J_i+1}, \tag{4.10}$$

where i represents the initial state, f represents the final state, $\hat{E\lambda}$ represents the $E\lambda$ transition operator and finally J_i and J_f represent the angular momenta of the initial and final states respectively. Again, although there is less experimental data on these observables, the data we have are reproduced well by the BH results with the majority of calculations lying within the experimental errorbars. Similar to the energy spectra (figure

4.4) approaching the semi-magic nuclei the scaled and unscaled BH calculations differ more than in the centres of chains where, in the case of the $B\left(E2\right)$, they basically overlap. Being successful in modelling multiple observables adds weight to the robustness of the BH approach within its scope of adequately describing quadrupole deformed systems and gives insights into the underlying structure of such nuclei in terms of the quantities that are not observables and only calculated theoretically.

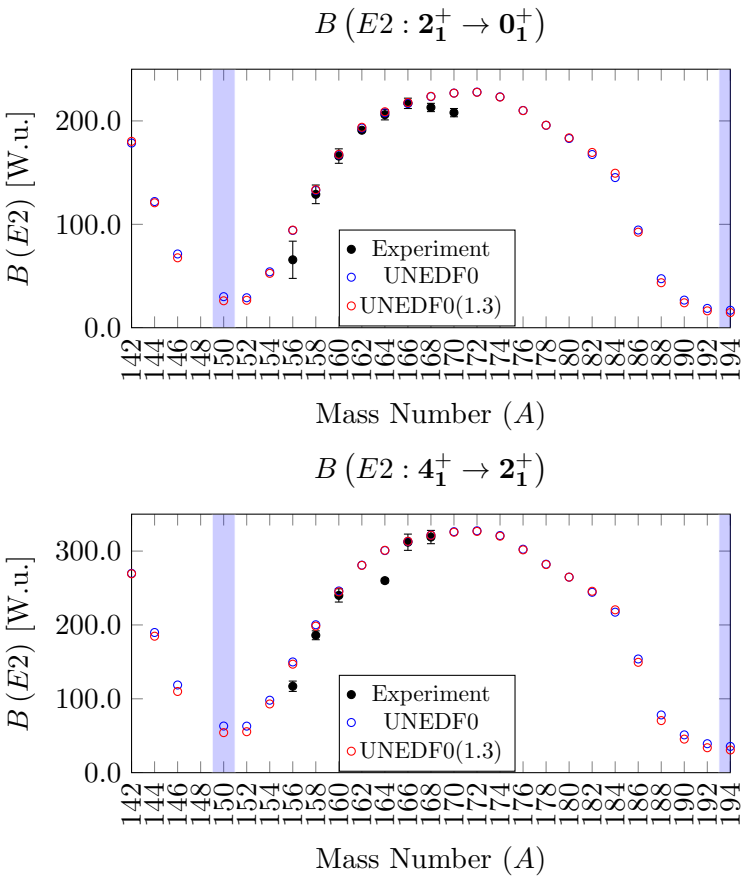

Figure 4.8: (Colour Online) Shows the $B\left(E2:2_1^+\rightarrow0_1^+\right)$ (top panel) and $B\left(E2:4_1^+\rightarrow2_1^+\right)$ (bottom panel) transition probabilities compared to experimental data [2] across the erbium isotopic chain for scaled (red hollow circles) and unscaled (blue hollow circles) UNEDF0 BH calculations.

Now, turning our attention to look more specifically at different nuclei in the erbium isotopic chain exhibiting different deformation behaviour. Figure 4.9 shows the PES for three selected examples of the chain - the semi-magic (spherical) nucleus ^{150}Er, a transitional nucleus ^{158}Er and a strongly deformed nucleus ^{166}Er. The potential energy scales are all set between -15 to 10 MeV and are cut at $\beta = 0.5$ deformation in order to make visual comparisons between the surfaces easier. The semi-magic nucleus, as expected, shows a reasonably steep potential energy surface with a well-defined spherical minimum ($\beta = 0$, $\gamma = 0$) whilst both other nuclei show strong (prolate) axial deformation ($\gamma = 0$). The transitional case (^{158}Er) clearly indicates that the spherical minimum of this isotopic chain rapidly moves to form a strongly deformed prolate erbium nucleus in the middle of the chain. The depth of the potential well increases as the deformation increases as we approach ^{166}Er where the minimum lies between -12 MeV and -13 MeV. Finally, as we continue along the chain this pronounced prolate deformation remains for several isotopes above ^{166}Er before the depth of the well begins to decrease and the deformation weakens. As the deformation weakens the potential energy surface becomes more flat for small values of β resulting in our calculations showing an oblate minimum for isotopes $^{186-190}$Er before returning to a spherical shape approaching the semi-magic ^{194}Er isotope.

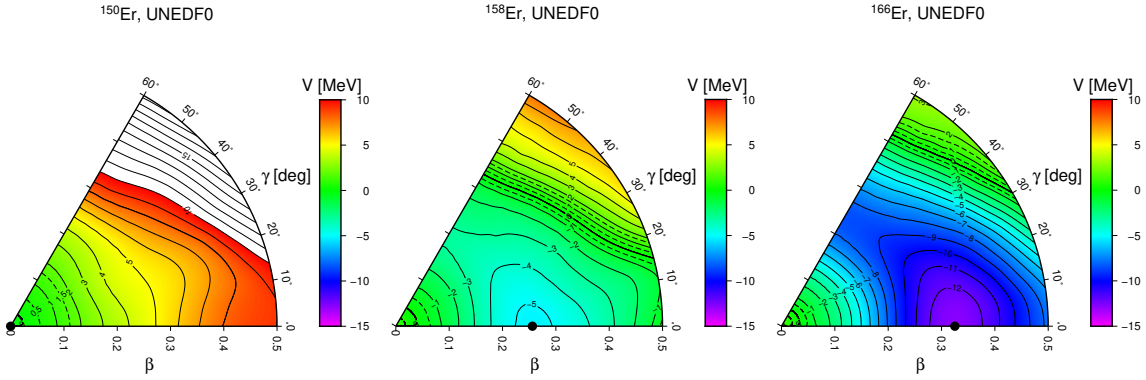

Figure 4.9: (Colour Online) Potential energy surfaces for ^{150}Er (spherical, right), ^{158}Er (transitional, centre) and ^{166}Er (strongly deformed, left) obtained using the UNEDF0 functional.

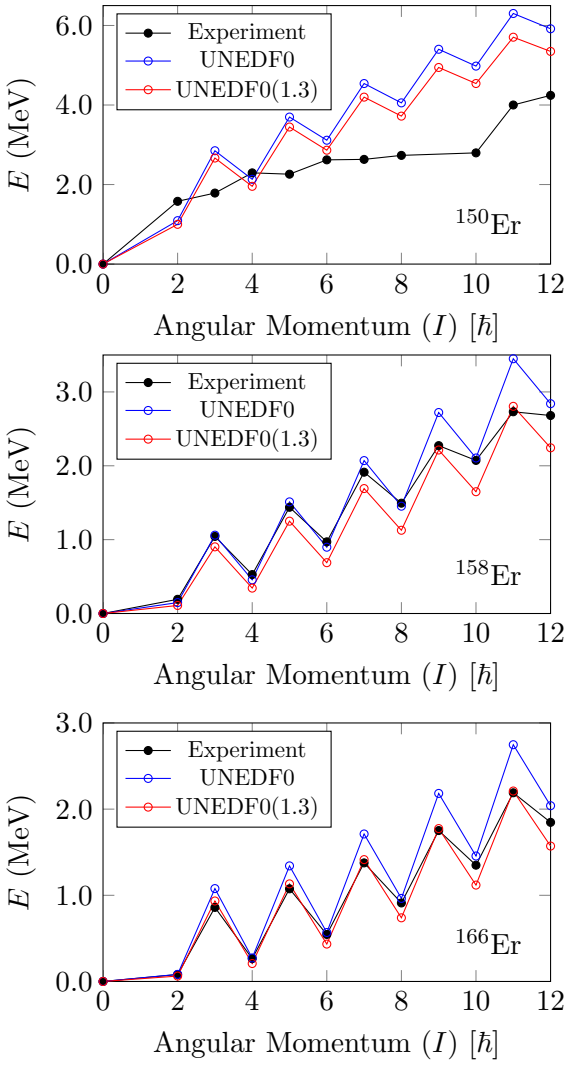

Figure 4.10: (Colour Online) Shows the evolution of the energy spectra expressed in MeV as a function of angular momentum for the low-lying energy states for scaled (red hollow circles) and unscaled (blue hollow circles) UNEDF0 BH calculations. The experimental results [2] are represented by the solid black dots. The results are shown for ^{150}Er (top panel), ^{158}Er (middle panel) and^{166}Er (bottom panel).

From figure 4.10 we can observe for the 3 tests case nuclei the energy spectra plot against angular momentum for the scaled and unscaled BH calculations along with the known experiment. Clearly the theoretical calculations appear completely incorrect for the semi-magic ^{150}Er nucleus. In most BH works significant deviation is noted for semi-magic nuclei in terms of correctly identifying the energy spectra and other observables using the BH. For both ^{158}Er and ^{166}Er we see a much better agreement with experiment. The trends of experiment appear well reproduced with most cases having experiment lie between the scaled and unscaled predictions. As outlined in chapter 3 we see that the difference between the scaled and unscaled calculations increasing for higher angular momentum states implying that by choosing an appropriate scaling, the results can match experiment. However, this notion is incorrect for a couple of reasons. Firstly, from the figures, it is clear that no one scaling best matches all of the states in a given nucleus exactly. Secondly, from the experimental trends it is observed that the trends between states are not uniform indicating, as we expect, that there is likely to be additional physics beyond BH which influences their structure for example, proton-neutron pairing correlations or other exotic

physics out with the scope of BH. Hence, caution should be applied when examining higher angular momentum states using solely BH calculations as it is expected that other physical effects are likely to influence the structure of the states. These effects can include but are not limited to proton-neutron pairing, pairing strengths of the model (in this case the functional pairing strengths), Coriolis terms and signature splitting. Having said this, whilst we restrict our discussion to low-lying energy spectra the trends, are modelled well. Given these calculations are fully triaxial both even and odd angular momentum states are included compared to axial calculations where only even angular momentum states can be considered [6]. The observed staggering arises from signature splitting of rotational bands which is well documented [49] [50] [28] and also documented with regards to collective works of this type in [6]. The signature quantum number is associated with a rotation by π of a deformed nucleus about a principle axis of rotation. The specific action of the rotating system is to lower the energy states of even angular momentum states more than that of odd states. This resultant shift between both bands at a given rotational frequency is referred to as signature splitting and is typically characterised by an energy staggering consistent with the calculated results shown [51]. γ-vibrations (oscillations in the shape of the nucleus, notably in this approach between prolate and oblate shapes) may also impact the structure of the rotational states contributing to the signature splitting effect.

Finally, figure 4.11 compares the low-lying 2_1^+ and 4_1^+ states of the calculations carried out in this study to that of the Gogny D1S functional [3]. Given the different nature of the functional there is no reason why these theoretical calculations should match as they are two distinct nuclear functionals constructed via different methods. However, it is observed that the erbium chain shows a strong overlap, particularly in the deformed region, for describing the low-lying states with either the finite and zero range interactions. Now that this BH systematic study with UNEDF0 has been carried out there exists the possibility for a large scale comparison between the two, ultimately addressing the question: what impact does the choice of functional have on the BH approach? This question will be examined further towards the end of this chapter when a variety of nuclei are calculated using multiple UNEDFs.

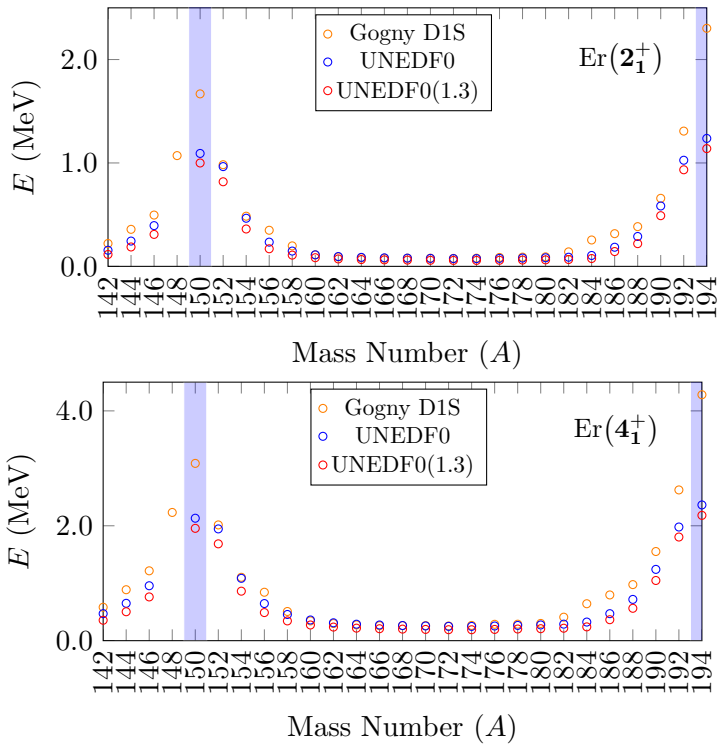

Figure 4.11: (Colour Online) Shows the evolution of the energies expressed in MeV of the first excited 2_1^+ (top panel) and 4_1^+ (bottom panel) states across the erbium isotopic chain for scaled UNEDF0 BH calculations represented by red hollow circles and unscaled UNEDF0 BH calculations represented by blue hollow circles and compare them to the Gogny D1S study [3] results represented by orange hollow circles. The light blue bands highlight the semi-magic nuclei ^{150}Er and ^{194}Er.

This concludes the analysis on this illustrative example of the erbium isotopic chain. Clearly, for quadrupole deformed systems such as erbium, the BH informed with mass parameters calculated systematically from a constrained HFB procedure using UNEDF0 reproduces the trends of experimental observables well. Furthermore, such analysis yields insights regarding the intrinsic deformation of the nucleus and a host of other potential quantities which could be explored in future given the vast array of states and transitions available for further work. Finally, as the database of UNEDF0 BH calculations grows more comparisons to other theoretical techniques and studies can be made to further highlight strengths and weaknesses in all theoretical models.

4.2.2 First excited $E_{2_1^+}$ state

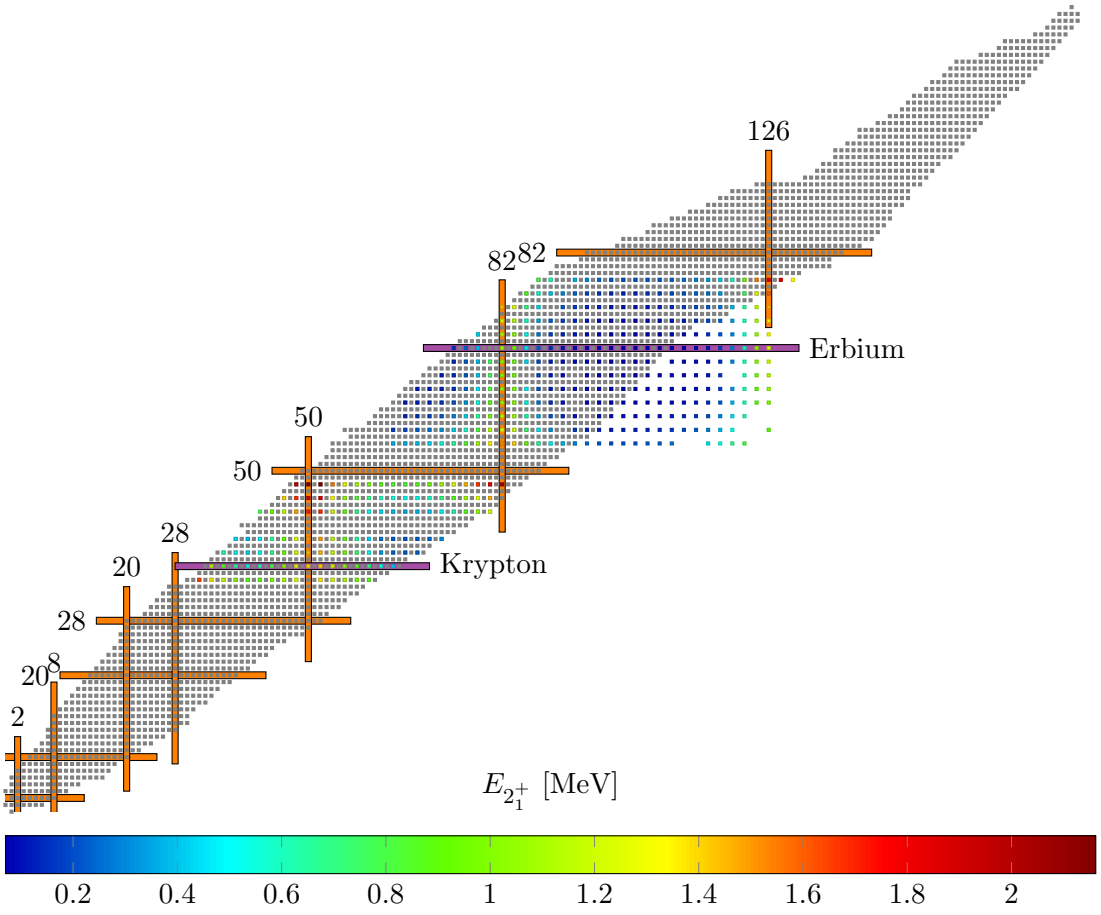

Figure 4.12: 2_1^+ energy spectra for the UNEDF0 BH study.

The low-lying 2_1^+ energy states across the survey region (shown in figure 4.12) agree with the global trends of experimental data. The first excited 2^+ state peaks at the magic numbers whilst rapidly dropping off to a few tens to a few hundred of keV for heavier nuclei. The calculations generally reproduce the energy scale of this state well whilst overestimating the absolute energy of the semi-magic peaks in the experimental data. This isn't surprising given that the unscaled results for several nuclei are overestimated in BH calculations hence, the motivation of many to introduce and fine-tuning via the mass parameter scaling factor. However, the general trends are consistent with experiment. Additionally, it is clear that the energy of this state is generally higher for the lighter nuclei examined in this survey region than in the rare-earth region. Again this is a general trend that broadly speaking is in agreement with experiment where the energy of many nuclei lie in the 500 keV to 1 MeV range.

4.2.3 First excited $E_{4_1^+}$ state

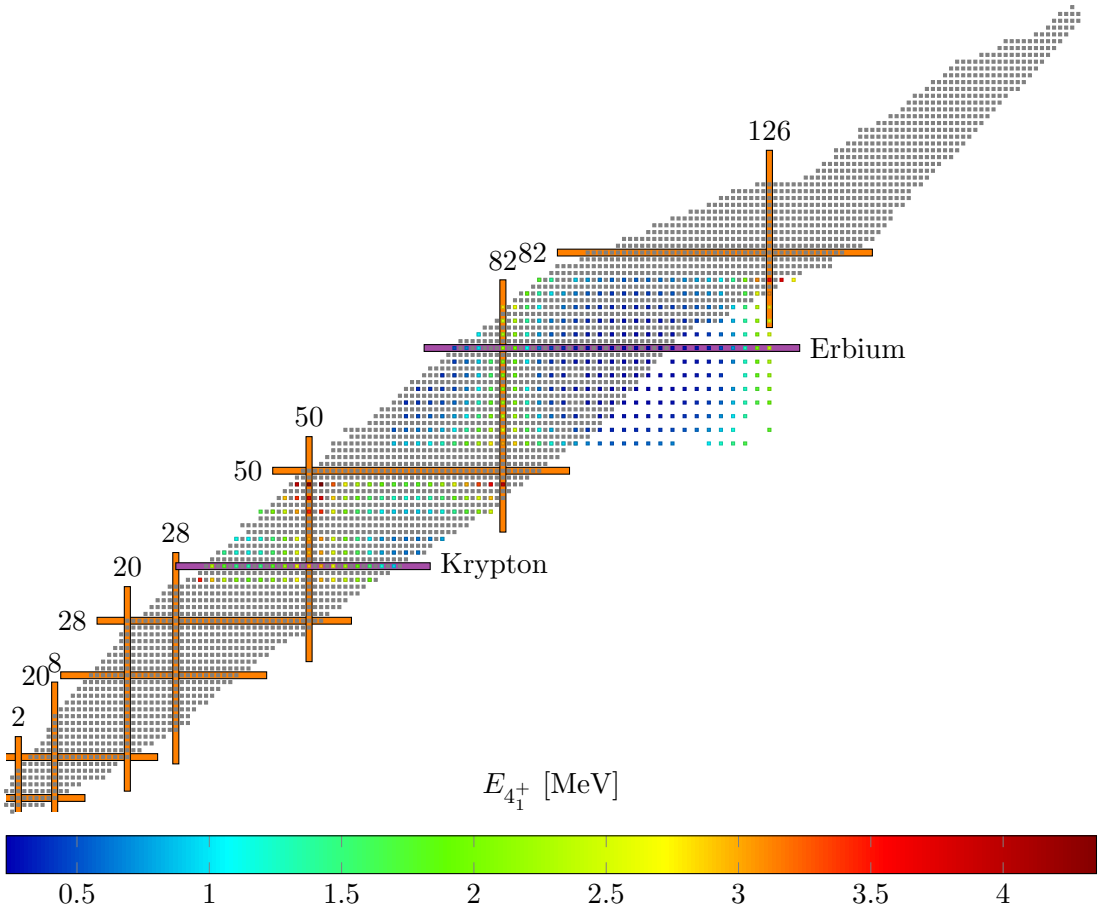

Figure 4.13: 4_1^+ energy spectra for the UNEDF0 BH study.

Figure 4.13 shows the same trends as that of figure 4.12. Again this is consistent with the trends seen from the experimental data. This state lies higher than that of the 2_1^+ state, peaks at magicity and tails off in the rare-earth region away from the magic numbers.

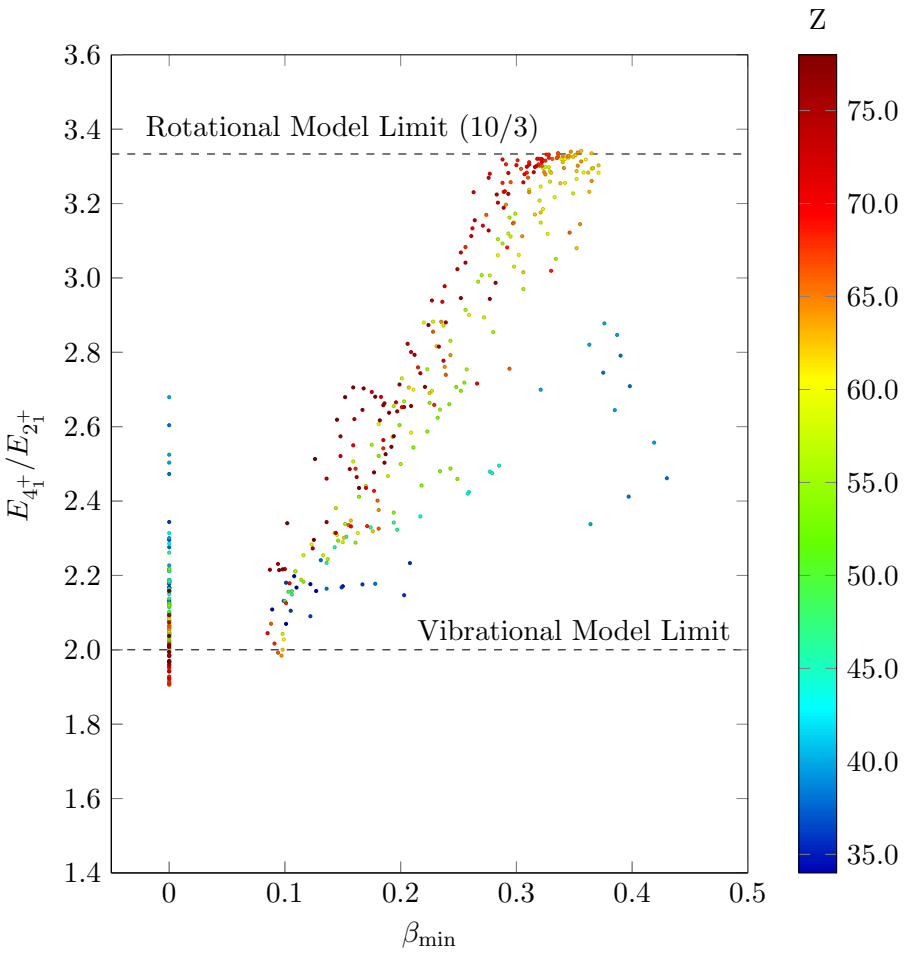

Figure 4.14: $E_{4_1^+}/E_{2_1^+}$ ratio against β_{min} across the nuclear chart for the UNEDF0 BH study.

Figure 4.14 shows the ratio between the energy of the first 4_1^+ and the first 2_1^+ state. As expected there are a number of nuclei from this study which are found to be spherical ($\beta_{\text{min}} = 0$) - predominantly magic and semi-magic nuclei. The remaining nuclei are sandwiched, as expected, between the vibrational model limit (ratio of 2) and the rotational model limit (ratio of 10/3). The microscopic BH calculations for the UNEDF0 functional predict most of these deformed nuclei are a mixture of both vibrational and rotational modes. Hence, if good agreement is obtained between these calculations and experiment then it is reasonable to conclude that these nuclei are described well as ether a pure vibrator, a pure rotator or in the case of the majority, a mix of both. Another general trend that is noted and is in agreement with the Gogny D1S study is that for any given ratio of these two states, the least deformed nuclei (smallest β_{min} value) are those with the largest proton number Z. The most deformed nuclei are nuclei with the lowest Z especially those nuclei located around $Z = 34 - 38$ as calculated within this approach. A more detailed study of the highly deformed low-Z nuclei could be carried out in future publications.

4.2.4 First excited $E_{0_2^+}$ state

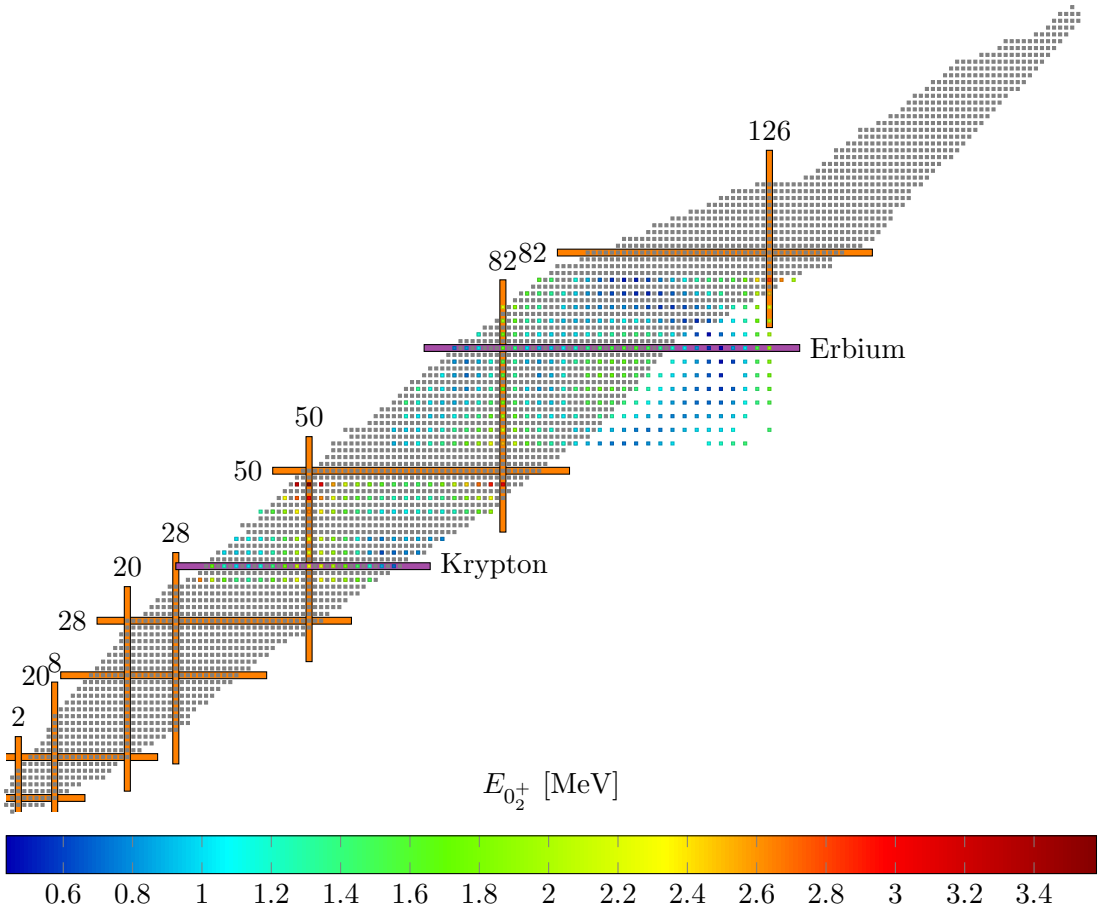

Figure 4.15: 0_2^+ energy spectra for the UNEDF0 BH study.

From figure 4.15 it is observed in the rare-earth region of the study that the behaviour of this state is consistent with the erbium isotopic chain. A peak in this energy state in the rare-earth appears to to occur at semi-magic nuclei and where the deformation of the isotopic chain is strongest. It falls off as before peaking once again in the strongly deformed region (away from magicity) before dropping off and rising as the next magic number (126) is approached. In the lighter region of the systematic survey the drop off of this state is observed as is the peak toward the next magic number however, there is no pronounced peak of the state away from magicity as in the rare-earth region. This may be significant given this region shows less pronounced deformation than that of the rare-earth region. It is important to note that more than being simply another low-lying energy state for comparison in this study, this state and more specifically its electromagnetic transition rates are crucial in addressing the long standing question of β-vibrations in nuclear physics which is in the scope of future work for this research.

4.2.5 $B\left(E2 : 2_1^+ \rightarrow 0_1^+\right)$ reduced transition probabilities

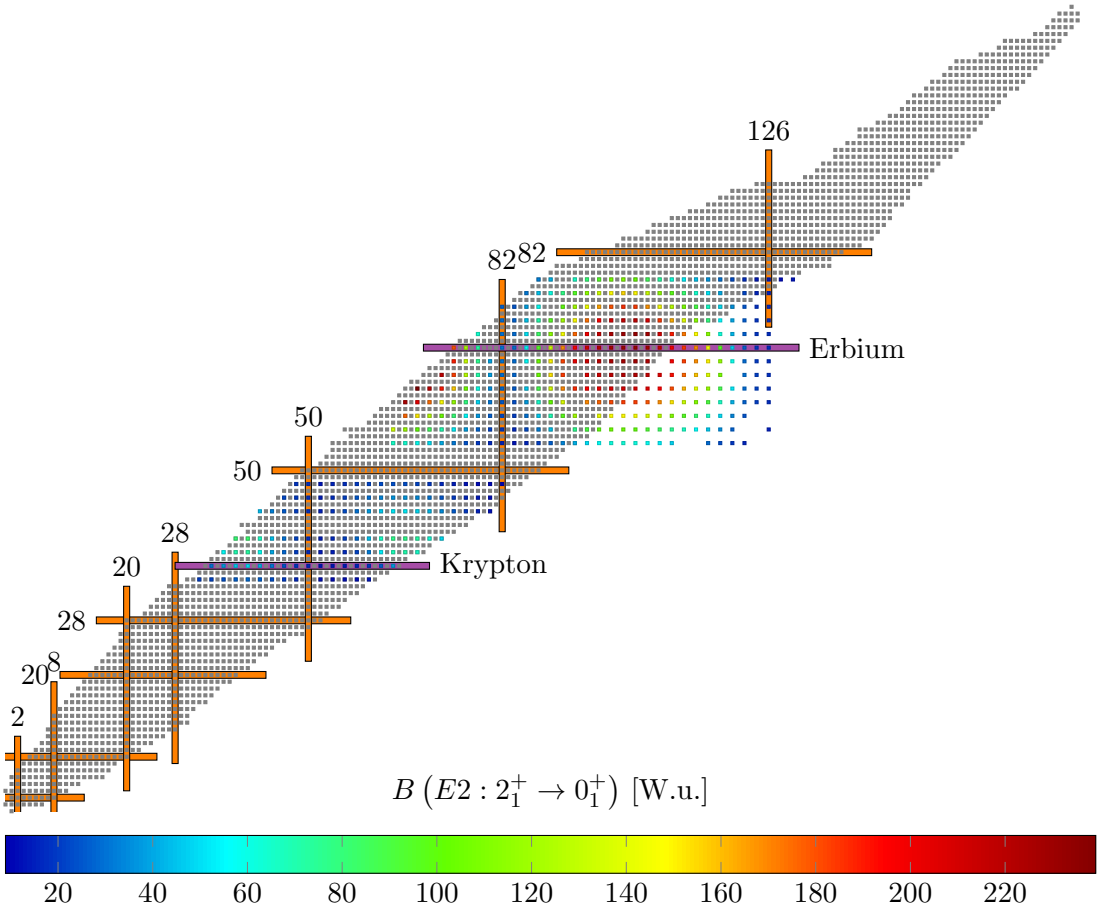

Figure 4.16: Reduced $B\left(E2 : 2_1^+ \rightarrow 0_1^+\right)$ transition rates across the nuclear chart.

Figure 4.16 presents the global trends for the $B\left(E2 : 2_1^+ \rightarrow 0_1^+\right)$ transition rates. From the figure it is clear that there is a strong correlation between strongly deformed nuclei and high transition rates. This $E2$ transition is strongly coupled to quadrupole deformation and so nuclei which exhibit such a strong deformation typically have a large corresponding transition rate as is calculated here. This is precisely what we observed in the erbium chain earlier in figure 4.8. The strength of this transition weakens approaching the magic numbers.

4.2.6 $B\left(E2: 4_1^+ \rightarrow 2_1^+\right)$ reduced transition probabilities

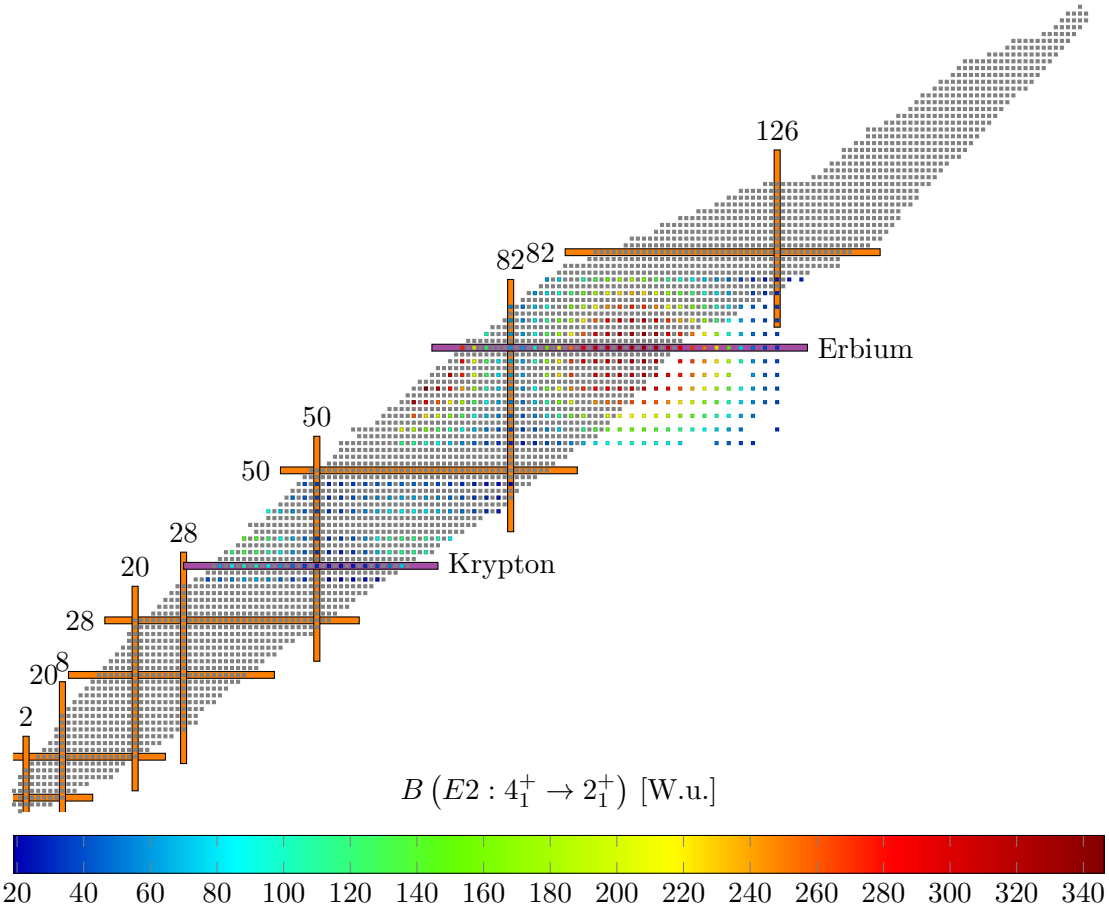

Figure 4.17: Reduced $B\left(E2: 4_1^+ \rightarrow 2_1^+\right)$ transition rates across the nuclear chart.

Figure 4.17 presents the global trends for the $B\left(E2: 4_1^+ \rightarrow 2_1^+\right)$ transition rates. From the figure it is clear again that there is a strong correlation between strongly deformed nuclei and high transition rates. This $E2$ transition is strongly coupled to quadrupole deformation and so nuclei which exhibit such a strong deformation typically have a large corresponding transition rate as is calculated here. These transitions are typically stronger than in the previous figure. The picture here is more complicated however, typically strong quadrupole deformation would give rise to a high transition rate between the 4_1^+ and 2_1^+ states. This was also observed in the erbium chain earlier in figure 4.8. The strength of this transition weakens approaching the magic numbers as well. Given the current lack of experimental data on $E2$ transitions it is hard to make firm conclusions based on these plots but they are presented in an attempt to build support for future nuclear experiments.

4.3 Generalised Bohr Hamiltonian with Various (UNEDF) Functionals

In this section we look at a selection of isotopic chains calculated with a trio of UNEDFs: UNEDF0, UNEDF1 and UNEDF1$_{\mathrm{SO}}$. Given the computational time constraints and the difficulty associated with triaxial convergence it was not possible to cover the entire survey region again for the 3 UNEDF functionals outlined. To this end, selected chains were chosen throughout the survey region and specific examples of these calculations are summarised in this section.

4.3.1 The Krypton Isotopic Chain

The krypton isotopic chain is of much interest to both theorists and experimentalists as it is a light-medium mass isotopic chain which contains ^{72}Kr a proposed candidate along with other light krypton isotopes (such as ^{74}Kr and ^{76}Kr) to be a nucleus exhibiting shape coexistence. Shape coexistence exists when two local minima, both lying in a smooth and relatively flat potential energy surface may provide the opportunity for the nucleus to exist in either minima and potentially oscillate back and forth between the two minima given there is no one clear favourable minimum energy state for the nucleus to exist in.
Following the analysis in [52] we compare the 3 functionals - UNEDF0, UNEDF1 and UNEDF1$_{\mathrm{SO}}$ for the krypton isotopic chain. UNEDF0 are represented by red circles, UNEDF1 by violet squares a UNEDF1$_{\mathrm{SO}}$ by blue triangles.

From figures 4.18 and 4.19 we can observe that the energies of the low-lying energy

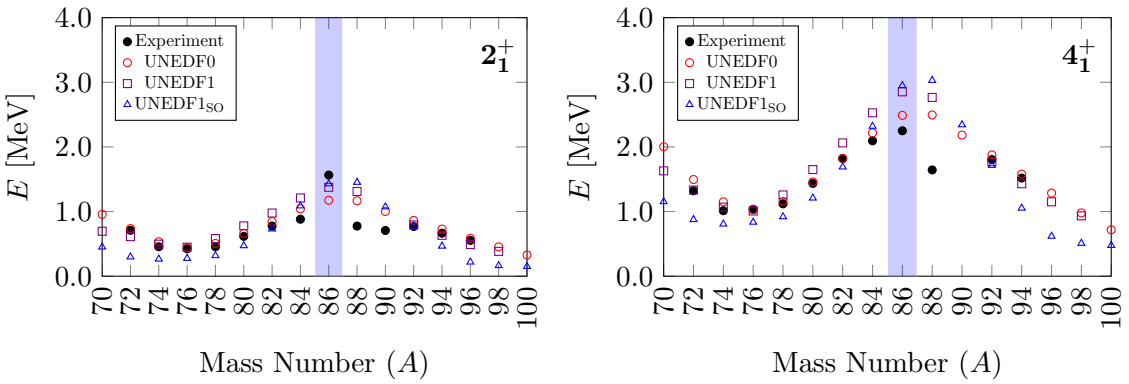

Figure 4.18: (Colour Online) We represent the evolution of the energies expressed in MeV of the first excited 2_1^+ (left panel) and 4_1^+ (right panel) states across the krypton isotopic chain for the 3 functionals: UNEDF0 represented by hollow circles; UNEDF1 represented by hollow squares and UNEDF1$_{\mathrm{SO}}$ represented by hollow triangles and compare them to the experimental results [2] represented by the solid dots. The light blue bands highlight the semi-magic ^{86}Kr nucleus.

spectra are reproduced well. UNEDF0 (and the majority of UNEDF1) are strong fits for the experimental data matching the trend of experimental data across the whole isotopic chain. Again, as expected, we notice a discrepancy for the semi-magic nucleus ^{86}Kr whilst the UNEDF1$_{\mathrm{SO}}$ results are overestimating (or underestimating) the peaks (or the troughs) of the energy spectra. Now we can turn our attention to the electromagnetic transition rates between the low-lying energy states. There is substantially less experimental data for this observable available and the errorbars also provide a larger spread than in the case of the highly accurate measurements of energy spectra. Hence, caution should be applied to examining this observable at this stage. However, all 3 functionals do provide

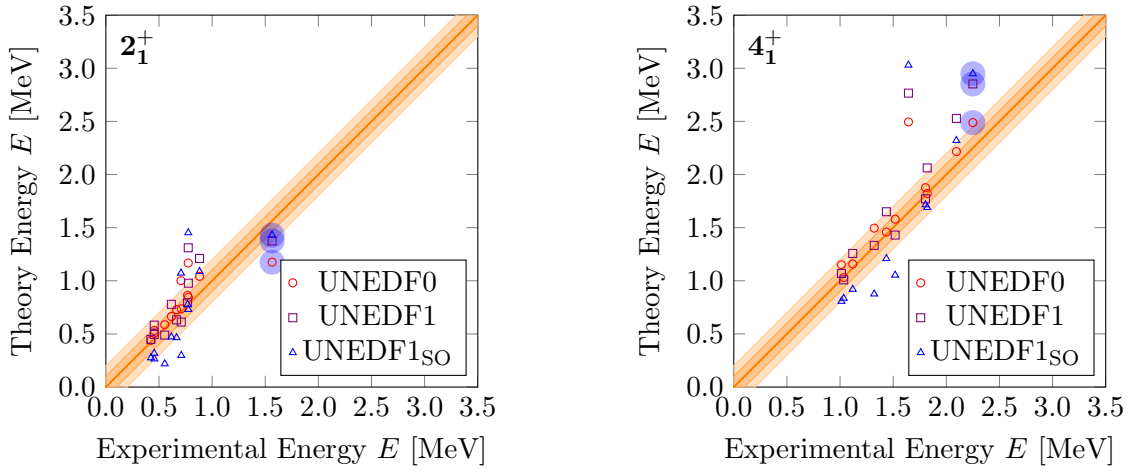

Figure 4.19: (Colour Online) Shows the first 2_1^+ (left panel) and 4_1^+ (right panel) theoretical energy states against the corresponding experimentally measured states [2] for all 3 UNEDF functionals represented by hollow: circles for UNEDF0; squares for UNEDF1 and triangles for UNEDF1$_{SO}$. To guide the eye we add errorbars of ± 100 keV (inner bound) and ± 200 keV (outer bound). Highlighted in large circles are the semi-magic ^{86}Kr nuclei.

peaks and troughs in the correct positions with many of the known experimental errorbars encompassing the theoretical BH calculations. Again, we see strong agreement for the $B\left(E2 : 4_1^+ \to 2_1^+\right)$ rates with UNEDF0 and UNEDF1 whilst noting that UNEDF1$_{SO}$ hits the peaks and troughs almost perfectly whilst lying out with the majority of the experimental errorbars.

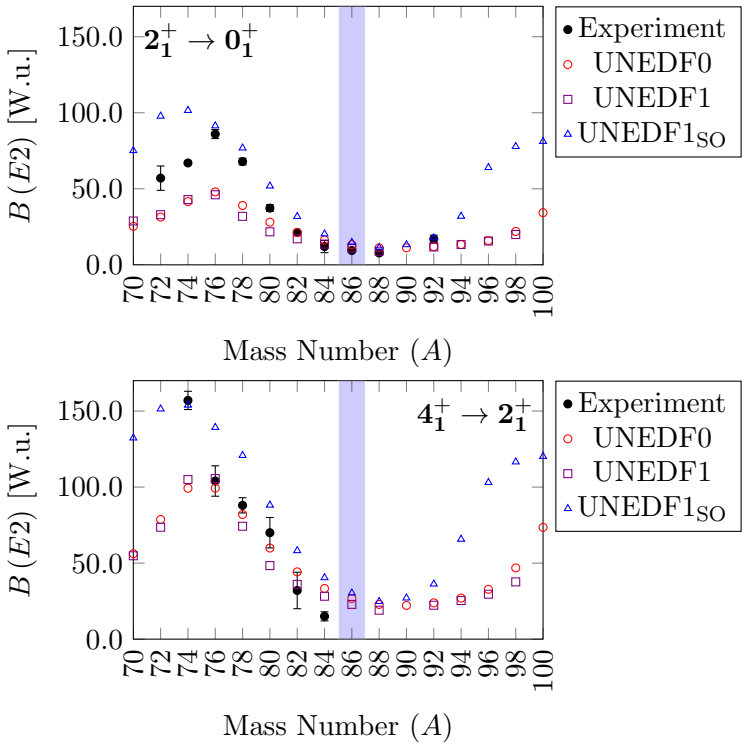

Figure 4.20: (Colour Online) Shows the $B\left(E2 : 2_1^+ \to 0_1^+\right)$ (left panel) and $B\left(E2 : 4_1^+ \to 2_1^+\right)$ (right panel) transition probabilities [2] across the Krypton isotopic chain for the 3 UNEDF functionals represented by hollow circles for UNEDF0; squares for UNEDF1 and triangles for UNEDF1$_{SO}$.

Furthermore, in figure 4.21 we compare the PES for three light krypton isotopes - ^{72}Kr, ^{74}Kr and ^{76}Kr- for the three functionals and observe several competing minima in the potential energy landscape of these nuclei between prolate and oblate shapes. The light krypton isotopes, specifically ^{72}Kr, have been the subject of much discussion in both the experimental and theoretical nuclear physics communities for some time as a potential candidate for shape coexistence. The results presented in this work show an agreement with the current experimental picture in so far as the potential energy surfaces show competing deformed minima which in principle would allow the ground state of the nucleus to oscillate between them, in other words, shape coexistence. To this extent these results are a weak conformation of the shape coexistence phenomenon. It should be pointed out that this work alone is inconclusive as the minima are more pronounced for the UNEDF1 and UNEDF1$_{\mathrm{SO}}$ functionals than for UNEDF0 and thus, are heavily dependent on the functional chosen. A key point that should be made is that these potential energy surfaces are not only relatively flat between the proposed competing minima but are flat and reasonably smooth for most low-lying $\beta\gamma$-deformation points in the deformation plane differing by a few MeV at most. To this end, although several plots may numerically outline various minima the UNEDF calculations indicate the minimum of the potential energy surface may not be well defined and thus, these calculations are not conclusive of the shape coexistence argument.
Finally, we can include a few higher angular momentum states as shown in figure 4.22 showing that the global ordering of the states appears preserved through the 3 UNEDF functionals whilst having different absolute energies of the states dependent on the specific functional used to calculate the microscopic mass parameters. All 3 functionals overestimate the 0_2^+ which is distinct from the current experimental picture where this state actually appears to lie below the 2_1^+ state. In principle, a strong electromagnetic transition from this state to the 2_1^+ would be an indication of β-vibrations which would indicate the nucleus oscillating between different deformations i.e. different minima. Along with possible oscillations in shape (γ-vibrations) these results may or may not support the shape coexistence argument. To this end, a proposed further study of β-vibrations via the aforementioned transition should be carried out globally on all nuclei within this work as a next step.
Overall for a light-medium isotopic chain such as krypton we reproduce the known experimental trends well with Skyrme functionals with UNEDF0 (and UNEDF1) having the strongest agreement with the experimental observables.

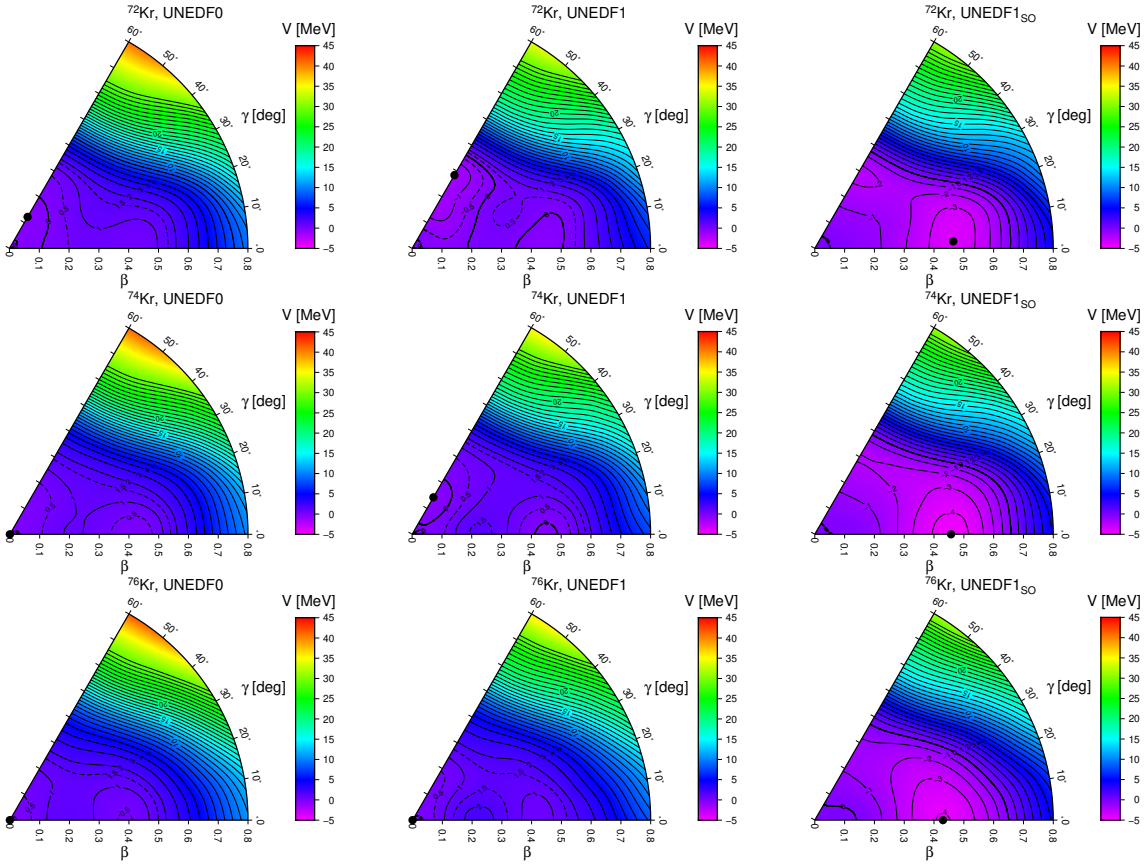

Figure 4.21: (Colour Online) Potential energy surfaces for ^{72}Kr (top row), ^{74}Kr (middle row) and ^{76}Kr (bottom row) obtained using UNEDF0 (left column), UNEDF1 (centre column) and UNEDF1$_{\mathrm{SO}}$ (right column) functionals.

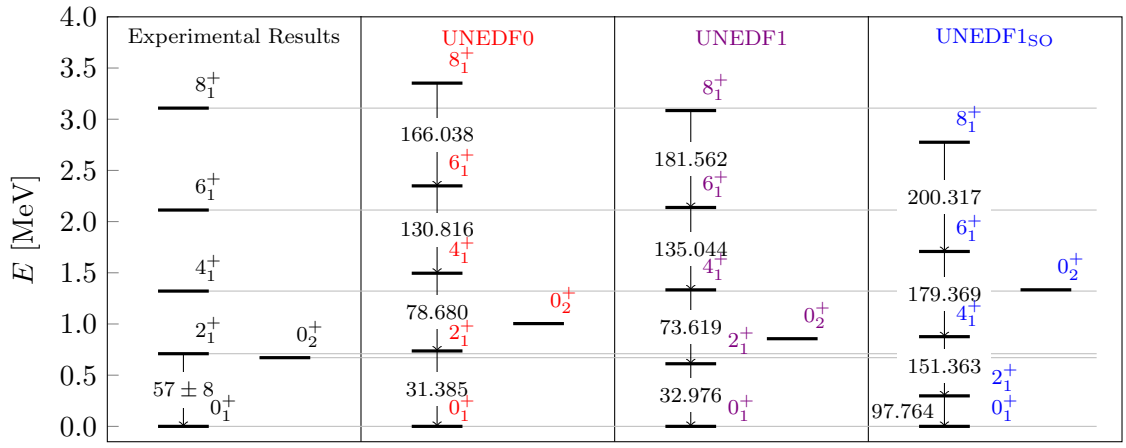

Figure 4.22: (Colour Online) Shows the energy spectra for a number of low-lying states and their associated $B\,(E2)$ transition probabilities for ^{72}Kr where we show the experimental results [2] (far left panel), UNEDF0 (left centre panel), UNEDF1 (right centre panel) and UNEDF1$_{\mathrm{SO}}$ (far right panel).

4.3.2 $N = Z$ Nuclei

In this subsection a discussion of the contribution made to the work of [53] is discussed. Now that we have explored the impact the choice of functional has on such an approach it can be employed in practice to a review of $N = Z$ nuclei. Given recent experimental

efforts as highlighted in the article it is now possible to accurately measure a set of $N = Z$ nuclei believed to exhibit strong collective properties. These nuclei provide an ideal testing ground for various collective nuclear models including the BH. The experimental efforts revealed a staggering in $B\left(E2\right)$ values and hence it was interesting to examine if the 3 UNEDFs used in this work are capable of reproducing the even-even $N = Z$ nuclear trends. From figure 4.23 we can observe that the trends are reasonably well reproduced with UNEDF0 and UNEDF1 both scaled and unscaled follow the general trends whilst UNEDF1$_{\mathrm{SO}}$ tends to overestimate the transition probabilities. It is crucial to note that no functional was able to reproduce the observed staggering and subsequently we conclude that whilst it is possible to model various nuclei with BH there is clearly physics we are not accounting for in this model. This could indicate for example the need for proton-neutron pairing to be included. However, UNEDF0 and UNEDF1 BH calculations are extremely close and typically lie within the experimental errorbars for ^{68}Se, ^{78}Sr (not $N = Z$ but experimental data was obtained too and so is included here) and ^{80}Zr. It is clear that all functionals fail for ^{72}Kr albeit UNEDF0 and UNEDF1 are still closer that UNEDF1$_{\mathrm{S0}}$. Finally, it should be noted that for ^{76}Sr UNEDF1$_{\mathrm{S0}}$ lies within the experimental errorbars. Again this is strong testament to the robustness of the ability of BH to reproduce experimental observables and provide initial theoretical support to nuclear experiment. It is important to highlight that not all functionals converged for all of these nuclei and hence, some points are not shown here. These initial calculations where able to provide an initial guide for further study during the project by my collaborators.

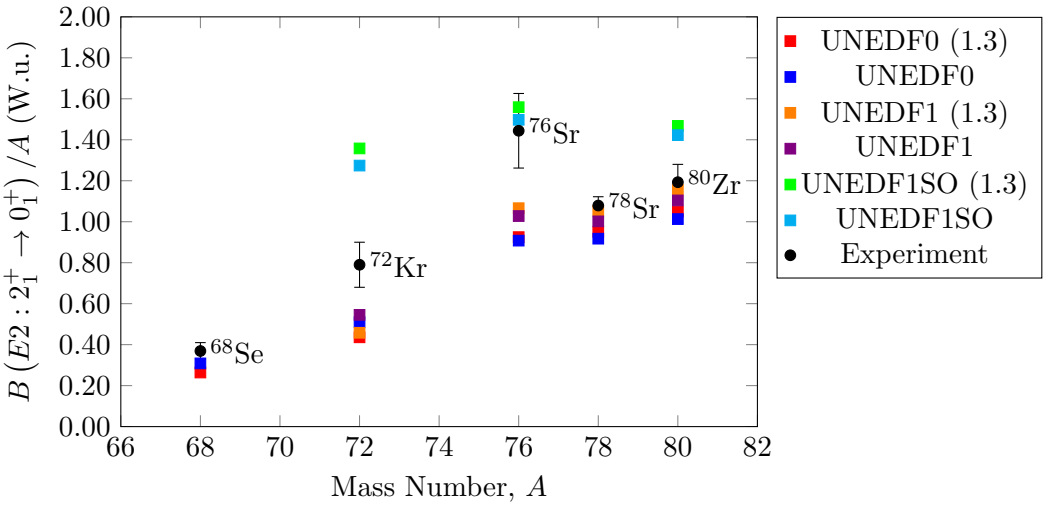

Figure 4.23: (Colour Online) Comparison of the experimental (black dots) and theoretical (coloured squares) $B\left(E2:2_1^+\rightarrow 0_1^+\right)$ transition probabilities in a variety of even-even nuclei requested by experimentalists. Unfortunately, not all functionals converged for all nuclei. Specifically, the ^{68}Se and ^{78}Sr nuclei.

4.3.3 ^{70}Kr and ^{70}Se Work

Supporting theoretical work was done on the mirror nuclei ^{70}Kr and ^{70}Se. Figure 4.24 shows the energy of a number of low-lying angular momentum states. It should be noted that there is little experimental data on the energy states and transition rates in ^{70}Kr. However, there is experimental data known for ^{70}Se. In the case of ^{70}Se it is clear that the low-lying energy states appear to be reproduced very well by the BH calculations carried out on this nucleus, especially by UNEDF1. However, a recurring feature of the current computational approach predicts this staggering between the energy of even and odd angular momentum states to persist to higher states. From the available preliminary experimental results shown in the figure it appears not to be the case. Furthermore, the known experiments to date believe the states shown in the figure to be the correct states but this remains uncertain i.e. NNDC puts the hollow experimental points in brackets as a best guess for the angular momentum of the identified state but with no direct experimental evidence. More experiments will be required to adequately confirm these states. Additionally, as previously noted the reliability of higher angular momentum states from BH calculations should be taken with some caution as there are multiple potential physical effects and phenomena that may affect the structure of these states which is not accounted for in the BH approach. However, confining ourselves to low-lying energy spectra and the known $B\left(E2\right)$ reduced transition probabilities shown in tables 4.1, 4.2, 4.3, 4.4, 4.5 and 4.6, we conclude that the theoretical predications lie close to the experimental values for energy spectra and lie within the known errorbars of the measured transition probabilities. Figure 4.25 shows the potential energy surfaces for 3 UNEDFs for

Table 4.1: ^{70}Kr BH data for UNEDF0.

Quantity	Experiment	UNEDF0	UNEDF0 (TV=1.3)
2_1^+ [MeV]	0.885 [54]	1.0998	0.9561
4_1^+ [MeV]	-	2.3150	2.0035
$B\left(E2:2_1^+\rightarrow 0_1^+\right)$ [W.u.]	-	29.7650	25.3110
$B\left(E2:2_1^+\rightarrow 0_1^+\right)$ [e^{2}fm^4]	-	510.0989	433.7683
$B\left(E2:0_1^+\rightarrow 2_1^+\right)$ [e^{2}fm^4]	2726±451 [54]	2550.4944	2168.8413
$B\left(E2:4_1^+\rightarrow 2_1^+\right)$ [W.u.]	-	66.6860	56.2090
$B\left(E2:4_1^+\rightarrow 2_1^+\right)$ [e^{2}fm^4]	-	1142.8340	963.2840

Table 4.2: ^{70}Kr BH data for UNEDF1.

Quantity	Experiment	UNEDF1	UNEDF1 (TV=1.3)
2_1^+ [MeV]	0.885 [54]	0.8578	0.6955
4_1^+ [MeV]	-	1.9813	1.6300
$B\left(E2:2_1^+\rightarrow 0_1^+\right)$ [W.u.]	-	33.1420	28.8270
$B\left(E2:2_1^+\rightarrow 0_1^+\right)$ [e^{2}fm^4]	-	567.9723	494.0238
$B\left(E2:0_1^+\rightarrow 2_1^+\right)$ [e^{2}fm^4]	2726±451 [54]	2839.8618	2470.1191
$B\left(E2:4_1^+\rightarrow 2_1^+\right)$ [W.u.]	-	64.9990	54.8330
$B\left(E2:4_1^+\rightarrow 2_1^+\right)$ [e^{2}fm^4]	-	1113.9230	939.7027

both mirror nuclei. Clearly from the figure the potential energy surfaces for both nuclei with each functional appear remarkably similar. However, the observables calculated from the BH approach are substantially different and hence an explanation must be sought to where these differences arise from. The most logical suggestion would be the 6 mass parameters calculated in the microscopic calculations which give rise to the differences in

Table 4.3: ^{70}Kr BH data for UNEDF1$_{\mathrm{SO}}$.

Quantity	Experiment	UNEDF1$_{\mathrm{SO}}$	UNEDF1$_{\mathrm{SO}}$ (TV=1.3)
2_1^+ [MeV]	0.885 [54]	0.6172	0.4513
4_1^+ [MeV]	-	1.5449471	1.1537256
$B\left(E2: 2_1^+ \rightarrow 0_1^+\right)$ [W.u.]	-	72.4550	75.12200
$B\left(E2: 2_1^+ \rightarrow 0_1^+\right)$ [e^{2}fm^4]	-	1241.7006	1287.4063
$B\left(E2: 0_1^+ \rightarrow 2_1^+\right)$ [e^{2}fm^4]	2726±451 [54]	6208.5020	6437.0313
$B\left(E2: 4_1^+ \rightarrow 2_1^+\right)$ [W.u.]	-	130.0970	132.3130
$B\left(E2: 4_1^+ \rightarrow 2_1^+\right)$ [e^{2}fm^4]	-	2229.5425	2267.5193

Table 4.4: ^{70}Se BH data for UNEDF0.

Quantity	Experiment	UNEDF0	UNEDF0 (TV=1.3)
2_1^+ [MeV]	0.94452 [2]	1.1576	1.0120
2_1^+ [MeV]	0.954 [54]	1.1576	1.0120
4_1^+ [MeV]	2.03880 [2]	2.3961	2.0905
$B\left(E2: 2_1^+ \rightarrow 0_1^+\right)$ [W.u.]	19.7±13 [2]	23.2740	19.8030
$B\left(E2: 2_1^+ \rightarrow 0_1^+\right)$ [e^{2}fm^4]	-	398.8591	339.3747
$B\left(E2: 0_1^+ \rightarrow 2_1^+\right)$ [e^{2}fm^4]	1659±659 [54]	1994.2955	1696.8735
$B\left(E2: 4_1^+ \rightarrow 2_1^+\right)$ [W.u.]	21.5±18 [2]	53.6170	44.6880
$B\left(E2: 4_1^+ \rightarrow 2_1^+\right)$ [e^{2}fm^4]	-	918.8635	765.8423

the observables which is examined in the subsequent subsection (4.3.4).

4.3.4 Mass Parameters

Figure 4.26 and figure 4.27 show the scaled and unscaled mass parameters for both mirror nuclei for all 6 mass parameters for the UNEDF0 functional. It can be seen that whilst the potential energy surfaces are incredibly similar the differences in the observable values clearly arises from the differences in the mass parameters. In particular, the rotational mass parameters (B_x, B_y, B_z) appear similar in both magnitude and structure of the $\beta\gamma$ landscape between the two mirror nuclei. However, the vibrational mass parameters ($B_{\beta\beta}$, $B_{\beta\gamma}$, $B_{\gamma\gamma}$) have a different structure between the two nuclei especially $B_{\beta\beta}$ and $B_{\gamma\gamma}$. These differences come from the constrained HFB calculations and give rise the the differences in observables specifically the energy spectra and transition rates. This particular work highlights one key feature of this BH survey namely the mass parameters are calculated microscopically in systematic constrained HFB calculations rather than phenomenologically. This is the first systematic survey of this type using UNEDF0 alongside BH and hopefully the automated and adaptable procedure designed over the course of this project will be of much benefit in the future to supporting the experimental nuclear physics community.

Table 4.5: ^{70}Se BH data for UNEDF1.

Quantity	Experiment	UNEDF1	UNEDF1 (TV=1.3)
2_1^+ [MeV]	0.94452 [2]	0.8996	0.7346
2_1^+ [MeV]	0.954 [54]	0.8996	0.7346
4_1^+ [MeV]	2.03880 [2]	2.0453	1.6947
$B\left(E2: 2_1^+ \to 0_1^+\right)$ [W.u.]	19.7±13 [2]	26.6100	23.1700
$B\left(E2: 2_1^+ \to 0_1^+\right)$ [e^{2}fm^4]	-	456.0299	397.0768
$B\left(E2: 0_1^+ \to 2_1^+\right)$ [e^{2}fm^4]	1659±659 [54]	2280.1497	1985.3840
$B\left(E2: 4_1^+ \to 2_1^+\right)$ [W.u.]	21.5±18 [2]	53.1860	44.6570
$B\left(E2: 4_1^+ \to 2_1^+\right)$ [e^{2}fm^4]	-	911.4772	765.3112

Table 4.6: ^{70}Se BH data for UNEDF1$_{\mathrm{SO}}$.

Quantity	Experiment	UNEDF1$_{\mathrm{SO}}$	UNEDF1$_{\mathrm{SO}}$ (TV=1.3)
2_1^+ [MeV]	0.94452 [2]	0.5841	0.4206
2_1^+ [MeV]	0.954 [54]	0.5841	0.4206
4_1^+ [MeV]	2.03880 [2]	1.4817	1.0959
$B\left(E2: 2_1^+ \to 0_1^+\right)$ [W.u.]	19.7±13 [2]	63.1230	66.2040
$B\left(E2: 2_1^+ \to 0_1^+\right)$ [e^{2}fm^4]	-	1081.7730	1134.5737
$B\left(E2: 0_1^+ \to 2_1^+\right)$ [e^{2}fm^4]	1659±659 [54]	5408.8648	5672.8682
$B\left(E2: 4_1^+ \to 2_1^+\right)$ [W.u.]	21.5±18 [2]	112.4250	115.1250
$B\left(E2: 4_1^+ \to 2_1^+\right)$ [e^{2}fm^4]	-	1926.6879	1972.9592

4.3.5 Collective Wavefunctions

This final section of the results presents and briefly describes the probability densities and collective wavefunctions for a selection of nuclei - ^{150}Er (spherical nucleus), ^{158}Er (transitional nucleus), ^{166}Er (strongly deformed nucleus) all obtained with UNEDF0 and ^{72}Kr (shape coexistence candidate) for UNEDF0, UNEDF1 and UNEDF1$_{\mathrm{SO}}$. The collective wavefunctions

$$\Psi^{\mathrm{coll}}_{In_IM}(\beta,\gamma,\Omega) = \sum_{K=0(2),\mathrm{even}} f_{In_IK}(\beta,\gamma)\,\phi^I_{MK}(\Omega)\,, \tag{4.11}$$

are obtained via the diagonalisation of the BH where

$$\phi^I_{MK} = \sqrt{\frac{2I+1}{16\pi^2\,(1+\delta_{I0})}}\left(D^I_{MK} + (-1)^I D^I_{M,-K}\right), \tag{4.12}$$

are normalised combinations of the Wigner D functions. The index n_I is an additional label to number states for a given angular momentum I. The probability density (on the $\beta\gamma$-plane) is obtained by integration of $|\Psi^{\mathrm{coll}}|^2$ over the Euler angles as follows

$$P_{In_I}(\beta,\gamma) = \sum_K |f_{In_IK}(\beta,\gamma)|^2 \sqrt{wr}\beta^4 |\sin(3\gamma)|. \tag{4.13}$$

The same colour scale of the erbium isotopes is used throughout to track the evolution of the probability density and wavefunction components with increasing neutron number for multiple low-lying states (0_1, 0_2, 2_1 and 2_2). The same is true for ^{72}Kr with the 3 different

UNEDFs. Note that there are two components to the two states with angular momentum $I = 2$ compared to only one for the $I = 0$ angular momentum states. Another point to explicitly highlight is that the integral of $P_{In_I}(\beta, \gamma)$ over the $\beta\gamma$-plane should be (and is) equal to 1. One must keep in mind that we integrate $Pd\beta d\gamma$, which differs from the euclidean surface in polar coordinates ($rdrd\phi$). To obtain P we need not only $|f|^2$ but also $\beta^4|\sin(3\gamma)|$ and $\sqrt{wr}$. Hence, there is a strong dependence on β and $P = 0$ for $\gamma = 0, \pi/3$. Also it is crucial to note that when the mass parameters are of the order of 10^2, the value of $\sqrt{wr}$ is of the order 10^5. Hence, the colour scale is not fixed and does not range from 0 - 1. In order to keep the colour scale consistent between nuclei under comparison a scaling of the wavefunction components (by a factor of 4 or 10) had to be incorporated but is displayed on the plots if this has been done. Generally speaking, for the lowest states with a given angular momentum I, the wavefunctions are located close to the minimum of the PES. However, when considering the probability density one must also account for the metric tensor. Given that both states shown with angular momentum $I = 2$ have two components drawing conclusions from a visual inspection of these wavefuctions is risky. These states are included for completeness and allow comparisons to be made between the different nuclei shown for any given state but this discussion is restricted.

The (spherical) ^{150}Er nucleus (shown in figures 4.28 and 4.29) is similar to the harmonic oscillator i.e. a node in the β-direction is observed. The 0_1 and 0_2 states are centred at $\beta = 0$ as expected for a spherical nucleus. Moreover, the 2_1 and 2_2 states have sizeable components for both $K = 0$ and $K = 2$. For the (strongly deformed nucleus) ^{166}Er (shown in figures 4.32 and 4.33) it is observed that for the 2_1 state the $K = 2$ component and for the 2_2 state the $K = 0$ component are both almost zero which is similar to the axial rotor where K is a good quantum number. The ^{158}Er nucleus (shown in figures 4.30 and 4.31) shows a similar structure as ^{166}Er but less flat as would be expected for a transitional nucleus located between the spherical ^{150}Er and strongly deformed ^{166}Er.

Considering the ^{72}Kr nucleus, the wavefunctions are spread over a large portion of the sextant ($\beta \leqslant 0.7$) which arises from the shape of the potential. For both UNEDF0 and UNEDF1 the potential is very flat whilst for UNEDF1$_{\mathrm{SO}}$ the minimum is at a very large β value. Again, as for the erbium isotopes, a scaling of 2 for the wavefunctions has been introduced to attempt to illustrate the structure for the flat distributions whilst keeping the colour scale uniform for ease of comparison. The same general structures are observed in figures 4.34, 4.36 and 4.38 as well as figures 4.35, 4.37 and 4.39 for all 3 functionals. Again the exact positioning and magnitude of the observed maxima and minima depend on the fuctional as we would expect but all indicate the potential for this nucleus to exhibit β-vibrations and potentially shape coexistent. Again, these conclusions are not conclusive and caution should be taken when drawing any firm conclusions from them. Finally, all of the figures listed in this section were calculated again but using the TV scaling factor of 1.3 but no notable changes were observed in these nuclei and so are omitted from this section.

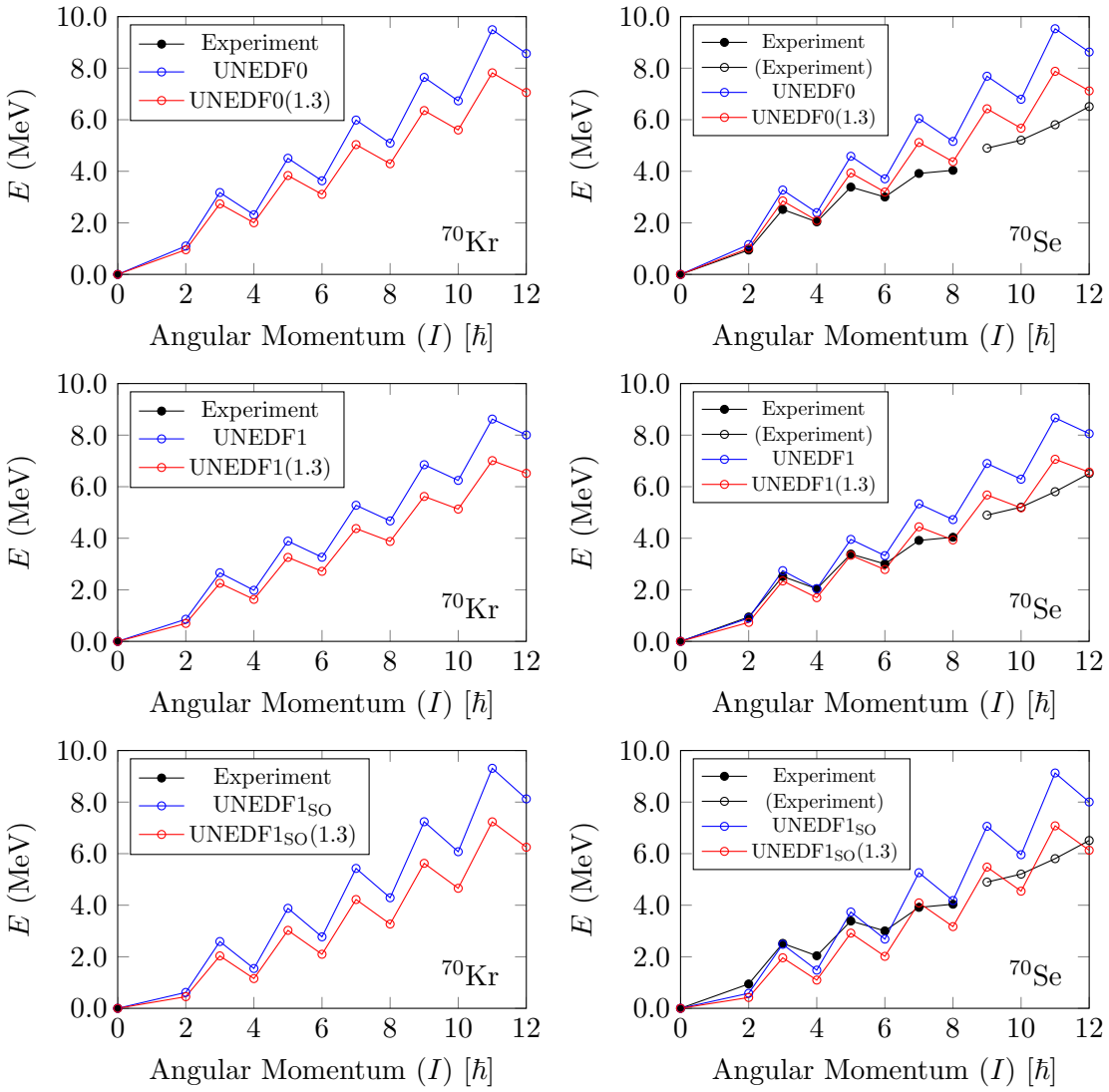

Figure 4.24: (Colour Online) Shows the evolution of the energy spectra expressed in MeV as a function of angular momentum for the low-lying energy states for scaled (red hollow circles) and unscaled (blue hollow circles) UNEDF0 (top row), UNEDF1 (middle row) and UNEDF1$_{\mathrm{SO}}$ (bottom row) BH calculations. The experimental results [2] are represented by the solid black dots whilst states that are uncertain in terms of their angular momentum are marked as hollow black dots. The results are shown for ^{70}Kr (left panels) and ^{70}Se (right panels).

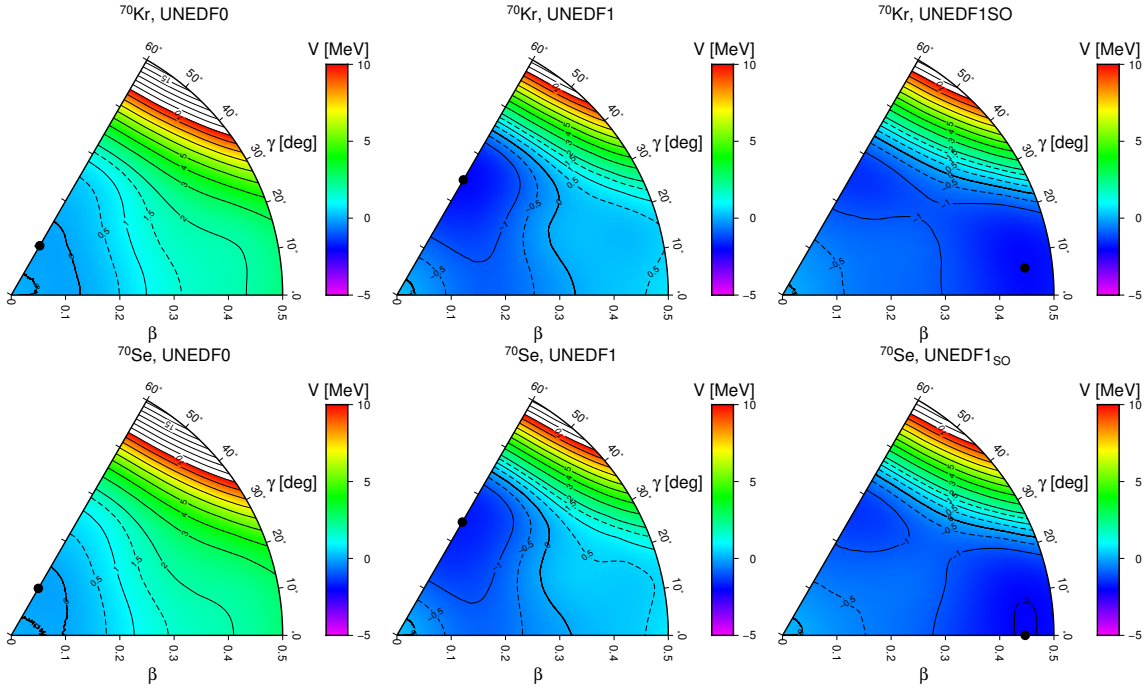

Figure 4.25: (Colour Online) Potential energy surfaces for ^{70}Kr (top row) and ^{70}Se (bottom row) obtained using UNEDF0 (left), UNEDF1 (centre) and UNEDF1$_{SO}$ (right).

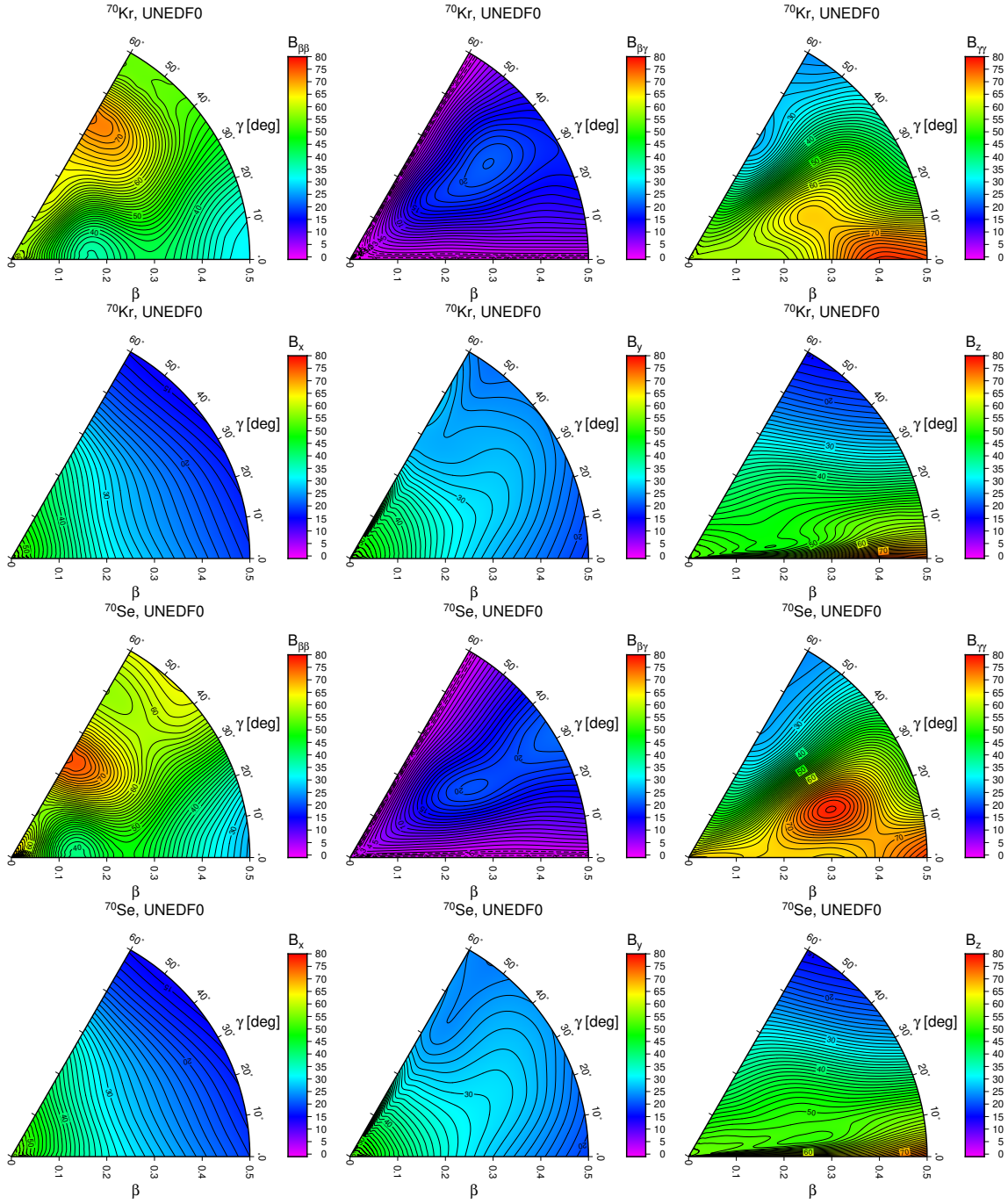

Figure 4.26: (Colour Online) Microscopically calculated mass parameters ($B_{\beta\beta}$, $B_{\beta\gamma}$, $B_{\gamma\gamma}$, B_x, B_y and B_z) for ^{70}Kr (top two rows) and ^{70}Se (bottom two rows) obtained using UNEDF0.

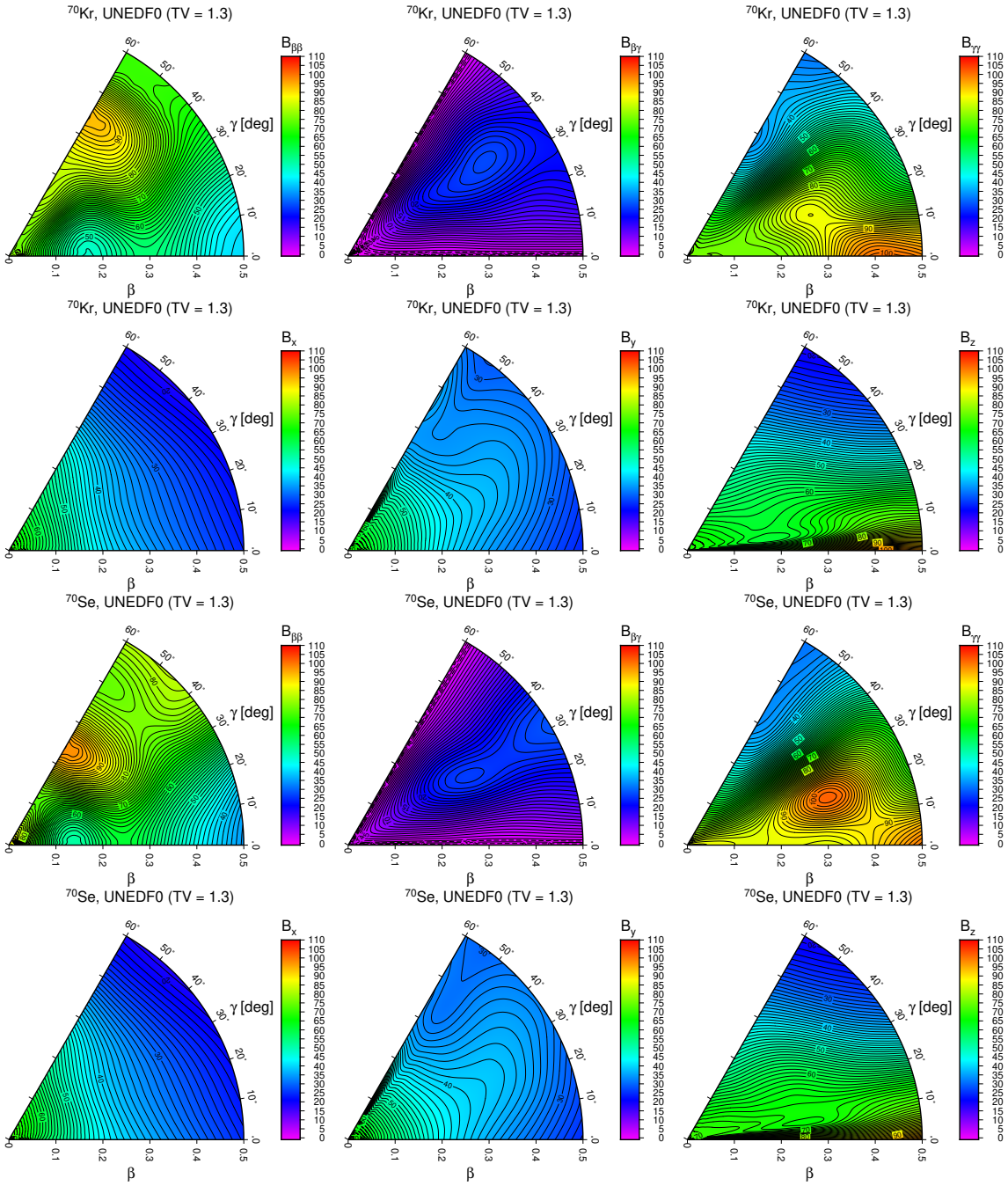

Figure 4.27: (Colour Online) Microscopically calculated mass parameters ($B_{\beta\beta}$, $B_{\beta\gamma}$, $B_{\gamma\gamma}$, B_x, B_y and B_z) for ^{70}Kr (top two rows) and ^{70}Se (bottom two rows) obtained using UNEDF0 with a Thouless-Valatin scaling factor of 1.3 for the mass parameters.

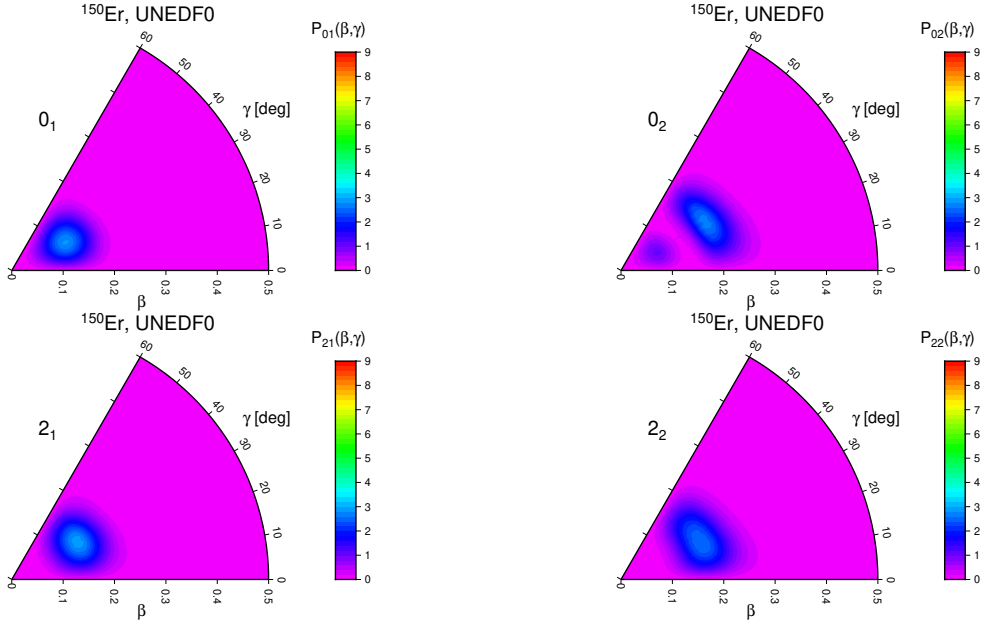

Figure 4.28: (Colour Online) Probability densities for the 0_1, 0_2, 2_1, 2_2 energy states of ^{150}Er obtained using UNEDF0.

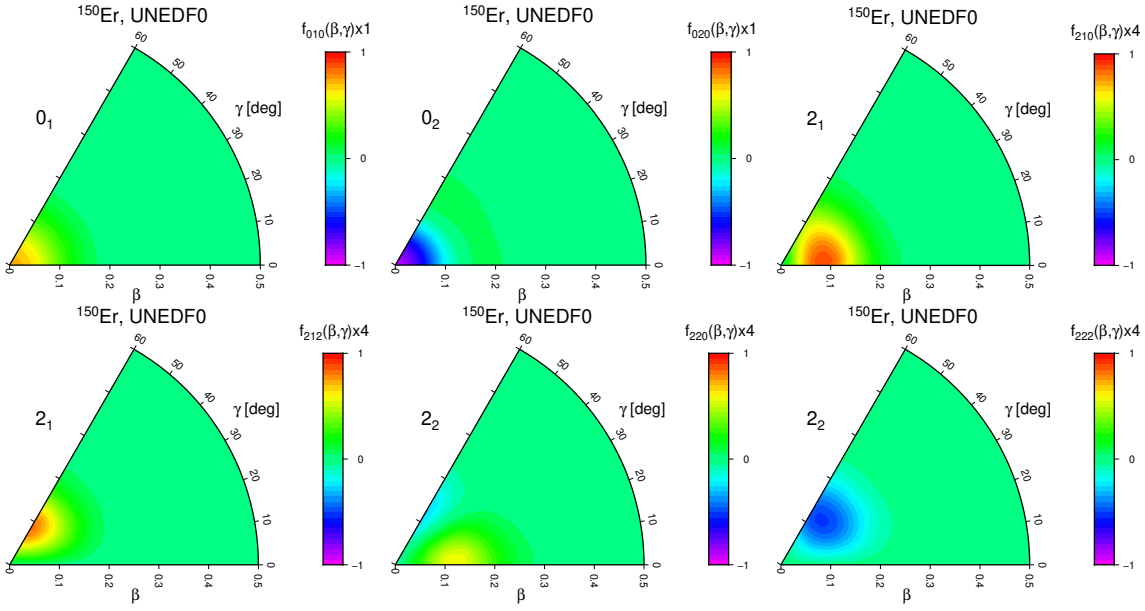

Figure 4.29: (Colour Online) Collective wavefunction components for ^{150}Er obtained using UNEDF0.

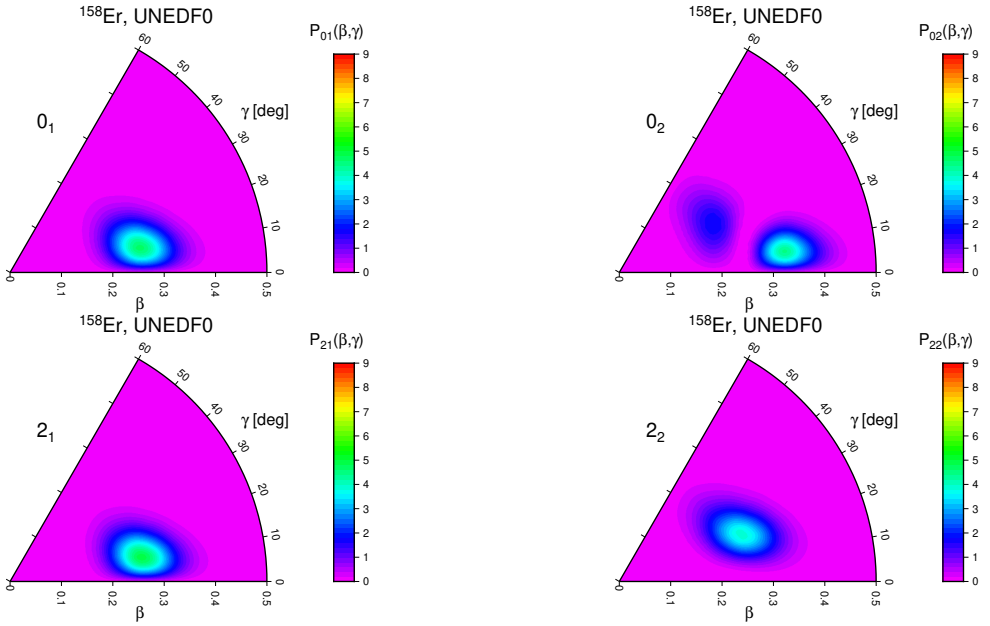

Figure 4.30: (Colour Online) Probability densities for the 0_1, 0_2, 2_1, 2_2 energy states of ^{158}Er obtained using UNEDF0.

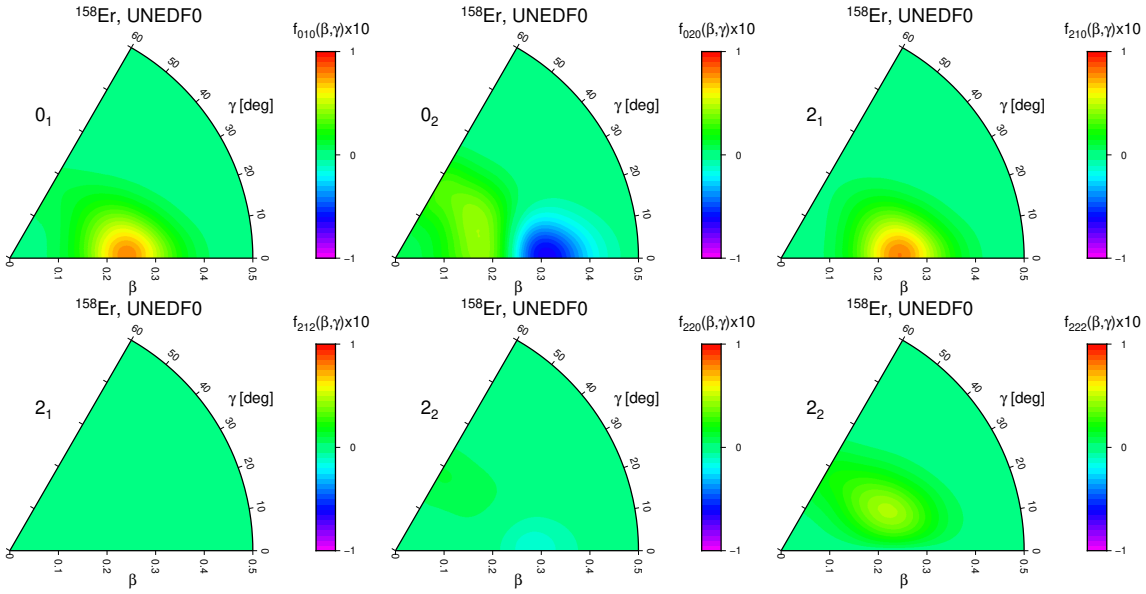

Figure 4.31: (Colour Online) Collective wavefunction components for ^{158}Er obtained using UNEDF0.

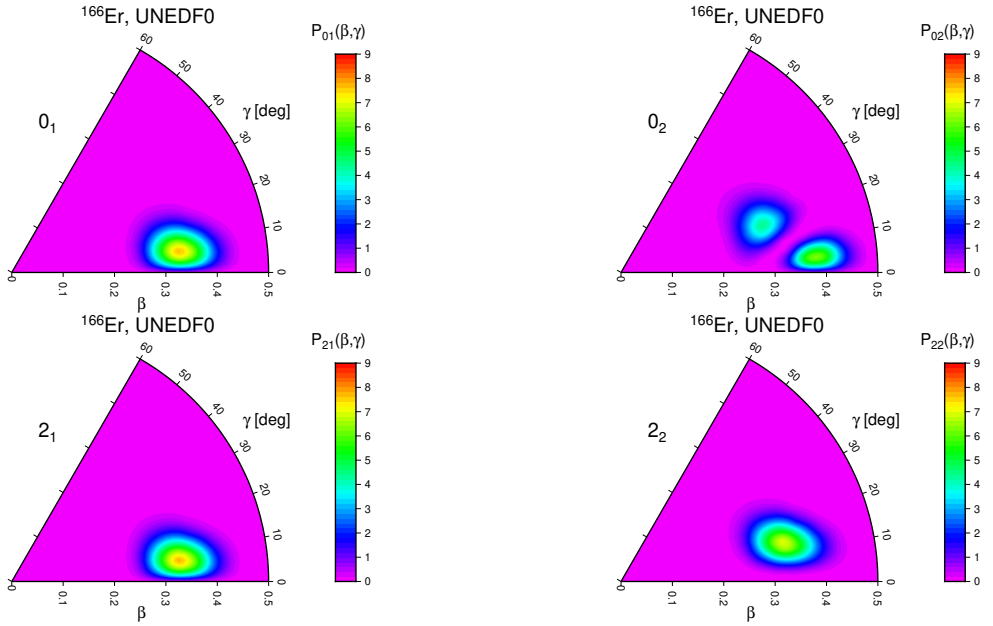

Figure 4.32: (Colour Online) Probability densities for the 0_1, 0_2, 2_1, 2_2 energy states of ^{166}Er obtained using UNEDF0.

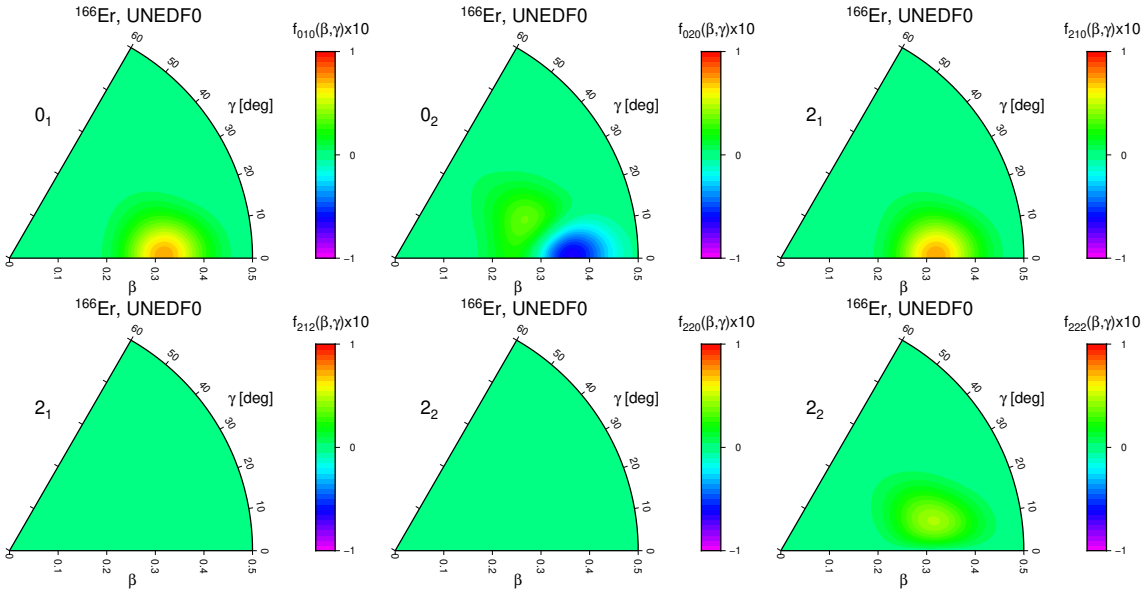

Figure 4.33: (Colour Online) Collective wavefunction components for ^{166}Er obtained using UNEDF0.

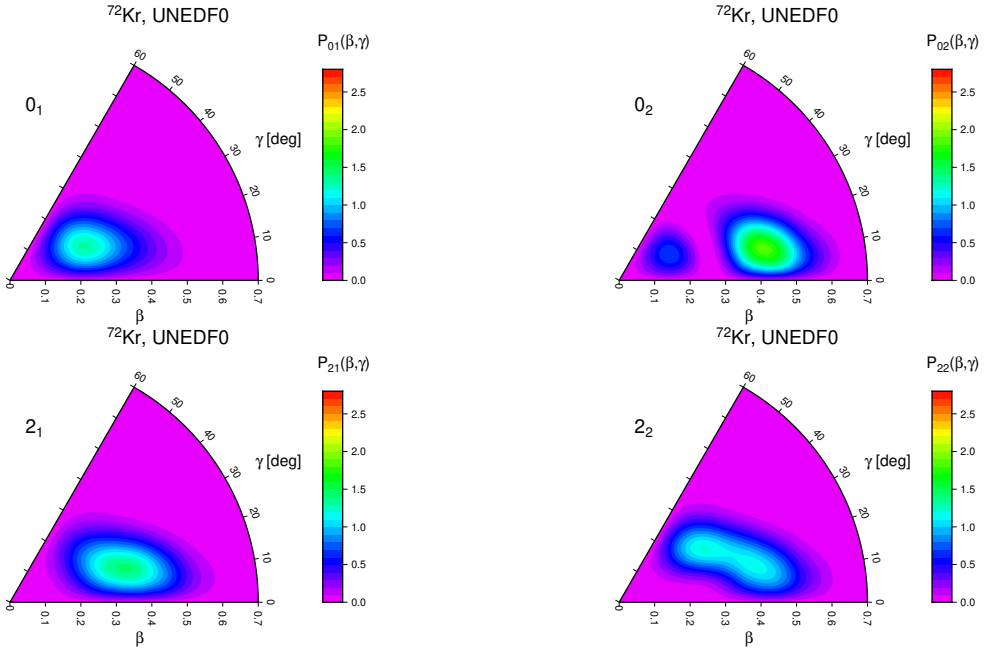

Figure 4.34: (Colour Online) Probability densities for the 0_1, 0_2, 2_1, 2_2 energy states of ^{72}Kr obtained using UNEDF0.

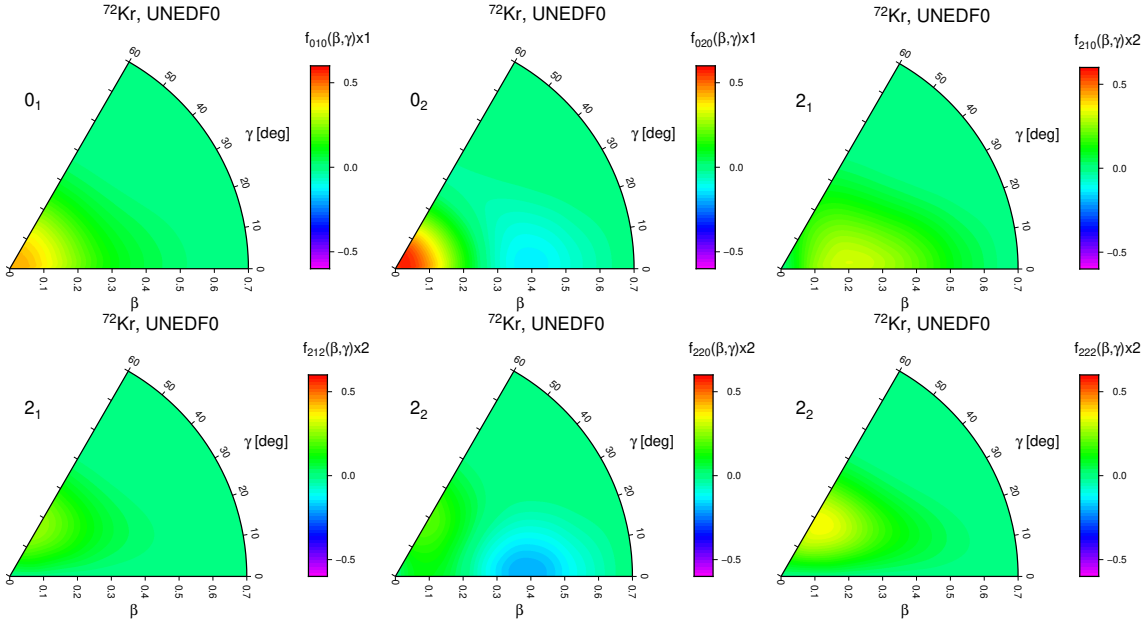

Figure 4.35: (Colour Online) Collective wavefunction components for ^{72}Kr obtained using UNEDF0.

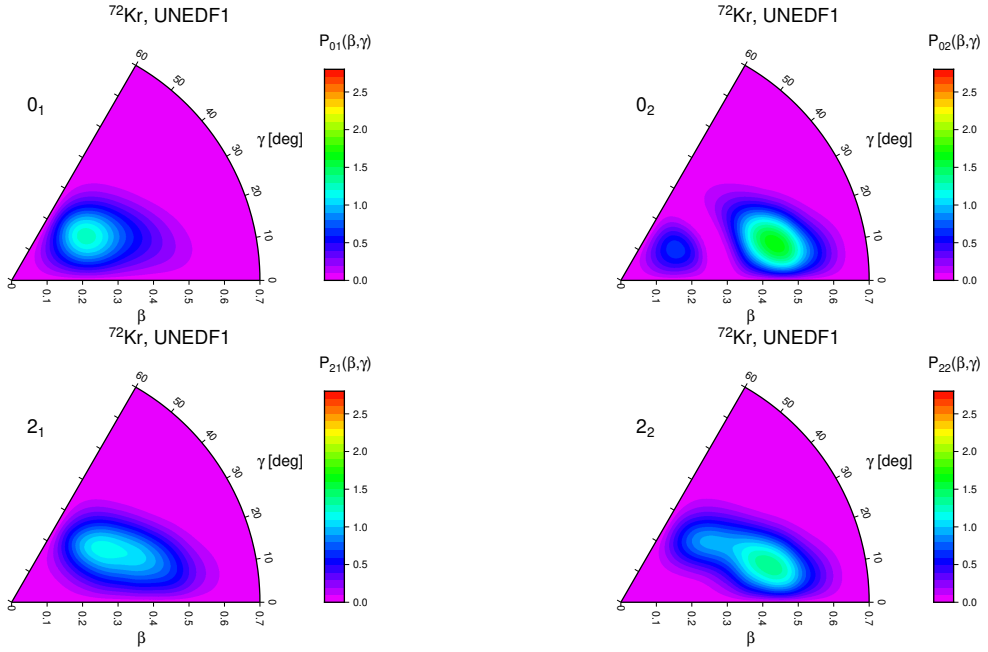

Figure 4.36: (Colour Online) Probability densities for the 0_1, 0_2, 2_1, 2_2 energy states of ^{72}Kr obtained using UNEDF1.

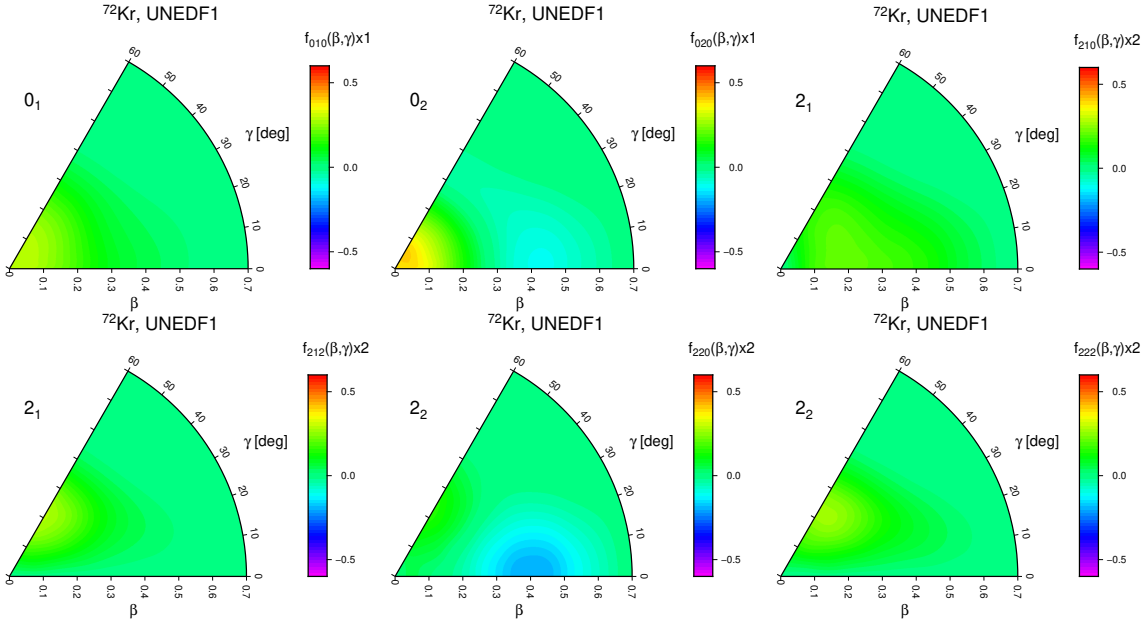

Figure 4.37: (Colour Online) Collective wavefunction components for ^{72}Kr obtained using UNEDF1.

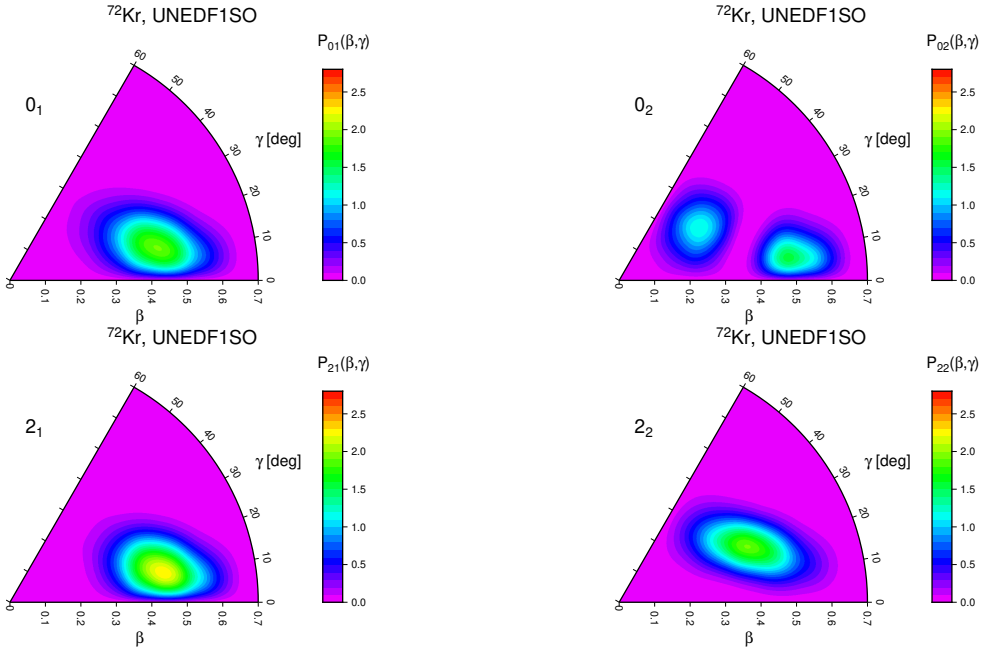

Figure 4.38: (Colour Online) Probability densities for the 0_1, 0_2, 2_1, 2_2 energy states of ^{72}Kr obtained using UNEDF1$_{\mathrm{SO}}$.

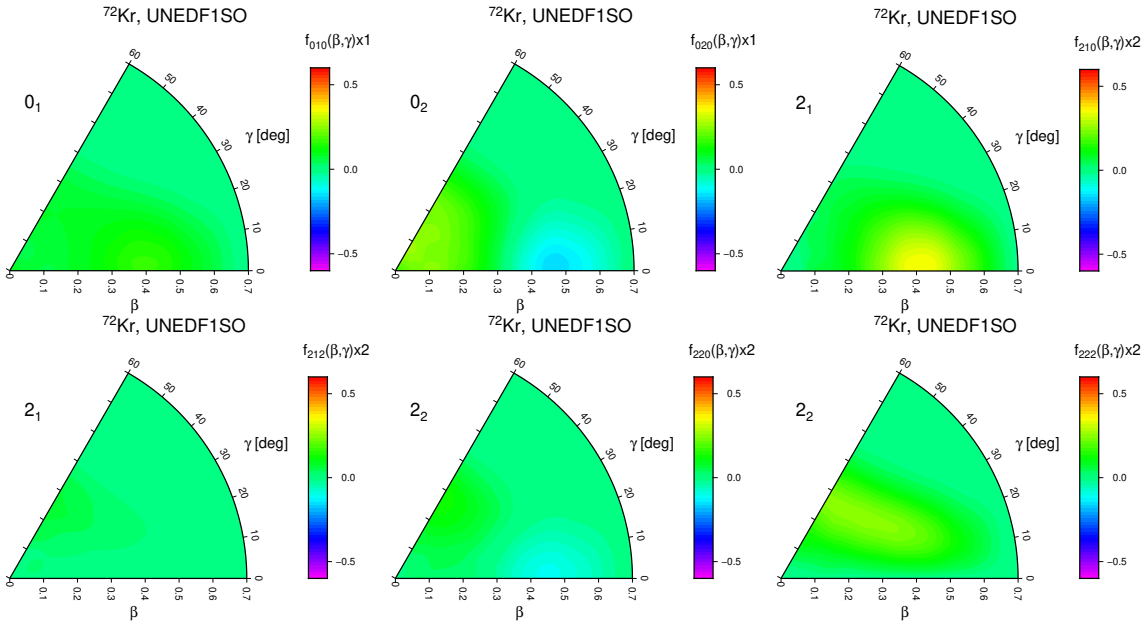

Figure 4.39: (Colour Online) Collective wavefunction components for ^{72}Kr obtained using UNEDF1$_{\mathrm{SO}}$.

Chapter 5

Summary, Conclusions and Future Work

5.1 Summary

To summarise, a large-scale systematic study of even-even nuclei across the medium-to-heavy mass region of the nuclear chart has been performed. This study involves calculating the 6 mass parameters microscopically from constrained HFB calculations implemented with the HFODD code at each $\beta\gamma$-deformation point in the PES and using them within the BH framework to describe low-lying energy spectra and associated reduced transition $B\left(E2\right)$ probabilities systematically across the nuclear chart. This study has applied more stringent convergence criteria to the calculations as well as increasing the number of shells from 12, in previous Skyrme BH works, to 16. Furthermore, a large effort has been put in to converge, fully triaxially, all of the points in the $\beta\gamma$-deformation plane up to and including $\beta = 1.0$ (513 nuclei included in the survey). In particular cases (a further 36 nuclei), some nuclei fail to meet such convergence criteria and are only included provided they converge up to at least $\beta = 0.7$ in order to ensure a strong comparison can be made between theory and experiment. Finally, in the rare-earth region of the chart a region of prediction for nuclei yet to be experimentally observed has been calculated as a theoretical guide to future experiments. The results of this systematic survey are published in an online database (`https://webfiles.york.ac.uk/nuclearBH/`) which will continue to be refined and developed as future work is carried out.

5.2 Conclusions

The UNEDF0 survey within the BH approach shows strong quadrupole deformation ground state properties away from magicity while reproducing spherical ground state properties at the magic numbers as expected. The BH appears to reproduce the trends for both low-lying energy spectra (2_1^+ and 4_1^+) and their associated reduced $B\left(E2\right)$ transition probabilities well. There are discrepancies in and around magic and semi-magic nuclei which is consistent with previous published works as referenced throughout the thesis.
It is noteworthy to highlight that there has been no systematic studies identifying the most fine-tuned set of mass parameter scaling in order to identify the best possible agreement of the approach with experimental observation. Hence, this work calculates both scaled (scaling factor of 1.3) and unscaled BH calculations in the published database as a basis for future work. Nevertheless, throughout this work it is clear that the majority of low-lying states and transition rates are reproduced better with a scaling somewhere within the range of 20% - 40% for the majority of nuclei included in the survey. On the matter of the scaling factor it is important to highlight that this impacts more heavily on

the transition rates than on the low-lying energy spectra and so caution should be applied when comparing both of these observables to experimental observations. Furthermore, there is substantially less experimental data known on the transition rates than on the energy spectra. That said, of what is known and explored in this study for the erbium and krypton isotopic chains along with some additional nuclei of interest, many of the rates lie within the current experimental errorbars which is highly encouraging for future study.
Given the only non-relativistic systematic studies presently conducted are the Gogny D1S [3] and the present work it is difficult to draw firm conclusions regarding the impact that the choice of functional has on the results of the BH framework. For completeness, there has been some systematic work carried out with a relativistic functional which is summarised in [55]. However, given this study with UNEDF0 applied to both the erbium and krypton isotopic chains presented in this work [52], the $N = Z$ nuclei examined [53] and other isotopic chains that are preliminary works in progress conducted throughout this research with UNEDF0, UNEDF1 and UNEDF1$_{\mathrm{SO}}$ along with the Gogny D1S study indicated that the specific interaction has an impact on the potential energy surfaces that are formed from the constrained HFB calculations. From the work on the mirror nuclei ^{70}Kr and ^{70}Se even in cases where the potential energy surfaces appear very similar the (vibrational) mass parameters can be substantially different and give rise to differences in the energy spectra and transition rates emerging form the BH approach. In the majority of cases the structure of the energy spectra of the low-lying states appears preserved under the BH approach. What differs between functionals in all of these cases are the energy of the states rather than the trends of the chains. This implies that with an appropriate choice of functional (and/or scaling) it should be possible to accurately reproduce rotational and vibrational nuclear observables consistent with experiment throughout the chart with this approach. The caution that should be applied here is that we have one Skyrme study and one Gogny study, which provide a strong foundation upon which to build but diversifying the scope of the microscopic calculations to include other functionals will illuminate this question further. Now that a full computational procedure for Skyrme type calculations within this framework exists, these calculations can be carried out at will in the future.
Over the course of this work multiple collaborative efforts have been made to support the experimental community with these calculations and many such collaborations are ongoing. Furthermore, a database of these results has been published and has the potential to continue to grow both in terms of the number of nuclei, the functionals used in the microscopic calculations and the observables and theoretical quantities calculated within the framework. Additionally, there now exists a systematic set of triaxial Skyrme constrained HFB calculations for all nuclei included within the study which is a substantial contribution beyond the standard axial calculations which have been published [56] previously.

5.3 Future Work

Much has been achieved over the duration of this research activity building on the plethora of work that came before it but nonetheless a complete and comprehensive description of both the ground state and excited state properties of all nuclei still needs to be developed. In this section a list of developments and future research work building on the current platform developed over the course of this work is summarised.
Firstly, there is a vast amount of data which has been gathered over the course of this survey including many nuclear states, electromagnetic transition probabilities, potential energy surfaces and many other quantities such as invariants and collective wavefunctions. Additionally, a further range of quantities which could be examined such as pairing

gaps, moments of inertia and their corresponding mass parameters from the constrained HFB calculations are potential areas for further study. Studies and future publications on any/all of these could in principle constitute a vast amount of further work and provide additional tests, and possible refinements, of the Bohr Hamiltonian methodology. The calculations exist and it is an aim to continue to extend the current analysis of these results into the fully published database useful to both the experimental and theoretical communities.

More specific future extensions of this work are wide ranging with varying applicability. Over the course of the project and currently ongoing are multiple collaborative opportunities for providing support to nuclear experiment in terms of both analysis and upcoming experimental proposals. Another extension to this work is to expand the database and corresponding analysis of the BH output results to encompass more nuclei. The first step would be to expand the current procedure to all even-even nuclei across the chart. Following this it would be ideal to construct a robust procedure in dealing with odd and odd-odd nuclei which are currently missing from all collective surveys. Some preliminary work exists in this area but is not robust and is currently unclear as to its reliability. If this can be accomplished then this will be a substantial step forward in nuclear physics as one collective theory can then be applied to the vast majority of nuclei across the nuclear chart. In principle, this could be done but approximating the nucleus as an even-even core (already calculated in my survey) with one (or two) additional quasi-particles. This is typically referred to as core-particle(s)-coupling [57] and provides an exciting avenue for future exploration.

Additionally, there are many remaining open questions surrounding the Bohr Hamiltonian approach. These include the impact the choice of functional has on the result as well as the applicability in using the Bohr Hamiltonian procedure to adjust coupling constants of existing functionals and perhaps even fitting new more comprehensive functionals in future. These can be addressed by running some further tests and reproducing existing results with a host of functionals and comparing them to standard results in the field. These additional calculations will help to grow the database and enrich the landscape of our understanding of deformed nuclei further. This can culminate in a rigorous comparison of numerous methodologies in the field and hopefully yield new insights in the future.

The most challenging yet exciting prospect emerging from this work is the concept of the implementation of a full Adiabatic Time-Dependent Hartree-Fock-Bogoliubov calculation of nuclei which no one has managed before. If successfully implemented it would allow the approach to be calculated with no additional scaling parameters and hopefully should lead to the most accurate collective calculations of all nuclei across the chart from an underlying HFB procedure. The removing of the scaling parameters and incorporating them directly into the theoretical calculation is complex but achievable. Along with collaborators this implementation can be done and would be a substantial achievement in the field of collective excitations of nuclei. Finally, there is relatively little uncertainty study done in nuclear theory given the difficulties inherent in quantifying uncertainties in unconstrained or phenomenological parameters present in most theoretical models. Interestingly, Bayesian statistics may yield an approach to better identify theoretical/model uncertainties [58]. In conjunction with machine learning techniques theoretical calculations should become faster and more accurate and along with this a reasonable uncertainty could be assigned to a whole model or computational procedure. Again, the present Bohr Hamiltonian work provides a suitable testing ground for this idea and it would be a further step in evaluating the robustness of this particular model. Additionally, the covariance matrix is known for UNEDF0 and hence it is possible to carry out error propagation on the functional for a given nucleus as a guide of the associated uncertainty with the constrained HFB calculations conducted in this work as introduced in [59].

Appendix A

Mass Parameters: A More Detailed Look

A.0.1 Mass Parameters in Different Variables

The classical expression for a kinetic energy is given by

$$T = B_{00}\dot{a}_0^2 + 2B_{02}\dot{a}_0\dot{a}_2 + B_{22}\dot{a}_2^2.$$

With (β, γ) deformation coordinates we have

$$\begin{aligned}
a_0 &= X\beta\cos(\gamma) \\
a_2 &= \frac{X}{Y}\beta\sin(\gamma) \\
\Rightarrow \beta\cos(\gamma) &= \frac{a_0}{X} \\
\beta\sin(\gamma) &= \frac{Ya_2}{X} \\
\Rightarrow \frac{\beta\sin(\gamma)}{\beta\cos(\gamma)} &= \tan(\gamma) \\
&= \frac{\frac{Ya_2}{X}}{\frac{a_0}{X}} \\
&= \frac{Ya_2}{a_0} \\
\Rightarrow \gamma &= \tan^{-1}\left(\frac{Ya_2}{a_0}\right).
\end{aligned}$$

Furthermore,

$$\begin{aligned}
\Rightarrow \beta^2\cos^2(\gamma) = \frac{a_0^2}{X^2} \qquad &\text{and} \qquad \beta^2\sin^2(\gamma) = \frac{Y^2a_2^2}{X^2} \\
\Rightarrow \beta^2\left(\cos^2(\gamma) + \sin^2(\gamma)\right) &= \frac{a_0^2}{X^2} + \frac{Y^2a_2^2}{X^2} \\
\Rightarrow \beta^2 &= \frac{a_0^2 + Y^2a_2^2}{X^2} \\
\Rightarrow \beta &= \frac{\sqrt{a_0^2 + Y^2a_2^2}}{X}.
\end{aligned}$$

There are two forms for the expression describing the kinetic energy (both used in various research papers) and are given by

$$T = \tilde{B}_{\beta\beta}\dot{\beta}^2 + 2\tilde{B}_{\beta\gamma}\dot{\beta}\dot{\gamma} + \tilde{B}_{\gamma\gamma}\dot{\gamma}^2$$
$$T = B_{\beta\beta}\dot{\beta}^2 + 2B_{\beta\gamma}\beta\dot{\beta}\dot{\gamma} + B_{\gamma\gamma}\beta^2\dot{\gamma}^2,$$

where

$$\tilde{B}_{\beta\beta} = B_{\beta\beta}, \qquad \tilde{B}_{\beta\gamma} = \beta B_{\beta\gamma}, \qquad \tilde{B}_{\gamma\gamma} = \beta^2 B_{\gamma\gamma}.$$

A.0.2 Expressions for Mass Parameters

Given

$$T = B_{00}\dot{a}_0^2 + 2B_{02}\dot{a}_0\dot{a}_2 + B_{22}\dot{a}_2^2,$$

where the dots denote time derivatives ∂_t, we can construct expressions for the mass parameters based on the matrix associated with the time derivatives of a_0 and a_2 or of β and γ. To begin, let us calculate the time derivatives of a_0 and of a_2 as follows

$$\dot{a}_0 = X\dot{\beta}\cos(\gamma) - X\beta\sin(\gamma)\dot{\gamma}$$
$$\dot{a}_2 = \frac{X}{Y}\dot{\beta}\sin(\gamma) + \frac{X}{Y}\beta\cos(\gamma)\dot{\gamma}.$$

So, we can construct the expression for T (given above) and compare it to the coefficients in the other forms of T as follows

$$\begin{aligned}
T = {} & B_{00}\left(X^2\dot{\beta}^2\cos^2(\gamma) - 2X^2\beta\dot{\beta}\dot{\gamma}\sin(\gamma)\cos(\gamma) + X^2\beta^2\sin^2(\gamma)\dot{\gamma}^2\right) \\
& + 2B_{02}\left(\frac{X^2}{Y}\dot{\beta}^2\sin(\gamma)\cos(\gamma) + \frac{X^2}{Y}\beta\dot{\beta}\dot{\gamma}\cos^2(\gamma) - \frac{X^2}{Y}\beta\dot{\beta}\dot{\gamma}\sin^2(\gamma) - \dot{\gamma}^2\frac{X^2}{Y}\beta^2\sin(\gamma)\cos(\gamma)\right) \\
& + B_{22}\left(\frac{X^2}{Y^2}\dot{\beta}^2\sin^2(\gamma) + 2\frac{X^2}{Y^2}\beta\dot{\beta}\dot{\gamma}\sin(\gamma)\cos(\gamma) + \frac{X^2}{Y^2}\dot{\gamma}^2\beta^2\cos^2(\gamma)\right).
\end{aligned}$$

Now either by matrix transformation or by collecting like terms of $\dot{\beta}^2$, $\dot{\beta}\dot{\gamma}$ and $\dot{\gamma}^2$ we obtain

$$\begin{aligned}
\tilde{B}_{\beta\beta} &= X^2\left(B_{00}\cos^2(\gamma) + 2\frac{1}{Y}B_{02}\cos(\gamma)\sin(\gamma) + B_{22}\frac{1}{Y^2}\sin^2(\gamma)\right) \\
\tilde{B}_{\beta\gamma} &= X^2\left(-B_{00}\beta\cos(\gamma)\sin(\gamma) + \frac{1}{Y}B_{02}\beta\left(\cos^2(\gamma) - \sin^2(\gamma)\right) + \frac{1}{Y^2}B_{22}\beta\cos(\gamma)\sin(\gamma)\right) \\
\tilde{B}_{\gamma\gamma} &= X^2\left(B_{00}\beta^2\sin^2(\gamma) - 2\frac{1}{Y}B_{02}\beta^2\cos(\gamma)\sin(\gamma) + B_{22}\frac{1}{Y^2}\beta^2\cos^2(\gamma)\right).
\end{aligned}$$

By using the above substitution we can write

$$\begin{aligned}
\tilde{B}_{\beta\beta} &= X^2\left(B_{00}\cos^2(\gamma) + 2\frac{1}{Y}B_{02}\cos(\gamma)\sin(\gamma) + B_{22}\frac{1}{Y^2}\sin^2(\gamma)\right) \\
\tilde{B}_{\beta\gamma} &= X^2\left(-B_{00}\cos(\gamma)\sin(\gamma) + \frac{1}{Y}B_{02}\left(\cos^2(\gamma) - \sin^2(\gamma)\right) + \frac{1}{Y^2}B_{22}\cos(\gamma)\sin(\gamma)\right) \\
\tilde{B}_{\gamma\gamma} &= X^2\left(B_{00}\sin^2(\gamma) - 2\frac{1}{Y}B_{02}\cos(\gamma)\sin(\gamma) + B_{22}\frac{1}{Y^2}\cos^2(\gamma)\right),
\end{aligned}$$

and this is the notation used in all publications by Leszek Próchniak.

A.0.3 Moments of Inertia from Mass Parameters

In this subsection we consider how to calculate the mass parameters B_k from the moments of inertia I_k. Simply put, we know that the moments of inertia are given by

$$I_k = 4B_k\beta^2 \sin^2\left(\gamma - \frac{2k\pi}{3}\right).$$

Obviously rearranging the above expression attempts to answer the question but problems can arise when β and/or $\sin^2\left(\gamma - \frac{2k\pi}{3}\right)$ are very small. The solution to such a problem is based on the known symmetry properties which follow.

1. If $\beta < \epsilon_\beta$

$$B_k = B_{\gamma\gamma}.$$

2. If $|\gamma| < \epsilon_\gamma$

$$\begin{aligned} B_z &= B_{\gamma\gamma} \\ B_k &= \frac{I_k}{4\beta^2 \sin^2\left(\gamma - \frac{2k\pi}{3}\right)}, \quad k = 1,\ 2. \end{aligned}$$

3. If $|\gamma - \pi/3| < \epsilon_\gamma$

$$\begin{aligned} B_y &= B_{\gamma\gamma} \\ B_k &= \frac{I_k}{4\beta^2 \sin^2\left(\gamma - \frac{2k\pi}{3}\right)}, \quad k = 1,\ 3. \end{aligned}$$

4. Otherwise

$$B_k = \frac{I_k}{4\beta^2 \sin^2\left(\gamma - \frac{2k\pi}{3}\right)}, \quad k = 1,\ 2, 3.$$

Appendix B

The Metric Tensor

An element of length ds^2 on a Riemannian manifold is defined by a set of local coordinates $\{\xi^\sigma\}$ as follows

$$ds^2 = \sum_{\sigma\tau} g_{\sigma\tau} d\xi^\sigma d\xi^\tau,$$

where $g_{\sigma\tau}$ is a component of the metric tensor.
Given that the collective model space, $\mathbb{R}^5$, and its 4-sphere sub-manifold S_4 are examples of a Euclidean space (or a sub-manifold of a Euclidean space) then there are multiple simplifications which can be made given that the underlying Euclidean space is flat. Thus, the length element can be defined in terms of Cartesian coordinates $\{x_i\}$ by

$$ds^2 \equiv \sum_i dx_i.$$

$$g_{\sigma\tau} = \sum_i \frac{\partial x_i}{\partial \xi^\sigma} \frac{\partial x_i}{\partial \xi^\tau}.$$

Furthermore, given that

$$\sum_i \frac{\partial x_i}{\partial \xi^\sigma} \frac{\partial \xi^\tau}{\partial x_i} = \delta_{\sigma\tau},$$

we can express the inverse $\overline{g}$ of the metric tensor which has matrix elements given by

$$\overline{g}^{\sigma\tau} = \sum_i \frac{\partial \xi^\sigma}{\partial x_i} \frac{\partial \xi^\tau}{\partial x_i}.$$

When constructing a coordinate system such as this we require a volume element dV and a Laplacian in terms of the new coordinates. Both of these can be obtained via the Jacobian as follows

$$\begin{aligned} dV &= d^n x \quad \text{for an } n\text{-dimensional Euclidean space} \\ &= \prod_i dx_i. \end{aligned}$$

In this case we are dealing with a 5-dimensional Euclidean space and wish to express it in arbitrary curvilinear coordinates as follows

$$dV = J d^5\xi \equiv J \prod_\sigma d\xi^\sigma,$$

where J is the Jacobian associated with the transformation $\{dx_i\} \to \{d\xi^\sigma\}$ from the standard Cartesian coordinates to arbitrary curvilinear coordinates and is the determinant of the matrix $\{\partial x_i / \partial \xi^\sigma\}$. It follows that

$$J = \sqrt{\det(g)}.$$

Appendix C

The Laplace-Beltrami Operator

Given that we can define the Laplacian operator $\nabla^2 = \boldsymbol{\nabla} \cdot \boldsymbol{\nabla}$ on a real Euclidean space in terms of Cartesian coordinates as follows

$$\nabla^2 = \sum_i \frac{\partial^2}{\partial x_i^2}$$

and that we can expand the partial derivative operator $\partial/\partial x_i$ in terms of arbitrary (curvilinear) coordinates by

$$\frac{\partial}{\partial x_i} = \sum_\lambda \frac{\partial \xi^\lambda}{\partial x_i} \frac{\partial}{\partial \xi^\lambda},$$

we can construct the Laplacian in arbitrary curvilinear coordinates with the following argument.
We utilise the metric tensor (specifically its inverse) in order to write the above Cartesian coordinate derivative solely in terms of arbitrary coordinates and subsequently use the definition of a matrix element in order to express the Laplacian in the form of arbitrary coordinates. Hence,

$$g_{\kappa\lambda} = \sum_i \frac{\partial x_i}{\partial \xi^\kappa} \frac{\partial x_i}{\partial \xi^\lambda} \qquad \text{and} \qquad \overline{g}^{\kappa\lambda} = \sum_i \frac{\partial \xi^\kappa}{\partial x_i} \frac{\partial \xi^\lambda}{\partial x_i}$$

$$\Rightarrow \frac{\partial}{\partial x_i} = \sum_{\kappa\lambda} \frac{\partial x_i}{\partial \xi^\kappa} \overline{g}^{\kappa\lambda} \frac{\partial}{\partial \xi^\lambda},$$

given that

$$\sum_i \frac{\partial x_i}{\partial \xi^\sigma} \frac{\partial \xi^\tau}{\partial x_i} = \delta^\tau_\sigma.$$

Having obtained an expression for the partial derivative operator it is now simple to construct the matrix element for the Laplacian operator using two arbitrary wave functions ψ and ϕ as follows

$$\langle \psi | \nabla^2 | \phi \rangle = \sum_i \int d^5x \psi^* \frac{\partial^2 \phi}{\partial x_i^2}$$

$$\Rightarrow \langle \psi | \nabla^2 | \phi \rangle = -\sum_i \int d^5x \left(\frac{\partial \psi}{\partial x_i} \right)^* \frac{\partial \phi}{\partial x_i}.$$

Now it is possible to re-write this matrix element in terms of the curvilinear coordinates discussed above by

$$\begin{aligned}\langle\psi|\nabla^2|\phi\rangle &= -\sum_{i\kappa\lambda\kappa'\lambda'}\int d^5x\left(\frac{\partial\psi}{\partial\xi^\lambda}\right)^*\frac{\partial x_i}{\partial\xi^\kappa}\overline{g}^{\kappa\lambda}\frac{\partial x_i}{\partial\xi^{\kappa'}}\overline{g}^{\kappa'\lambda'}\frac{\partial\phi}{\partial\xi^{\lambda'}}\\ &= -\sum_{\kappa\lambda}\int d^5x\left(\frac{\partial\psi}{\partial\xi^\kappa}\right)^*\overline{g}^{\kappa\lambda}\frac{\partial\phi}{\partial\xi^\lambda}\\ &= -\sum_{\kappa\lambda}\int d^5\xi\left(\frac{\partial\psi}{\partial\xi^\kappa}\right)^* J\overline{g}^{\kappa\lambda}\frac{\partial\phi}{\partial\xi^\lambda}.\end{aligned}$$

Now we can undo the integration by parts in order to recover an expression for ∇ in the general curvilinear coordinates as follows

$$\begin{aligned}\langle\psi|\nabla^2|\phi\rangle &= \sum_{\kappa\lambda}\int d^5\xi\psi^*\frac{\partial}{\partial\xi^\kappa}J\overline{g}^{\kappa\lambda}\frac{\partial\phi}{\partial\xi^\lambda}\\ &= \sum_{\kappa\lambda}\int d^5x\psi^*\frac{1}{J}\frac{\partial}{\partial\xi^\kappa}J\overline{g}^{\kappa\lambda}\frac{\partial\phi}{\partial\xi^\lambda}\end{aligned}$$

$$\Rightarrow \nabla^2 = \sum_{\kappa\lambda}\frac{1}{J}\frac{\partial}{\partial\xi^\kappa}J\overline{g}^{\kappa\lambda}\frac{\partial}{\partial\xi^\lambda} \quad \text{(Laplace-Beltrami Operator).} \tag{C.1}$$

Appendix D

Derivation of the Metric Tensor and the Jacobian for the Bohr Hamiltonian

Given that the quadrupole moments q_m are given by

$$q_m = \beta \left[\cos(\gamma) \mathscr{D}^2_{0m}(\Omega) + \sqrt{\frac{1}{2}} \sin(\gamma) \left(\mathscr{D}^2_{2m}(\Omega) + \mathscr{D}^2_{-2m}(\Omega) \right) \right],$$

where the $\mathscr{D}^J_{KM}(\Omega)$ are rotation matrices corresponding to a set of Euler angles and by invoking the following identity

$$\sum_m (-1)^m \mathscr{D}^2_{\mu,m}(\Omega) \mathscr{D}^2_{\mu',-m}(\Omega) = \sqrt{5} \left(2\mu' 2\mu | 0,0 \right) = (-1)^\mu \delta_{\mu',-\mu},$$

we can obtain and simplify the following expressions for each of the 5 coordinates ($\beta, \gamma, \theta^1, \theta^2$ and θ^3). Starting for β we see

$$\begin{aligned}
\frac{\partial q_m}{\partial \beta} &= \cos(\gamma) \mathscr{D}^2_{0m}(\Omega) + \sqrt{\frac{1}{2}} \sin(\gamma) \left(\mathscr{D}^2_{2m}(\Omega) + \mathscr{D}^2_{-2m}(\Omega) \right) \\
\Rightarrow g_{\beta\beta} &= \cos^2(\gamma) \underbrace{\mathscr{D}^2_{0m}(\Omega) \mathscr{D}^2_{0m}(\Omega)}_{(-1)^0 \delta_{0,0}=1} + 2\sqrt{\frac{1}{2}} \cos(\gamma) \sin(\gamma) \left[\underbrace{\mathscr{D}^2_{0m}(\Omega) \mathscr{D}^2_{2m}(\Omega)}_{(-1)^0 \delta_{2,0}=0} + \underbrace{\mathscr{D}^2_{0m}(\Omega) \mathscr{D}^2_{-2m}(\Omega)}_{(-1)^0 \delta_{-2,0}=0} \right] \\
&\quad + \frac{1}{2} \sin^2(\gamma) \left[\underbrace{\mathscr{D}^2_{2m}(\Omega) \mathscr{D}^2_{2m}(\Omega)}_{(-1)^2 \delta_{2,-2}=0} + 2 \underbrace{\mathscr{D}^2_{2m}(\Omega) \mathscr{D}^2_{-2m}(\Omega)}_{(-1)^2 \delta_{2,2}=1} + \underbrace{\mathscr{D}^2_{-2m}(\Omega) \mathscr{D}^2_{-2m}(\Omega)}_{(-1)^2 \delta_{-2,2}=0} \right] \\
&= \cos^2(\gamma) + \sin^2(\gamma) \\
\Rightarrow g_{\beta\beta} &= 1.
\end{aligned}$$

For γ we obtain

$$
\begin{aligned}
\frac{\partial q_m}{\partial \gamma} &= \beta \left[-\sin(\gamma)\, \mathscr{D}^2_{0m}(\Omega) + \sqrt{\frac{1}{2}} \cos(\gamma) \left(\mathscr{D}^2_{2m}(\Omega) + \mathscr{D}^2_{-2m}(\Omega) \right) \right] \\
\Rightarrow g_{\gamma\gamma} &= \beta^2 \left[\sin^2(\gamma) \underbrace{\mathscr{D}^2_{0m}(\Omega)\, \mathscr{D}^2_{0m}(\Omega)}_{(-1)^0 \delta_{0,0}=1} - 2\sqrt{\frac{1}{2}} \sin(\gamma)\cos(\gamma) \left[\underbrace{\mathscr{D}^2_{0m}(\Omega)\, \mathscr{D}^2_{2m}(\Omega)}_{(-1)^0 \delta_{2,0}=0} + \underbrace{\mathscr{D}^2_{0m}(\Omega)\, \mathscr{D}^2_{-2m}(\Omega)}_{(-1)^0 \delta_{-2,0}=0} \right] \right. \\
&\quad \left. + \frac{1}{2}\cos^2(\gamma) \left[\underbrace{\mathscr{D}^2_{2m}(\Omega)\, \mathscr{D}^2_{2m}(\Omega)}_{(-1)^2 \delta_{2,-2}=0} + 2\, \underbrace{\mathscr{D}^2_{2m}(\Omega)\, \mathscr{D}^2_{-2m}(\Omega)}_{(-1)^2 \delta_{2,2}=1} + \underbrace{\mathscr{D}^2_{-2m}(\Omega)\, \mathscr{D}^2_{-2m}(\Omega)}_{(-1)^2 \delta_{-2,2}=0} \right] \right] \\
&= \beta^2 \left[\cos^2(\gamma) + \sin^2(\gamma) \right] \\
\Rightarrow g_{\gamma\gamma} &= \beta^2 .
\end{aligned}
$$

For θ^1, θ^2 and θ^3 they all follow a similar simplification as follows

$$
\begin{aligned}
\frac{\partial q_m}{\partial \theta^1} &= -i\beta \left(\sqrt{\frac{3}{2}} \cos(\gamma) + \sqrt{\frac{1}{2}} \sin(\gamma) \right) \left[\mathscr{D}^2_{1m}(\Omega) + \mathscr{D}^2_{-1,m}(\Omega) \right] \\
\Rightarrow g_{11} &= -\beta^2 \left(\sqrt{\frac{3}{2}} \cos(\gamma) + \sqrt{\frac{1}{2}} \sin(\gamma) \right)^2 \left[\underbrace{\mathscr{D}^2_{1m}(\Omega)\, \mathscr{D}^2_{1m}(\Omega)}_{(-1)^1 \delta_{1,-1}=0} + 2\, \underbrace{\mathscr{D}^2_{1m}(\Omega)\, \mathscr{D}^2_{-1,m}(\Omega)}_{(-1)^1 \delta_{1,1}=-1} \right. \\
&\quad \left. + \underbrace{\mathscr{D}^2_{-1,m}(\Omega)\, \mathscr{D}^2_{-1,m}(\Omega)}_{(-1)^1 \delta_{-1,1}=0} \right] \\
\Rightarrow g_{11} &= 2\beta^2 \left(\sqrt{\frac{3}{2}} \cos(\gamma) + \sqrt{\frac{1}{2}} \sin(\gamma) \right)^2 \\
&= \beta^2 \left[3\cos^2(\gamma) + 2\sqrt{3} \sin(\gamma)\cos(\gamma) + \sin^2(\gamma) \right] \\
&= 4\beta^2 \left[\frac{3}{4}\cos^2(\gamma) + \frac{2}{4}\sqrt{3}\sin(\gamma)\cos(\gamma) + \frac{1}{4}\sin^2(\gamma) \right] \\
&= 4\beta^2 \left(-\frac{1}{2}\sin(\gamma) - \frac{\sqrt{3}}{2}\cos(\gamma) \right) \left(-\frac{1}{2}\sin(\gamma) - \frac{\sqrt{3}}{2}\cos(\gamma) \right) \\
&= 4\beta^2 \left(\sin(\gamma)\cos\left(\frac{2\pi}{3}\right) - \cos(\gamma)\sin\left(\frac{2\pi}{3}\right) \right) \left(\sin(\gamma)\cos\left(\frac{2\pi}{3}\right) - \cos(\gamma)\sin\left(\frac{2\pi}{3}\right) \right) \\
&= 4\beta^2 \sin\left(\gamma - \frac{2\pi}{3}\right) \sin\left(\gamma - \frac{2\pi}{3}\right) \\
\Rightarrow g_{11} &= 4\beta^2 \sin^2\left(\gamma - \frac{2\pi}{3}\right) .
\end{aligned}
$$

$$\frac{\partial q_m}{\partial \theta^2} = \beta\left(\sqrt{\frac{3}{2}}\cos(\gamma) - \sqrt{\frac{1}{2}}\sin(\gamma)\right)\left[\mathscr{D}^2_{1m}(\Omega) - \mathscr{D}^2_{-1,m}(\Omega)\right]$$

$$\Rightarrow g_{22} = \beta^2\left(\sqrt{\frac{3}{2}}\cos(\gamma) - \sqrt{\frac{1}{2}}\sin(\gamma)\right)^2\left[\underbrace{\mathscr{D}^2_{1m}(\Omega)\,\mathscr{D}^2_{1m}(\Omega)}_{(-1)^1\delta_{1,-1}=0} - 2\underbrace{\mathscr{D}^2_{1m}(\Omega)\,\mathscr{D}^2_{-1,m}(\Omega)}_{(-1)^1\delta_{1,1}=-1} + \underbrace{\mathscr{D}^2_{-1,m}(\Omega)\,\mathscr{D}^2_{-1,m}(\Omega)}_{(-1)^1\delta_{-1,1}=0}\right]$$

$$\begin{aligned}
\Rightarrow g_{22} &= 2\beta^2\left(\sqrt{\frac{3}{2}}\cos(\gamma) - \sqrt{\frac{1}{2}}\sin(\gamma)\right)^2 \\
&= \beta^2\left[3\cos^2(\gamma) - 2\sqrt{3}\sin(\gamma)\cos(\gamma) + \sin^2(\gamma)\right] \\
&= 4\beta^2\left[\frac{3}{4}\cos^2(\gamma) - \frac{2}{4}\sqrt{3}\sin(\gamma)\cos(\gamma) + \frac{1}{4}\sin^2(\gamma)\right] \\
&= 4\beta^2\left(-\frac{1}{2}\sin(\gamma) + \frac{\sqrt{3}}{2}\cos(\gamma)\right)\left(-\frac{1}{2}\sin(\gamma) + \frac{\sqrt{3}}{2}\cos(\gamma)\right) \\
&= 4\beta^2\left(\sin(\gamma)\cos\left(\frac{4\pi}{3}\right) - \cos(\gamma)\sin\left(\frac{4\pi}{3}\right)\right)\left(\sin(\gamma)\cos\left(\frac{4\pi}{3}\right) - \cos(\gamma)\sin\left(\frac{4\pi}{3}\right)\right) \\
&= 4\beta^2\sin\left(\gamma - \frac{4\pi}{3}\right)\sin\left(\gamma - \frac{4\pi}{3}\right) \\
\Rightarrow g_{22} &= 4\beta^2\sin^2\left(\gamma - \frac{4\pi}{3}\right).
\end{aligned}$$

$$\frac{\partial q_m}{\partial \theta^3} = i\beta\sqrt{2}\sin(\gamma)\left[\mathscr{D}^2_{2m}(\Omega) - \mathscr{D}^2_{-2,m}(\Omega)\right]$$

$$\Rightarrow g_{33} = -2\beta^2\sin^2(\gamma)\left[\underbrace{\mathscr{D}^2_{2m}(\Omega)\,\mathscr{D}^2_{2m}(\Omega)}_{(-1)^2\delta_{2,-2}=0} - 2\underbrace{\mathscr{D}^2_{2m}(\Omega)\,\mathscr{D}^2_{-2,m}(\Omega)}_{(-1)^2\delta_{2,2}=1} + \underbrace{\mathscr{D}^2_{-2,m}(\Omega)\,\mathscr{D}^2_{-2,m}(\Omega)}_{(-1)^2\delta_{-2,2}=0}\right]$$

$$\Rightarrow g_{33} = 4\beta^2\sin^2(\gamma).$$

Hence, we have obtained the metric tensor matrix elements and can construct the metric tensor as follows

$$g = \begin{pmatrix}
1 & 0 & 0 & 0 & 0 \\
0 & \beta^2 & 0 & 0 & 0 \\
0 & 0 & 4\beta^2\sin^2(\gamma - 2\pi/3) & 0 & 0 \\
0 & 0 & 0 & 4\beta^2\sin^2(\gamma - 4\pi/3) & 0 \\
0 & 0 & 0 & 0 & 4\beta^2\sin^2(\gamma)
\end{pmatrix}$$

and since the matrix is diagonal the Jacobian J is given by the product of the diagonal terms yielding

$$J^2 = 64\beta^8\sin^2(\gamma)\sin^2(\gamma - 2\pi/3)\sin^2(\gamma - 4\pi/3),$$

which we can simplify using the following trigonometric identities

$$\begin{aligned}
\sin(A \pm B) &= \sin(A)\cos(B) \pm \cos(A)\sin(B) \\
\Rightarrow \sin(3A) &= 3\cos^2(A)\sin(A) - \sin^3(A).
\end{aligned}$$

Hence,

$$\begin{aligned}\sin^2(\gamma - 2\pi/3) &= (\sin(\gamma)\cos(2\pi/3) - \cos(\gamma)\sin(2\pi/3))^2 \\ &= \left(-\frac{1}{2}\sin(\gamma) - \frac{\sqrt{3}}{2}\cos(\gamma)\right)^2 \\ &= \frac{1}{4}\sin^2(\gamma) + \frac{\sqrt{3}}{2}\sin(\gamma)\cos(\gamma) + \frac{3}{4}\cos^2(\gamma)\end{aligned}$$

and

$$\begin{aligned}\sin^2(\gamma - 4\pi/3) &= (\sin(\gamma)\cos(4\pi/3) - \cos(\gamma)\sin(4\pi/3))^2 \\ &= \left(-\frac{1}{2}\sin(\gamma) + \frac{\sqrt{3}}{2}\cos(\gamma)\right)^2 \\ &= \frac{1}{4}\sin^2(\gamma) - \frac{\sqrt{3}}{2}\sin(\gamma)\cos(\gamma) + \frac{3}{4}\cos^2(\gamma)\,.\end{aligned}$$

Therefore,

$$\begin{aligned}\sin^2(\gamma - 2\pi/3)\sin^2(\gamma - 4\pi/3) &= \left(\frac{1}{4}\sin^2(\gamma) + \frac{\sqrt{3}}{2}\sin(\gamma)\cos(\gamma) + \frac{3}{4}\cos^2(\gamma)\right) \\ &\quad \left(\frac{1}{4}\sin^2(\gamma) - \frac{\sqrt{3}}{2}\sin(\gamma)\cos(\gamma) + \frac{3}{4}\cos^2(\gamma)\right) \\ &= \frac{1}{16}\sin^4(\gamma) - \frac{\sqrt{3}}{8}\sin^3(\gamma)\cos(\gamma) \\ &\quad + \frac{3}{16}\sin^2(\gamma)\cos^2(\gamma) + \frac{\sqrt{3}}{8}\sin^3(\gamma)\cos(\gamma) \\ &\quad - \frac{3}{4}\sin^2(\gamma)\cos^2(\gamma) + \frac{3\sqrt{3}}{8}\sin(\gamma)\cos^3(\gamma) + \frac{3}{16}\sin^2(\gamma)\cos^2(\gamma) \\ &\quad - \frac{3\sqrt{3}}{8}\sin(\gamma)\cos^3(\gamma) + \frac{9}{16}\cos^4(\gamma) \\ &= \frac{1}{16}\sin^4(\gamma) + \left(\frac{3}{16} + \frac{3}{16} - \frac{12}{16}\right)\sin^2(\gamma)\cos^2(\gamma) + \frac{9}{16}\cos^4(\gamma) \\ &= \frac{1}{16}\sin^4(\gamma) - \frac{6}{16}\sin^2(\gamma)\cos^2(\gamma) + \frac{9}{16}\cos^4(\gamma)\,,\end{aligned}$$

which implies

$$\begin{aligned}\sin^2(\gamma)\sin^2(\gamma - 2\pi/3)\sin^2(\gamma - 4\pi/3) &= \frac{1}{16}\left(\sin^6(\gamma) - 6\sin^4(\gamma)\cos^2(\gamma) + 9\cos^4(\gamma)\sin^2(\gamma)\right) \\ &= \frac{1}{16}\left(-\sin^3(\gamma) + 3\cos^2(\gamma)\sin(\gamma)\right)\left(-\sin^3(\gamma) + 3\cos^2(\gamma)\sin(\gamma)\right) \\ &= \frac{1}{16}\sin^2(3\gamma)\,.\end{aligned}$$

Hence, the Jacobian J can be simplified to

$$\begin{aligned}J^2 &= 4\beta^8\sin^2(3\gamma) \\ \Rightarrow J &= \pm 2\beta^4\sin(3\gamma)\,. \qquad \text{(D.1)}\end{aligned}$$

Noting that for a physical coordinate system we will use the positive root i.e. $J = 2\beta^4\sin(3\gamma)$.

List of Acronyms

Acronym	
QCD	Quantum Chromodynamics
LQCD	Lattice Quantum Chromodynamics
HK	Hohenberg-Kohn
HF	Hartree-Fock
HFB	Hartree-Fock-Bogoliubov
TDHFB	Time Dependent Hartree-Fock-Bogoliubov
ATDHFB	Adiabatic Time Dependent Hartree-Fock-Bogoliubov
DFT	Density Functional Theory
NDFT	Nuclear Density Functional Theory
BH	Bohr Hamiltonian
GBH	Generalised Bohr Hamiltonian
UNEDF	Universal Nuclear Energy Density Functional
PES	Potential Energy Surface
NNDC	National Nuclear Data Center

Bibliography

[1] Bertsch G, Dean D and Nazarewicz W 2007 *SciDAC Review* **6** 42

[2] National Nuclear Data Center, Brookhaven National Laboratory URL `https://www.nndc.bnl.gov/`

[3] Delaroche J P, Girod M, Libert J, Goutte H, Hilaire S, Peru S, Pillet N and Bertsch G 2009 *Physical Review C* **81**

[4] Mottelson B R 1975 Nobel Lecture: Elementary Modes of Excitation in the Nucleus URL `https://www.nobelprize.org/prizes/physics/1975/mottelson/lecture/`

[5] Bettini A 2014 *Introduction to Elementary Particle Physics* (Cambridge University Press)

[6] Rowe D J and Wood J L 2010 *Fundamentals of nuclear models foundational models* (World Scientific)

[7] Lin H W and Meyer H B 2015 *Lattice QCD for Nuclear Physics* vol 889 (Springer)

[8] Hjorth-Jensen M, Lombardo M and Kolck U 2017 *An advanced course in computational nuclear physics: bridging the scales from quarks to neutron stars* Lecture notes in physics (Springer)

[9] Hohenberg P and Kohn W 1964 *Phys. Rev.* **136**(3B) B864–B871 URL `https://link.aps.org/doi/10.1103/PhysRev.136.B864`

[10] Fiolhais C, Nogueira F and Marques M 2003 *A Primer in Density Functional Theory* vol 620 (Springer)

[11] Engel E and Dreizler R 2010 *Density Functional Theory: An Advanced Course* vol 1 ISBN 978-3-642-14089-1

[12] Martin R 2004 *Electronic Structure: Basic Theory and Practical Methods* vol 1 ISBN 9780521534406

[13] Meng J 2016 *Relativistic Density Functional for Nuclear Structure* (WORLD SCIENTIFIC) (*Preprint* `https://www.worldscientific.com/doi/pdf/10.1142/9872`) URL `https://www.worldscientific.com/doi/abs/10.1142/9872`

[14] Ring P and Schuck P 2004 *The nuclear many-body problem* (Springer)

[15] Bohr A, Mottelson B R and Pines D 1958 *Phys. Rev.* **110**(4) 936–938 URL `https://link.aps.org/doi/10.1103/PhysRev.110.936`

[16] Skyrme T H R 1959 *Nuclear Physics* **9** 615 – 634 ISSN 0029-5582 URL `http://www.sciencedirect.com/science/article/pii/0029558258903456`

[17] Decharge J and Gogny D 1980 *Phys. Rev. C* **21** 1568–1593

[18] Vautherin D and Brink D M 1972 *Phys. Rev. C* **5**(3) 626–647 URL https://link.aps.org/doi/10.1103/PhysRevC.5.626

[19] Sadoudi J, Duguet T, Meyer J and Bender M 2013 *Phys. Rev. C* **88** 064326 (*Preprint* 1310.0854)

[20] Schunck N 2019 *Energy Density Functional Methods for Atomic Nuclei* 2053-2563 (IOP Publishing) ISBN 978-0-7503-1422-0 URL http://dx.doi.org/10.1088/2053-2563/aae0ed

[21] Kortelainen M, Lesinski T, Moré J, Nazarewicz W, Sarich J, Schunck N, Stoitsov M V and Wild S 2010 *Phys. Rev. C* **82**(2) 024313 URL https://link.aps.org/doi/10.1103/PhysRevC.82.024313

[22] Kortelainen M, McDonnell J, Nazarewicz W, Reinhard P G, Sarich J, Schunck N, Stoitsov M V and Wild S M 2012 *Phys. Rev. C* **85**(2) 024304 URL https://link.aps.org/doi/10.1103/PhysRevC.85.024304

[23] Shi Y, Dobaczewski J and Greenlees P T 2014 *Phys. Rev. C* **89**(3) 034309 URL https://link.aps.org/doi/10.1103/PhysRevC.89.034309

[24] Bender M, Rutz K, Reinhard P G, Maruhn J A and Greiner W 1999 *Phys. Rev. C* **60**(3) 034304 URL https://link.aps.org/doi/10.1103/PhysRevC.60.034304

[25] Bulgac A and Yu Y 2002 *Phys. Rev. Lett.* **88**(4) 042504 URL https://link.aps.org/doi/10.1103/PhysRevLett.88.042504

[26] Berger J, Girod M and Gogny D 1991 *Computer Physics Communications* **63** 365 – 374 ISSN 0010-4655 URL http://www.sciencedirect.com/science/article/pii/001046559190263K

[27] Péru S and Martini M 2014 *The European Physical Journal A* **50** 88 ISSN 1434-601X URL https://doi.org/10.1140/epja/i2014-14088-7

[28] Ragnarsson I and Nilsson S 2005 *Shapes and Shells in Nuclear Structure* (Cambridge University Press)

[29] Sheikh J, Dobaczewski J, Ring P, Robledo L and Yannouleas C 2019 (*Preprint* 1901.06992)

[30] Baranger M and Véneroni M 1978 *Annals of Physics* **114** 123–200 ISSN 0003-4916 URL https://www.sciencedirect.com/science/article/pii/0003491678902658

[31] Prochniak L Mass parameters unpublished summary notes of mass parameters as defined in the adiabatic time-dependent Hartree-Fock-Bogoliubov theory

[32] Prochniak L and Rohozinski S G 2009 *J. Phys.* **G36** 123101 (*Preprint* 0911.0366)

[33] Inglis D R 1955 *Phys. Rev.* **97**(3) 701–706 URL https://link.aps.org/doi/10.1103/PhysRev.97.701

[34] Bohr A and Mottelson B R 2008 *Nuclear structure volume 1: single-particle motion* (World Scientific)

[35] Bohr A and Mottelson B R 2008 *Nuclear structure volume 2: nuclear deformation* (World Scientific)

[36] Matsuyanagi K, Matsuo M, Nakatsukasa T, Yoshida K, Hinohara N and Sato K 2016 *Phys. Scripta* **91** 063014 (*Preprint* 1606.08547)

[37] Rohoziński S, Próchniak L, Starosta K and Droste C 2011 *The European Physical Journal A* **47** 1–15

[38] Guo J Y 2015 *Phys. Rev. C* **92** 014307 (*Preprint* 1707.00247)

[39] Lenis D and Bonatsos D 2006 *Physics Letters B* **633** 474–478

[40] Xiang J, Li Z P, Nikšić T, Vretenar D and Long W H 2020 *Phys. Rev. C* **101**(6) 064301 URL https://link.aps.org/doi/10.1103/PhysRevC.101.064301

[41] Robledo L M 2010 *Journal of Physics G: Nuclear and Particle Physics* **37** 064020 URL https://doi.org/10.1088/0954-3899/37/6/064020

[42] Schunck N, Dobaczewski J, McDonnell J, Satuła W, Sheikh J, Staszczak A, Stoitsov M and Toivanen P 2012 *Computer Physics Communications* **183** 166 – 192 ISSN 0010-4655 URL http://www.sciencedirect.com/science/article/pii/S0010465511002852

[43] Prochniak L 2015 *Phys. Scripta* **90** 114005 (*Preprint* 1502.02707)

[44] Li Z P, Nikšić T, Ring P, Vretenar D, Yao J M and Meng J 2012 *Phys. Rev. C* **86**(3) 034334 URL https://link.aps.org/doi/10.1103/PhysRevC.86.034334

[45] Thouless D and Valatin J 1962 *Nuclear Physics* **31** 211–230 ISSN 0029-5582 URL https://www.sciencedirect.com/science/article/pii/0029558262907411

[46] Dobaczewski J *et al.* 2009 (*Preprint* 0909.3626)

[47] Washiyama K, Hinohara N and Nakatsukasa T 2021 *Phys. Rev. C* **103**(1) 014306 URL https://link.aps.org/doi/10.1103/PhysRevC.103.014306

[48] Prochniak L Diagonalization of the general bohr hamiltonian. program nmuri18. unpublished summary notes of the definitions used within the Bohr Hamiltonain code

[49] Stephens F S 1974 *Lawrence Berkeley National Laboratory* URL https://escholarship.org/uc/item/93z6p5hq

[50] Stephens F S 1975 *Rev. Mod. Phys.* **47**(1) 43–65 URL https://link.aps.org/doi/10.1103/RevModPhys.47.43

[51] Kumar V, Kumar S, Kumar S, Hasan Z, Koranga B S, Negi D and Lee A 2011 *International Journal of Modern Physics E-nuclear Physics - IJMPE* **20** 1455–1463

[52] Muir D, Próchniak L, Pastore A and Dobaczewski J 2020 Structure of Krypton Isotopes using the Generalised Bohr Hamiltonian Method *27th International Nuclear Physics Conference* (*Preprint* 2004.10835)

[53] Llewellyn R D O, Bentley M A, Wadsworth R, Iwasaki H, Dobaczewski J, de Angelis G, Ash J, Bazin D, Bender P C, Cederwall B, Crider B P, Doncel M, Elder R, Elman B, Gade A, Grinder M, Haylett T, Jenkins D G, Lee I Y, Longfellow B, Lunderberg E, Mijatović T, Milne S A, Muir D, Pastore A, Rhodes D and Weisshaar D 2020 *Phys. Rev. Lett.* **124**(15) 152501 URL https://link.aps.org/doi/10.1103/PhysRevLett.124.152501

[54] Wimmer K, Korten W, Doornenbal P, Arici T, Aguilera P, Algora A, Ando T, Baba H, Blank B, Boso A, Chen S, Corsi A, Davies P, de Angelis G, de France G, Delaroche J P, Doherty D T, Gerl J, Gernhäuser R, Girod M, Jenkins D, Koyama S, Motobayashi T, Nagamine S, Niikura M, Obertelli A, Libert J, Lubos D, Rodríguez T R, Rubio B, Sahin E, Saito T Y, Sakurai H, Sinclair L, Steppenbeck D, Taniuchi R, Wadsworth R and Zielinska M 2021 *Phys. Rev. Lett.* **126**(7) 072501 URL https://link.aps.org/doi/10.1103/PhysRevLett.126.072501

[55] Nikšić T, Li Z P, Vretenar D, Próchniak L, Meng J and Ring P 2009 *Phys. Rev. C* **79**(3) 034303 URL https://link.aps.org/doi/10.1103/PhysRevC.79.034303

[56] FRIB Mass Explorer URL http://massexplorer.frib.msu.edu/

[57] Larsson S, Leander G and Ragnarsson I 1978 *Nuclear Physics A* **307** 189–223 ISSN 0375-9474 URL https://www.sciencedirect.com/science/article/pii/0375947478906139

[58] Sivia D S and Skilling J 2006 *Data Analysis A Bayesian Tutorial* (Oxford Science Publications)

[59] Haverinen T and Kortelainen M 2017 *Journal of Physics G: Nuclear and Particle Physics* **44** 044008 URL https://doi.org/10.1088/1361-6471/aa5e07